WATER REACTOR SAFETY RESEARCH DIVISION

QUARTERLY PROGRESS REPORT
JULY 1 - SEPTEMBER 30, 1979

HERBERT J.C. KOUTS, Department Chairman
WALTER Y. KATO, Associate Chairman for Reactor Safety

Principal Investigators:

D.J. Diamond	W.G. Shier, Jr.
O.C. Jones, Jr.	D. van Rooyen
M.M. Levine	

Compiled by Anthony J. Romano
Manuscript Completed: December 1979

DEPARTMENT OF NUCLEAR ENERGY
BROOKHAVEN NATIONAL LABORATORY, ASSOCIATED UNIVERSITIES, INC.
UPTON, NEW YORK 11973

8005270012

FOREWORD

The Water Reactor Safety Research Programs Quarterly Report describes current activities and technical progress in the programs at Brookhaven National Laboratory sponsored by the USNRC Division of Reactor Safety Research. The projects reported each quarter are the following: LWR Thermal Hydraulic Development, Advanced Code Evaluation, TRAC Code Assessment, and Stress Corrosion Cracking of PWR Steam Generator Tubing.

The previous reports, BNL-NUREG-50624, BNL-NUREG-50661, BNL-NUREG-50683, BNL-NUREG-50747, BNL-NUREG-50785, BNL-NUREG-50820, BNL-NUREG-50883, BNL-NUREG-50931, BNL-NUREG-50978, BNL-NUREG-51015 and BNL-NUREG-51081 have covered the periods October 1, 1976 through June 30, 1979.

WATER REACTOR SAFETY RESEARCH

TABLE OF CONTENTS

I. LIGHT WATER REACTOR SAFETY

SUMMARY

The understanding of the nonequilibrium vapor generation process in liquids under sudden depressurization in static or flowing systems and its modeling require a basic understanding and prediction capability of the inception conditions and a suitable and realistic growth law.

Alamgir and Lienhard (1979) developed a method for correlating the inception point of static systems. They related the pressure undershoot at flashing onset below the saturation pressure to the reduced temperature and the static depressurization rate, and they correlated various blowdown experiments covering depressurization rates of $(- dp/dt) \geq 10^8$ Pa/s with an estimated deviation of 10.4 percent.

For flowing systems in pipes, the experimental inception points observed by Reocreux were related to the Alamgir and Lienhard's static onset correlation provided that one makes corrections for the effects of the turbulent pressure fluctuations.

In flowing systems in nozzles with subcooled inlet conditions, the flashing inception was observed to occur very close to the throat. Once again, this onset point was related to Alamgir and Lienhard's static onset predictions and a physical basis to explain this observation thereby resulted. In order to test this reasoning, a resulting corrollary hypothesis could be considered suggesting that in general there would be negligible vaporization in the converging section of flashing experiments performed with subcooled inlet conditions. Flow rates should thus be correlated with single phase discharge coefficients. Indeed this was found to be so for test results available in the literature for water and liquid nitrogen in converging-diverging nozzle over a very wide range of subcooling. Therefore, between Alamgir and Lienhard's static flashing onset correlation and our observations in flowing systems (both in pipes and in nozzles) one can unify both aspects of the flashing inception problem. This allows us now to precisely describe the initial superheat at the onset of flashing, a quantity upon which downstream noneq .librium vapor generation is heavily dependent. Once the inception point is determined, two methods are proposed to solve the growth integral:

a. The first approach involves the use and integration of the bubble growth model developed by Saha and Wu, in conjunction with the onset information obtained from Alamgir and Lienhard's correlation. The only free parameter in this approach will be the packing density of bubbles at inception.

b. The second approach involves the solution of the jump conditions across a nonequilibrium vapor generating zone to obtain values for limiting cases. The application of this latter method to several experimental conditions (Reocreux, Brown and BNL), however, did not produce a possible solution. While the basic assumptions underlying this method are being examined to determine the applicability of this procedure, it is stressed that mechanical nonequilibrium has been eliminated as an important factor.

In the flashing experiments, new measurements with the five beam gamma densitometer were used to calculate the area averaged void profiles. Data were recorded under flashing conditions for 100 and 125 C inlet temperatures and several flow rates.

The results of a typical experiment (Run 130) are presented in detail, including the transverse distributions of the chordal averaged void profiles at various axial locations. The calculation of the area-averaged void fraction from these data is also summarized and presented. The experimental results of pressure distributions, void profiles, and vapor generation rates are compared to TRAC-P1A predictions. Run 130 was a repetition of Run 76 conducted in the last series of runs under similar experimental conditions. The repeatability of the experimental results are excellent. For the specific experiment presented (Run 130), the diametrical averaged void fractions were found not to be generally representative of the area averaged void fractions at the same axial location. The TRAC-P1A predictions seem to agree reasonably well with the experimental results of Run 130. This is attributed to the fact that inception in this experiment was very close to the saturation conditions. On the other hand, for experiments where the inception occurs under highly nonequilibrium conditions, significant differences between the TRAC-P1A predictions and experimental data will be expected.

Considerable progress has been made in developing and implementing new component models for RAMONA-III. A model for the recirculation loop drive pump was developed and combined with the jet pump model previously done. These models are being implemented within the code. They have successfully executed as stand-along packages. The steamline model has successfully executed both as a stand-alone code and within RAMONA-III. A rudimentary control and protection system has been implemented.

A new fuel rod heat conduction model was developed and implemented in the code. New updates to the code were received from Scandpower and generated at BNL in order to correct and improve the code. A graphics capability is in the process of being developed. A Peach Bottom-2 plant model was developed at BNL and a similar input deck was received from Scandpower. Calculations are being run with these data in order to understand what improvements might still be needed.

The RETRAN code has successfully run all six test problems supplied with the code. In addition, a plant model for Three Mile Island has been obtained and run on the BNL CDC-6600.

The once-through steam generator model with a momentum equation to calculate the recirculation flow through the aspirator region has been incorporated in the IRT code. In addition, a model for steam generator tube rupture and steamline break analyses has been implemented on IRT.

Work on the independent assessment of TRAC-P1A has continued during the reporting quarter. The sensitivity of the code to the size of the inlet BREAK cell and nodalization has been studied for the Moby-Dick nitrogen-water tests. An idealized thought experiment has been conducted in a shock-tube filled with air to check only the numerics of the code. The Marviken critical flow Tests 22 and 24 have been simulated with TRAC-P1A, and the possible reasons for the discrepancies are discussed. The code was unable to reach a steady-state for RPI phase separation Test #3. For FRIGG Loop tests, the code was first applied to a simpler test vessel without rods and a steady-state was reached.

1. Light Water Reactor Thermal/Hydraulic Development Program (N. Abuaf and
O. C. Jones, Jr.)

1.1 Modeling of the Nonequilibrium Flashing Process (N. Abuaf and B.J.C. Wu)

1.1.1 Flashing Inception in Converging-Diverging Nozzles With Subcooled Water
Inlet Conditions

One observation from the BNL flashing experiments that was reported
previously (Zimmer 1979) pointed out to the fact that in a wide range of
experiments performed with subcooled water inlet conditions, the flashing
inception occurred very close to the nozzle throat. This fact implies that
if the above-mentioned observation is generally true, then all the experimen-
tal data existing in the literature and concerning the flow of liquids in
converging-diverging nozzles may be correlated by a single phase discharge
coefficient. The discharge coefficient for an incompressible liquid can be
related to the mass flux through the throat (G_T), the density (ρ), and

pressure difference between the inlet and throat $(p_o - p_T)$ where the inlet

area is assumed to be large such that the inlet velocity is negligibly small:

$$c_D = \sqrt{\frac{G_T^2}{2\rho(p_o - p_T)}} \tag{1.1}$$

The experimental data existing in the literature for converging-diverging
nozzle flows with various subcooled inlet conditions and with flashing in the
nozzle were considered. The experimental data examined in all these experi-
ments included the mass flux, the pressures at the inlet and throat, and
inlet conditions for the determination of the density. The data analyzed
included those of Brown (1961), Schrock (1977), Sozzi (1975), and Zimmer
(1979) for water and Simoneau (1979) for liquid nitrogen. Figure (1.1) shows
the pressure distributions in the converging-diverging nozzle as recorded by
Brown (1961) for his runs No. 36 and 51. Run 36 had an inlet pressure of

8.5×10^3 kPa, an inlet temperature of 270 ^{o}C, corresponding to a highly
subcooled inlet condition, since the saturation pressure at the inlet tem-

perature was 5.5×10^3 kPa [50 ^{o}C subcooling (Schrock, 1977)]. Run 51, on

the other hand, had an inlet pressure of 7.14×10^3 kPa, an inlet temperature
of 286 ^{o}C, conditions very close to the saturation line, since the saturation

pressure at the inlet temperature was 7.03×10^3 kPa. Schrock (1977) assumed
this run to have subcooled inlet conditions (18.3 ^{o}C subcooling), but the
investigator's own estimated pressure measurement accuracy (Schrock, 1977) of
5 percent would imply that this run could have had a very low inlet void
fraction. In the following calculations, we shall follow the original
investigator's assertion that this experiment had a subcooled inlet condi-
tion. These pressure distributions presented in Fig. (1.1) show the large
range of subcooling in Brown's experiments from 18.3 ^{o}C to 50 ^{o}C. The
discharge coefficients calculated for Brown's data (1961), Sozzi's data
(1975), and BNL data (Zimmer, 1979), as well as two sets of the liquid
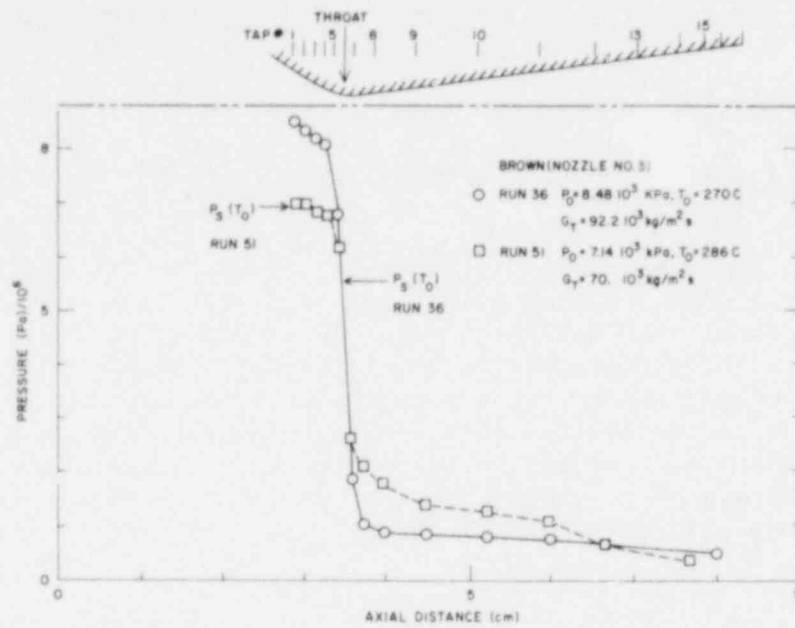nitrogen data obtained by Simoneau (1979) for his conical nozzle with inlet

Figure (1.1) - Pressure Distributions for Two Experiments (Run 36, 51) Under 18.3 and 50 °C Subcooled Inlet Conditions (Brown 1961). (BNL Neg. No. 11-669-79).
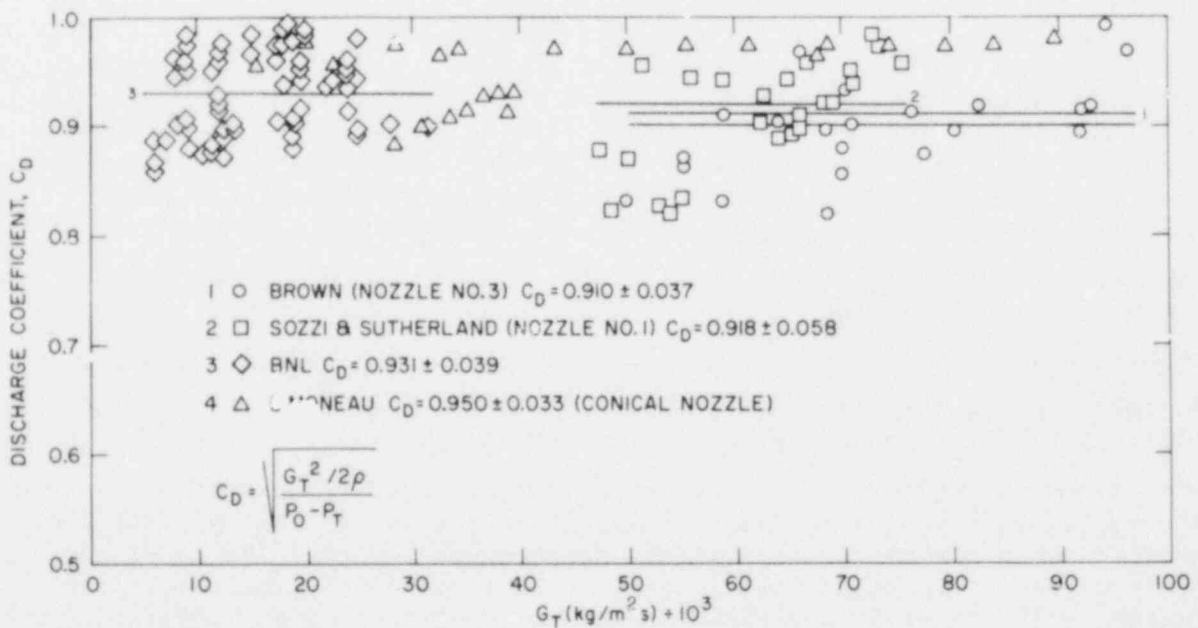

Figure (1.2) - Variation of the Discharge Coefficient With the Throat Mass Flux for Data in a Converging-Diverging Nozzle With Subcooled Liquid Inlet Conditions. (BNL Neg. No. 11-664-79).

temperatures of 95 ^{O}K and 110 ^{O}K are plotted in Fig. (1.2), as a function of the throat mass flux. The discharge coefficients calculated for each nozzle are scattered around a value of $\pm$ 0.92 $\pm$ 0.04, a value quite close to the expected single phase discharge coefficient for converging-diverging nozzles. The slightly larger standard deviation in Sozzi and Sutherland's data (Nozzle No. 1) could be due to the possibility that inlet voids existed for some of the experiments reported here. Their stagnation qualities were deduced from fluid density in the vessel ρ obtained through hydrostatics, and the stagnation pressures, p_o.

$$x_o \triangleq \frac{\frac{1}{\rho} - V_f(p_o)}{V_{fg}(p_o)} \tag{1.2}$$

All the data presented by Sozzi (1975) with Nozzle No. 1, with a negative inlet quality from Eq. (1.2), implying subcooled inlet conditions were included in the results presented in Fig. (1.2). This definition (Sozzi 1975) of the subcooling strongly depends on the method the density in the vessel was measured, since some stratification in the vessel was reported. Thus some of the subcooled runs which had a very small negative quality $\sim -2 \times 10^{-4}$, could have had a very low inlet void fraction. In Fig. (1.2), again the original investigator's claim was followed and all the negative inlet quality data were assumed to be subcooled. The small variation of C_D over the wide range of subcooled venturi-nozzle data presented in Fig. (1.2), implies that the flow up to the nozzle throat is single phase liquid. In addition, one can conclude that even if flashing occurred close but upstream of the throat pressure tap, the density change caused by the flashing inception did not have a significant effect on the pressure measured at the throat. The logical correlation of the data should be C_D vs Reynolds number and not throat mass flux as presented in the figure. This graph is in preparation and should depict a clearer trend once plotted. Additional experiments performed by Sozzi and Sutherland (1975) with their nozzle (No. 3), which is a straight-edge orifice, with subcooled inlet conditions, provided a discharge coefficient (not shown) of 0.67 $\pm$ 0.0?, which is also very close to the expected single phase value for an orifice.

We also tried to substantiate the fact mentioned above that under subcooled inlet conditions, flashing inception seems to occur very close to the throat, from a different point of view. Alamgir (1979) developed a method for correlating the pressure undershoot at flashing onset of a system below the saturation pressure during a rapid static depressurization and flashing of water. Data from various work were used in the correlation and the probable error in the predicted undershoot was estimated to be $\pm$ 10.4 percent for large depressurization rates. The pressure undershoot below the saturation pressure, p_s, was related to the system reduced temperature (T_R) and the depressurization rate (Σ') by the following expression

$$p_s - p_n = 0.2483 \frac{\sigma^{3/2}}{\sqrt{kT_c}} \cdot \frac{T_R^{13.73} \left[1 + 14.15 \; \Sigma'^{0.8}\right]^{0.5}}{1 - \frac{V_f}{V_g}} \tag{1.3}$$

for $\Sigma' > 4 \times 10^{-3}$ Matm/s and where σ is the surface tension, k, Boltzmann's constant, T_c, the critical temperature, and V_f and V_g are the specific volumes of saturated liquid and saturated vapor at the initial temperature in the depressurization process. The pressure undershoot at flashing onset as a function of the depressurization rate predicted by Alamgir and Lienhard's correlation is presented in Fig. (1.3) as the solid line for a temperature of 270 C. In the same figure, we have also plotted (circles connected by dashed line) the locus of the liquid depressurization history in Brown's experiment No. 36. The ordinate of each circle was determined by the local pressure measurement which when subtracted from the saturation pressure at the inlet temperature provides the local degree of overpressure or underpressure. The abscissa, which is a measure of the local depressurization rate was calculated from the expression

$$\frac{dp}{dt} = \frac{dp}{dz} \cdot \frac{dz}{dt} = \frac{\dot{m}^3}{\rho^2 A^4} \cdot \frac{dA}{dz} \tag{1.4}$$

where $\dot{m}$ is the mass flow rate, A the local cross-sectional area and dA/dz the variation of A with the axial distance z.

In Fig. (1.3), the region below the horizontal axis ($p_s - p \leq 0$) represents a subcooled liquid condition, the region between the solid curve predicted by Alamgir and Lienhard's correlation and the horizontal axis represents a superheated liquid condition, and the solid curve is the onset of flashing. If we follow the lines of the experimental points for Run 36 (Brown, 1961), we observe that at pressure taps 3, 4, and 5 the fluid is subcooled, between taps 5 and 6 (throat), the conditions cross inception line. A similar representation is also depicted in Fig. (1.4) for Run No. 51 (Brown, 1961) where $T_o = 286$ °C. This time the state of Taps 1, 2 are subcooled but close to saturation, at Taps 3, 4, and 5, the liquid becomes superheated, but once again the flashing inception line is crossed between Taps 5 and 6 (throat). The locus of a fluid particle moving from inlet to throat in the converging section of the nozzle depicts that as it gets into smaller cross sectional areas, the local dp/dt increases and the fluid element finds itself in a region which can sustain a higher pressure undershoot (higher superheat). At the throat or close to the throat, dA/dz from geometry, and dp/dz for single phase flows, go from negative to positive. At the point where dp/dz $\geq$ 0 or dA/dz $\geq$ 0 the liquid can not sustain any superheat and relaxes with the flashing inception. The dp/dt at the throat for Fig.

Figure (1.3) - Comparison of the Flashing Inception Predicted by Alamgir (1979) (solidline) With the Locus of the Liquid Depressurization History (circles connected by dashed line) in Brown's Nozzle (Run 36). (BNL Neg. No. 11-665-79).
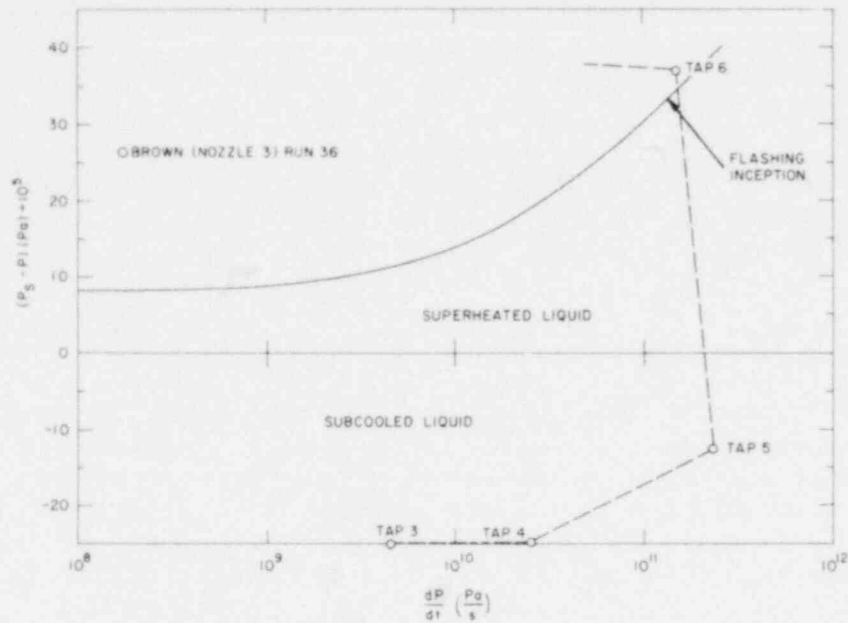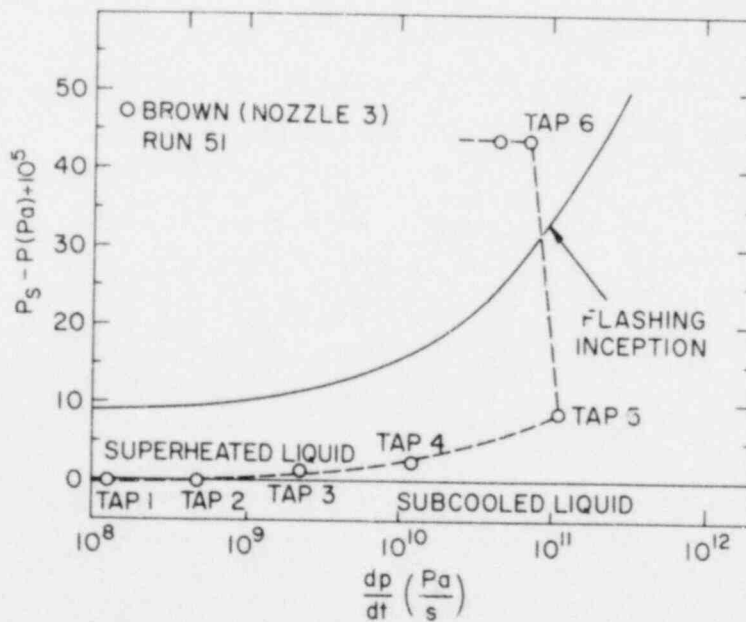

Figure (1.4) - Comparison of the Flashing Inception Predicted by Alamgir (1979) (solid line) With the Locus of the Liquid Depressurization History (circles connected by dashed line) in Brown's Nozzle (Run 51). (BNL Neg. No. 11-662-79).

(1.3) and (1.4) was calculated from Eq. (1.4) with a dA/dz value calculated by a second degree polynominal considering the upstream tap locations 5 and 4.

A similar representation of the pressure undershoot as predicted by Alamgir and Lienhard's correlation and the locus of a fluid element in the converging part of the nozzle are presented in Fig. (1.5) for BNL experiments 76, 77, 78, and 79. All these experiments were conducted at an inlet temperature of ~ 100 $^{\circ}$C and at various inlet mass fluxes as reported previously. The depressurization rates of the BNL experiments ranged from 10^6-10^8 Pa/s, which were much lower than the ones of Brown, 10^8-10^{11} Pa/s. The BNL depressurization rates are below the limit of Alamgir and Lienhard's correlation. In these low depressurization rates < 10^8 Pa/s, Alamgir-Lienhard's correlation predict a constant undershoot which depends on the temperature but is independent of the depressurization rate. The experimental data existing in the literature that they tried to correlate in these low ranges had an unexplained wide scatter. Although their correlation was assumed to apply in the low depressurization rates, some additional static depressurization experiments are needed to verify the validity of the correlation in this range. The important observation to be highlighted from Fig. (1.5) is that the flashing inception line is always crossed between Taps 24 and 25 (throat).

Thus from two approaches, discharge coefficient and static depressurization onset, we have demonstrated that in all of the experimental data analyzed for converging-diverging nozzles with various degrees of subcooled inlet, flashing inception occurs very close to the throat, and the mass flux under these conditions can be predicted with the single phase discharge coefficient concept.

A similar reasoning can be applied to the friction dominated pipe flow experiments (Reocreux, 1974). In this case, the local depressurization rate is constant for a given mass flux and can be expressed as

$$\frac{dp}{dt} = \frac{dp}{dz} \cdot \frac{dz}{dt} = f \frac{G^3}{2\rho^2 D} \tag{1.5}$$

where G is the mass flux, f the friction coefficient, ρ the density, and D the pipe diameter. As seen in Fig. (1.6), the depressurization rates of the Grenoble experiments, 10^4 to 10^6 Pa/s, are lower than the BNL experiments and are below the range of applicability of Alamgir and Lienhard's correlation. In Fig. (1.6), the pressure undershoot calculated from the correlation are once again independent of the depressurization rate, but depend strongly on the inlet temperature. The open circles are the onset points as determined (Wu, 1979) from the void fraction measurements of Reocreux data (1974) for experiments conducted at 116 $^{\circ}$C and 125 $^{\circ}$C. The vertical dashed lines present the locus of a fluid element in a pipe flow, from subcooled downstream conditions to the onset of flashing. The experimentally determined onset points lie below the onset predictions of Alamgir and Lienhard

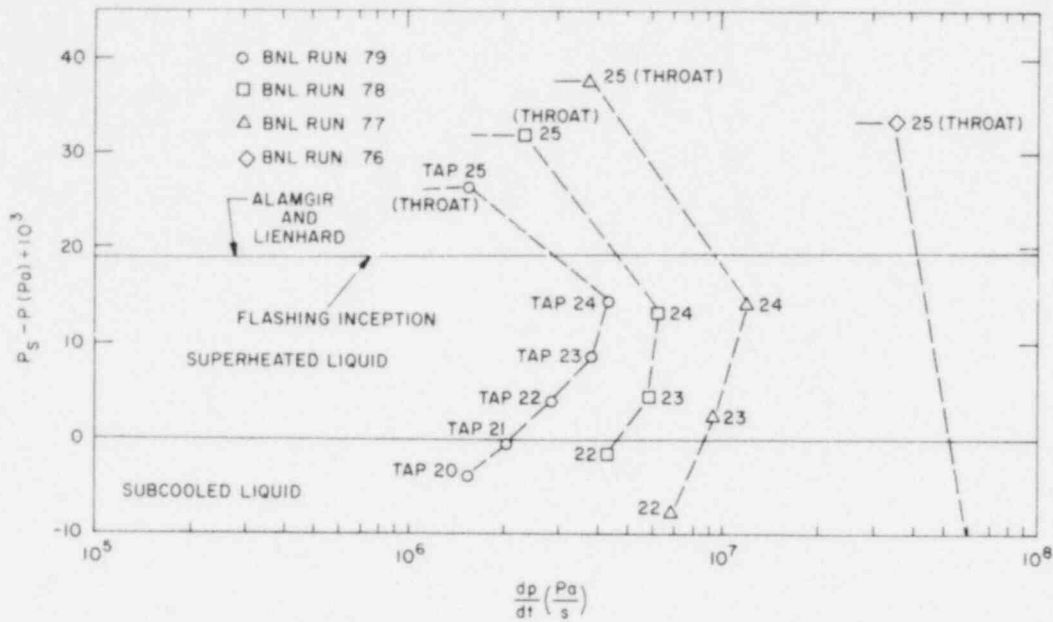Figure (1.5) - Comparison of the Flashing Inception Predicted by Alamgir (1979) (solid line) With the Locus of the Depressurization History in BNL's Nozzle (Runs 76,77,78,79). (BNL Neg. No. 11-663-79).
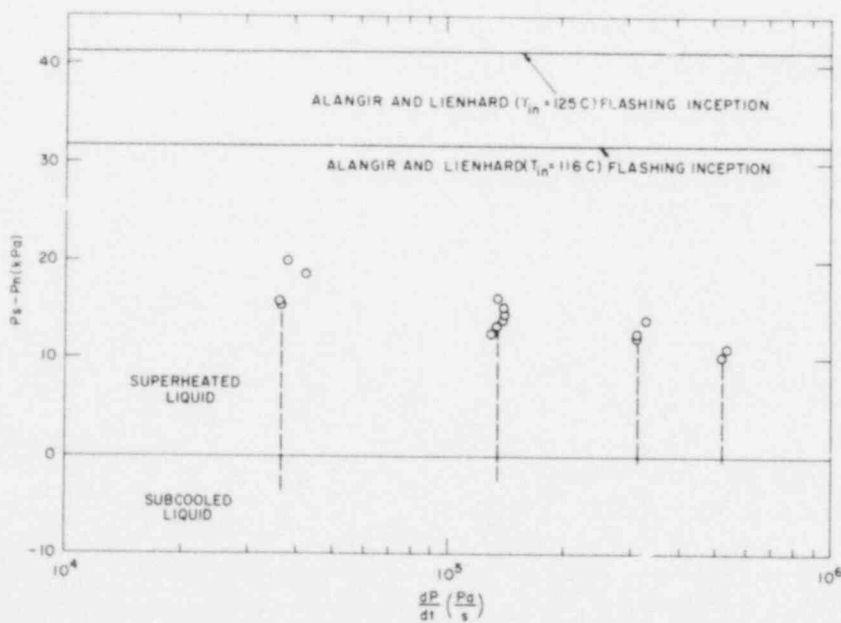

Figure (1.6) - Comparison of the Flashing Inception Predicted by Alamgir (1979) (solid lines) With the Locus of the Depressurization History in Reocreux' Pipe Experiments. (BNL Neg. No. 11-666-79).

Rohatgi (1975) has carried out such a calculation for flashing flow of liquid nitrogen and compared his results to the experiments of Simoneau (1975). There are two unknown parameters in the heterogeneous nucleation equations used by Rohatgi and Reshotko, one the number of effective nucleation sites per unit volume, the other being a function of the contact angle between liquid nitrogen and the surface of the heterogeneity. These unknown parameters were determined by "best fits" to the experimental data.

On the other hand, the Oswatitsch integral has been used successfully in condensation studies (see, e.g., Wegener 1977). In the latter case, the nucleation is homogeneous and the functional form of J is known, and the point of onset of condensation of a large number of substances in flows with a wide range of cooling rates (counterpart of the depressurization rate here) are successfully correlated.

It was to determine the growth rate term in the Oswatitsch integral, $m(z,\zeta)$, that Jones (1976) analyzed the growth of vapor bubbles in variable pressure fields applicable to the flashing process. The difficulty still remained, however, of determining the nucleation site density characteristics. It was this difficulty which led Saha (1978) and Wu (1979) to pursue an alternate approach. Rather than solving the Oswatitsch integral (Eq. 1.6) directly, attention was focussed on the subsequent growth of the vapor bubbles generated by nucleation, and the following approximate equation for the local vapor generation rate was derived,

$$\Gamma_v = C_\Gamma \frac{k_\ell}{\sqrt{a_\ell t}} \cdot \frac{(T_\ell - T_s)}{L} \beta \tag{1.7}$$

where β is given

by   when

$\beta = \alpha^2,$ $0 < \alpha \le 0.3,$

$\beta = 0.3^{2/3} = 0.4481$ $0.3 < \alpha \le 0.7,$

$\beta = (1 - \alpha)^{2/3}$ $\alpha > 0.7,$

where k_ℓ and a_ℓ are the thermal conductivity and diffusivity of the liquid, T_ℓ and T_s are the local temperatures of the liquid and vapor (assumed saturated) and L the latent heat, C_Γ is an undetermined parameter, t was of course the age of the voids with respect to the inception point in the Lagrangean coordinate system. The solution of Eq. (1.7), when applied to a specific problem required the following information which is unknown a priori:

a. the onset of flashing or inception point, z_{NVG}, which is

usually under nonequilibrium conditions and constitutes the origin of the time scale t for the bubble growth history.

b. The initial void fraction, α_o, at the point of inception.

c. The constant C_Γ, which has the dimension of inverse length and is proportional to the cube root of the number of bubbles generated at the inception point.

This above-mentioned conduction controlled vapor generation rate was applied to the experimental data of Reocreux (1974), and the values of the three unknown parameters, z_{NVG}, α_o and C_Γ were determined by the "best fit" to the void data. In reality, z_{NVG}, α_o, and C_Γ are all related to each other. If the nucleation rate J was known, and the Oswatitsch integral was solved independently, the values of the C_Γ, α_o and z_{NVG} will be provided as parts of the solution. Since the nucleation rates J for flashing flows are not known, a solution of the Oswatitsch integral is as yet not available. Two approaches were undertaken in order to solve the growth integral as presented in Eq. (1.6):

(1) The first approach consists in solving and integrating Eq. (1.7) by independently determining the unknown parameters. The onset of flashing or inception point z_{NVG}, should be fixed from an "empirical onset" correlation. The Alamgir-Lienhard (1979) correlation relating the pressure undershoot below p_{sat} at the inception point, to the reduced initial temperature and depressurization rate is used to determine the onset point or z_{NVG}. Once the inception point pressure is determined, following the reasoning of Alamgir and Lienhard, one could calculate the critical radius at the onset pressure and the only free parameter left will be the packing density of bubbles at inception. A value chosen for this free parameter will in turn fix α_o and C_Γ for the specific conditions. With the above determined values of the parameters z_{NVG}, α_o and C_Γ, one can now use Eq. (1.7) and its solution will provide the full details of the nonequilibrium transitional region where vapor generation takes place. This method is being followed now.

(2) A second approach to the solution of the same problem involves a study of the limiting cases. The relationship between conditions across a nonequilibrium vapor generating zone is one such possible method that was attempted. The reasons for seeking such a realtionship can be summarized as follows:

The flashing of a superheated liquid under nonequilibrium conditions seemed to appear as a process analogous to chemical reactions or condensation in high speed gas flows. Bray (1959) showed that a reacting flow in a nozzle can be modeled successfully by an equilibrium flow down to a transition point (termed "sudden freezing point" by Bray), and the flow downstream of this point is frozen, i.e., no change in composition. A parallel approach was applied to condensing flows in supersonic

nozzles (Wegener 1977). Here the flow was assumed to be frozen (supersaturated) down to the inception point where a sudden transition to equilibrium occurred and the flow was considered to be in equilibrium and saturated downstream of the onset point. This method of approach for condensing flows was applied successfully except when the flow is too slow compared to the characteristic time of condensation.

Similar to the latter method described above, we wanted to find if such an approach could be applied to flashing flows. The flashing flow with a subcooled inlet can be considered as a frozen flow (superheated liquid) upstream of the inception point. The flashing inception generates a given amount of vapor and quickly returns the flow downstream to the equilibrium conditions. This method of solution where the jump conditions are applied across the transition zone at inception, does not give the details of what is happening inside but correlates the upstream and downstream properties of the flow. When applied to nozzle flows, an additional implicit assumption required of this method is that the transition region is narrow, which was true in reacting and condensing flows in nozzles. By the solution of the jump conditions, which seemed quite simple methematically, we expected it could give useful information on limiting cases and can form the basis of comparison with other methods of prediction.

In order to test this latter method as it might apply to our experimental data reported in the last Quarterly Progress Report (Abuaf 1979), we decided to divide the flashing flow of an initially subcooled liquid in a converging-diverging nozzle into three regions. In the first region, the liquid depressurizes, its local pressure falling below the saturation pressure. Although the liquid becomes superheated, there is still no vaporization. In this frozen region, it was assumed that the extrapolated values of the liquid properties from the subcooled region still apply. Then a certain critical superheat (or "underpressure") is reached, vapor generation starts under nonequilibrium conditions, and it continues in the next (second) region, called the transition region, gradually restoring thermodynamic equilibrium. At the end of this region, local thermodynamic equilibrium is established and a vapor-liquid saturated mixture is assumed to exist. Similar behavior is also found to exist in straight pipes where the inception superheat leads to a low void, nonequilibrium zone gradually tending to equilibrium. In the last of the three regions, the two-phase mixture undergoes equilibrum change and the flow remains in local thermodynamic equilibrium thereafter. The thermodynamic properties of the mixture are then given by the equilibrium equation of state, e.g., the steam table.

1.1.3 Relation of Thermodynamic States Across a Nonequilibrium Vaporization Region

Figure (1.9) shows schematically the one-dimensional case of this situation. The flow in the transition region is governed by the fluid dynamic and transfer equations and their solution is not available at this time. On the other hand, the relationship between the thermodynamic states across the
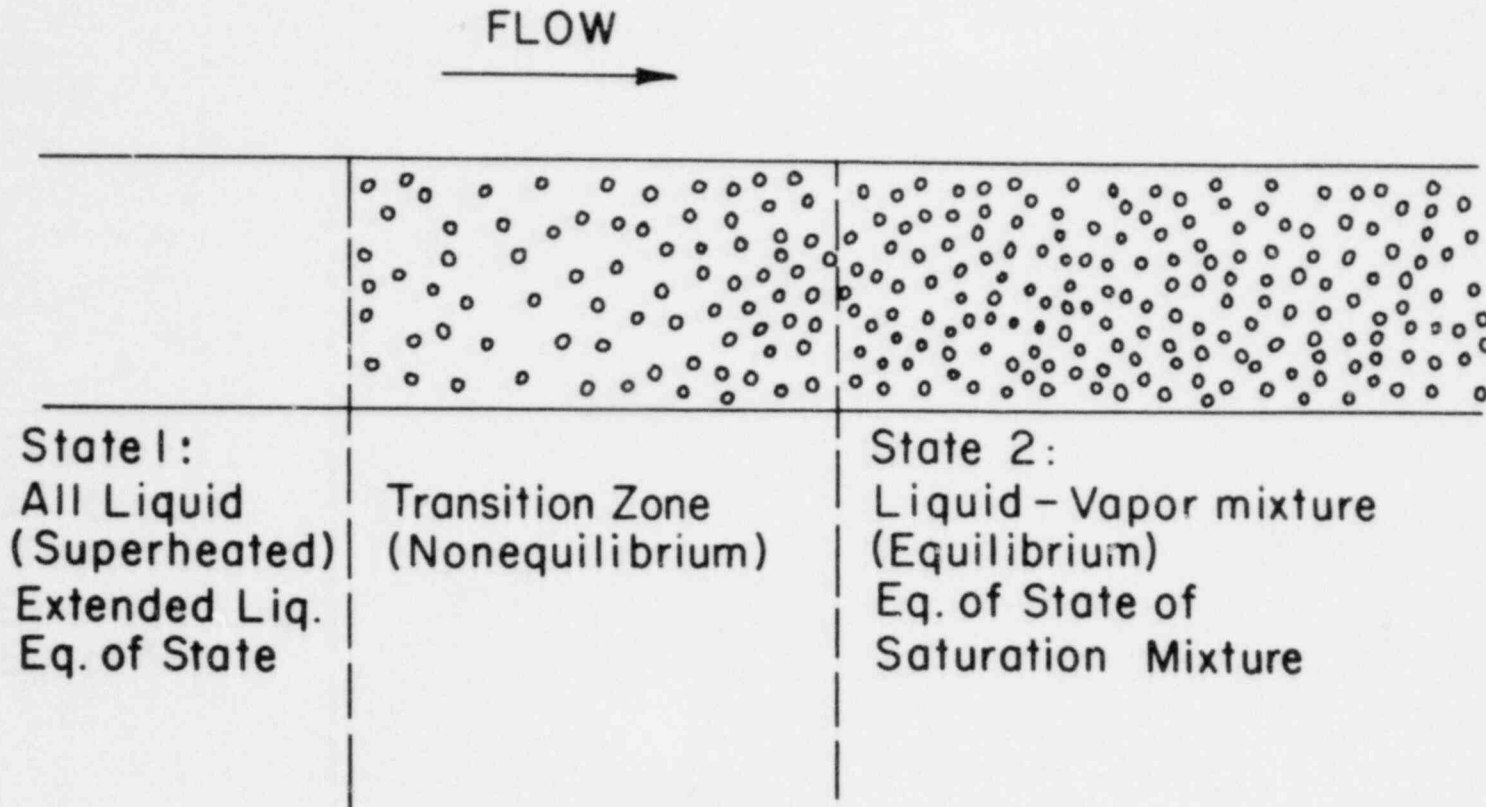
Figure (1.9) – Schematic Representation of a One-Dimensional Nonequilibrium Vaporization Front. (BNL Neg. No. 10-1202-79).

transition region are governed by the conservation equations and the respec-tive equations of state in regions 1 and 2 (See Fig. 1.9). Thus, for one-dimensional steady flows in a constant area duct and adopting a coordinate system in which the transition region is stationary, we have

Continuity: $\quad \rho_1 u_1 = \rho_2 u_2 = G,$ $\hspace{5cm}$ (1.8)

Momentum: $\quad p_1 + \rho_1 u_1^2 = p_2 + \rho_2 u_2^2 = F,$ $\hspace{4cm}$ (1.9)

Energy: $\quad h_1 + \frac{1}{2} u_1^2 = h_2 + \frac{1}{2} u_2^2 = H,$ $\hspace{4cm}$ (1.10)

State: $\quad h_1 = f_\ell (p_1, \rho_1),$ $\hspace{5cm}$ (1.11)

$\quad\quad\quad\quad h_2 = f_{2\phi} (p_2, \rho_2),$ $\hspace{5cm}$ (1.12)

where f_ℓ represents the extrapolated liquid equation of state and $f_{2\phi}$ the equation of state of the saturation mixture, and p, ρ, h, and u are the pressure, density, enthalpy, and velocity, respectively.

In region 2, the mixture is assumed to be a homogeneous one and there is no slip between the phases. The constants of motion G, F, and H are the total mass flux, the thrust per unit area and the total (stagnation) enthalpy of the flow. The constancy of F and H is the result of the additional assumption of the absence of heat loss (or gain) and friction at the walls. We point out, however, that interphase exchanges of energy and/or momentum in the transition region do not violate this assumption and they may be present.

Equation (1.8) to (1.10) are identical to the well-known equations of normal shock waves in classical gasdynamics, with the exception that for classical shock waves, the gas on either side obeys the same equation of state. Our problem is more akin to shock waves with chemical reaction, detonation or combustion fronts, where two different sets of equations of state are needed. Since vapor will be present in region 2 but not in 1, we expect $\rho_2 < \rho_1$. It follows from Eq. (1.3) that $u_2 > u_1$, whence $p_2 < p_1$ from the momentum Eq. (1.9), and $h_2 < h_1$ from the energy Eq. (1.10). Thus, we expect in the transition region the fluid changes from an initial, super-heated state at (p_1, ρ_1) to a final saturation state at a lower pressure and density. In order for this transition to be realized physically, the ad-ditional requirement on the entropy, $s_2 \geq s_1$ must be satisfied. In contrast to shock waves in gasdynamics, as we shall see later, the physical require-ment of pressure and density decrease across the transition zone does not necessarily violate the second law of thermodynamics.

Relationship between the thermodynamic variables in states 1 and 2 may be obtained by eliminating the velocities u_1 and u_2 in Eqs. (1.8) to (1.10).

Thus, from Eq. (1.8) and (1.9), we have

$$P_1 + \frac{G^2}{\rho_1} = P_2 + \frac{G^2}{\rho_2} ,$$

or

$$-G^2 = \frac{P_1 - P_2}{\frac{1}{\rho_1} - \frac{1}{\rho_2}} .$$

In terms of the specific volume $V \equiv 1/\rho$, we have

$$-G^2 = \frac{P_1 - P_2}{V_1 - V_2} . \tag{1.13}$$

This is the well-known Rankine relation which says the slope of the straight line connecting the initial and final states on a p-V diagram must be negative and is equal to $(-G^2)$. That the pressure and density must decrease across the transition region is consistent with real values of G. Next, the velocities u_1 and u_2 may be elminated between the continuity and energy Eqs. (1.8) and (1.10), and the Rankine Eq. (1.11) may subsequently be substituted to eliminate the mass flux to yield

$$h_1 - h_2 = \frac{1}{2} (P_1 - P_2) (V_1 + V_2) . \tag{1.14}$$

With the equations of state (1.11) and (1.12), this equation gives an expression of p_2 in terms of V_2 for a prescribed set of p_1 and V_1. This is the well-known Hugoniot relation, and the curve $p_2 = p_2(V_2)$ on a p-V diagram is called the Hugoniot adiabat.

A particular, limiting case seemingly representative of a few of our experiments will be examined first. If the transition zone is relatively narrow, then the Rankine-Hugoniot relations may be considered to give the "jump" conditions across a vaporization front, much like a shock wave. For transition zones of finite thickness, such an approach yields only a crude approximation. However, for flashing flow in a constant area duct, it will provide limiting conditions for the flow and thermodynamic variables. In addition, useful physical insight may be gained in such a simplified treatment. If one assumes that the transition zone has vanishing thickness, the above equations may be applied to flows in a variable area duct. Under this assumption, the flashing flow in a converging-diverging nozzle may be computed in a three-step manner: The liquid first depressurizes without phase change to a pressure below the saturation value. Here the flow may be

treated by the Bernoulli equation or isentropic expansion up to the transition point, whereupon flashing begins and the fluid property "jumps" from a supersaturated state to an equilibrium two phase state. Finally equilibrium expansion once again is used to describe the flow downstream of the "jump".[*] Thus, the jump condition is needed to provide the initial condition of the flow in the last region of equilibrium expansion. In a few of the experiments evaluated, (Fig. 1.5 in Abuaf 1979), this indeed seemed to be close to that observed. Homogeneous equilibrium seem to do a good job downstream of flashing inception. In most situations, however, broad zones of nonequilibrium were observed and an extension of this method will be required.

The Hugoniot relation has been evaluated for conditions of our Run 77. Assuming $p_1 = 80$ kPa (in this experiment, saturation occurred at $p \gtrsim 99$ kPa), we found the Hugoniot curve displayed in Fig. (1.10). Here in contrast to gas shocks, the "pre-jump" state (p_1, V_1) does not lie on the Hugoniot curve because $(p_2 = p_1, V_2 = V_1)$ is not a solution of Eq. (1.14) since $h_1 \neq f_{2\phi}(p_1, \rho_1)$. A straight line connecting (p_1, V_1) to a point on the intersection of the Rankine and Hugoniot curves gives a possible solution of the Eqs. (1.8) to (1.10). The slope of the straight line will give the value of $(-G^2)$ required to support such a discontinuity in a stationary configuration. Here the direction of change is from upper left to lower right in the p-V plane, and the process is formally analogous to that of a deflagration wave (Courant 1948, Hayes 1960). We note that there is a point, labeled the Chapman-Jouguet (C-J) point, on the Hugoniot adiabat which is tangent to the Rankine line (also shown) there. This is the steepest Rankine line that can be drawn for the Hugoniot curve corresponsing to (p_1, V_1), and represents the maximum mass flux allowed by Eqs. (1.8), (1.9) and (1.10). Rankine lines for lower mass fluxes will be less steep and may intersect the Hugoniot at two points, one above and one below the C-J point, corresponding to the weak and strong deflagration solutions, respectively. The existence of strong deflagrations is doubtful, but combustion waves may be described as weak deflagrations (Courant 1948, Hayes 1960). In a weak deflagration, the fluid enters the transition region with a subsonic velocity, and it leaves the transition again with a subsonic velocity with respect to a_2, the speed of sound in region 2. At the Chapman-Jouguet point, $u_2 = a_2$. The entropy s_2 increases along the Hugoniot adiabat from the point $p = p_1$ to the C-J point, reaching a maximum there and decreases thereafter. The entropy s_2 corresponding to the state downstream of a weak deflagration transition is greater than s_1.
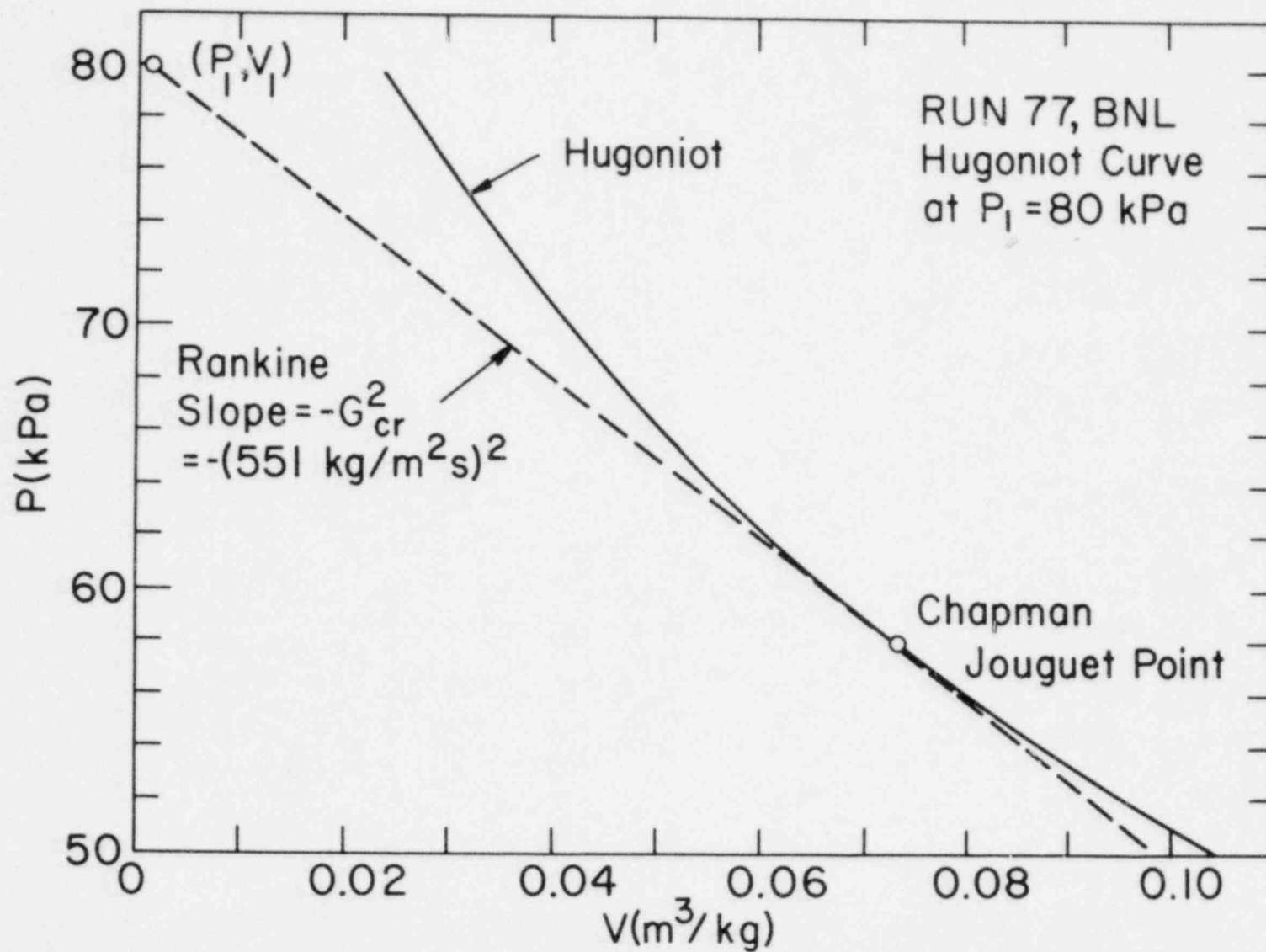
---

[*] Schrock, et al. (1977) has used a similar approach.

Figure (1.10) – Hugoniot Curve of Vaporization Front at p_1 = 80 kPa in BNL Flashing Experiment Run 77 (Abuaf 1979). (BNL Neg. No. 10-1201-79).

For our purpose, we note that the maximum allowable mass flux while still maintaining a stable vaporization front satisfying the assumptions laid down here is given by the slope of the Rankine line at the C-J point. In Fig. (1.10), we see $G_{max} = G_{cr} = 551 \text{ kg/m}^2\text{s}$ at the point in the nozzle where $p_1 = 80$ kPa for superheated liquid flow. Results of similar calculations for other values of p_1 in Run 77 are summarized in Fig. (1.11). Here we have plotted the experimental value of G determined from the measured nozzle inlet conditions and effective flow area distribution from hydrodynamic calibration for an isentropic expansion of the liquid to superheated states.[*] The mass fluxes G_{cr} at the C-J point are indicated by the circles. An intersection of the G_{cr} and G_{exp} curves would have provided a solution for the location of the flashing front where the experimental mass flux may be accommodated and the flashing front maintained steadily. Unfortunately, such an intersection was not found for our Run 77. Indeed, G_{cr} is too low by a factor of 10-20. Figure (1.12) presents results of similar calculations for an experiment published by Schrock, Starkman, and Brown (1977), calculations for the experimental conditions of Reocreux's (1974) Run 423 led to the results in Table (1.1).

TABLE (1.1)

COMPARISON OF THE CRITICAL MASS FLUXES CALCULATED BY THE JUMP CONDITIONS AND THE EXPERIMENTAL VALUE MEASURED BY REOCREUX (RUN 423)

p_{in} = 243 kPa		$p_{sat}(T_{in})$ = 210 kPa
T_{in} = 121.9 $^{\circ}$C		$G = G_{in}$ = 4.38 Mg/m^{2}s = const
p_1 (kPa)	G_{cr} (Mg/m^{2}s)	G_{exp} (Mg/m^{2}s)
175	1.11	4.38
190	1.32	4.38
200	1.51	4.38

Again, no solutions were found either for Schrock's or Reocreux's experiment although the discrepancy was smaller. The failure to reach a solution in these calculations has led us to reconsider the basic assumption

---

[*]It was found that isentropic expansion of the liquid is almost identical to an isothermal, incompressible flow such as given by the Bernoulli equation.
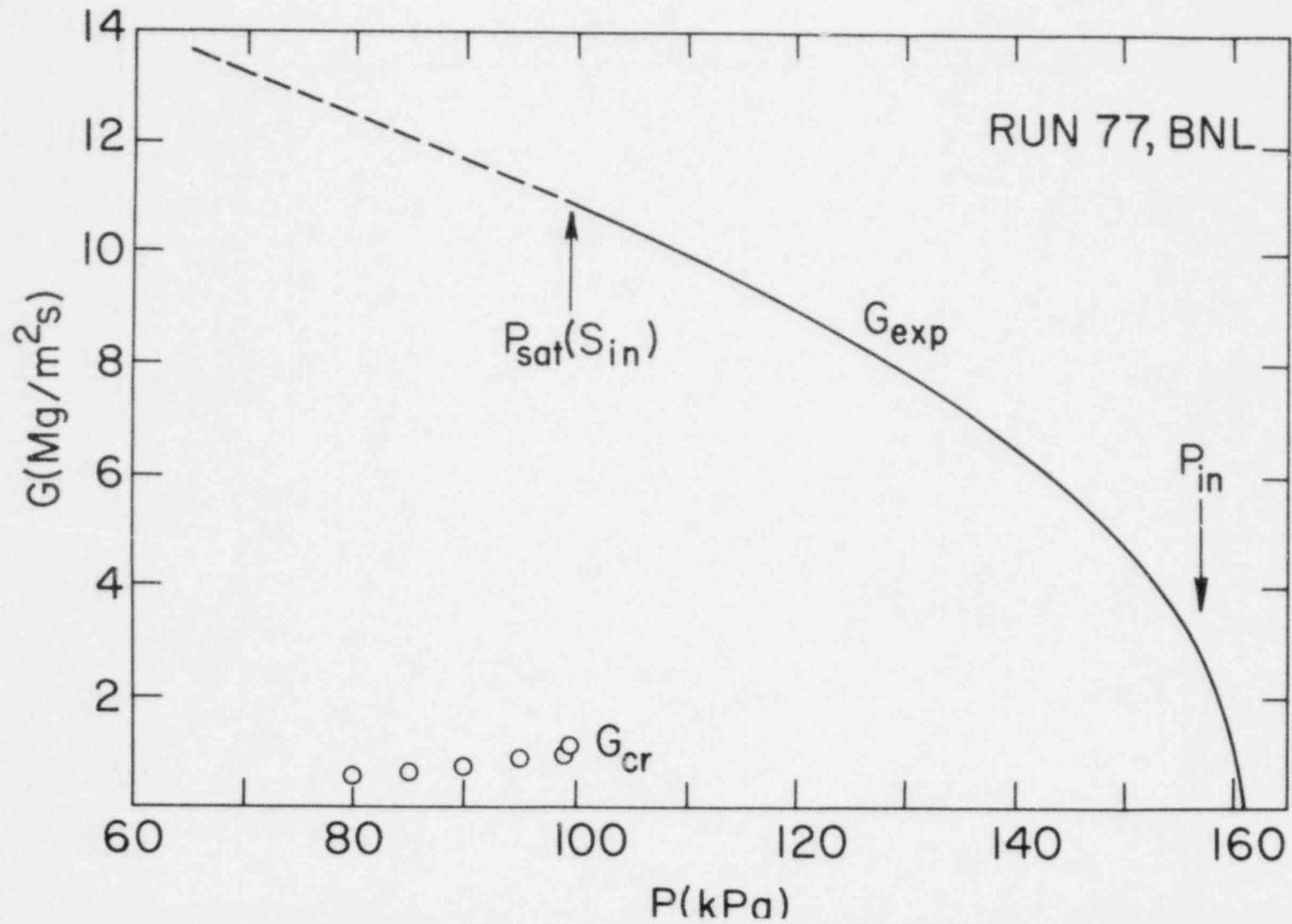
Figure (1.11) - Comparison of Experimental Mass Flux G_{exp} and Critical Mass Flux G_{cr} at C-J Point in BNL Experiment Run 77. (BNL Neg. No. 10-1200-79).
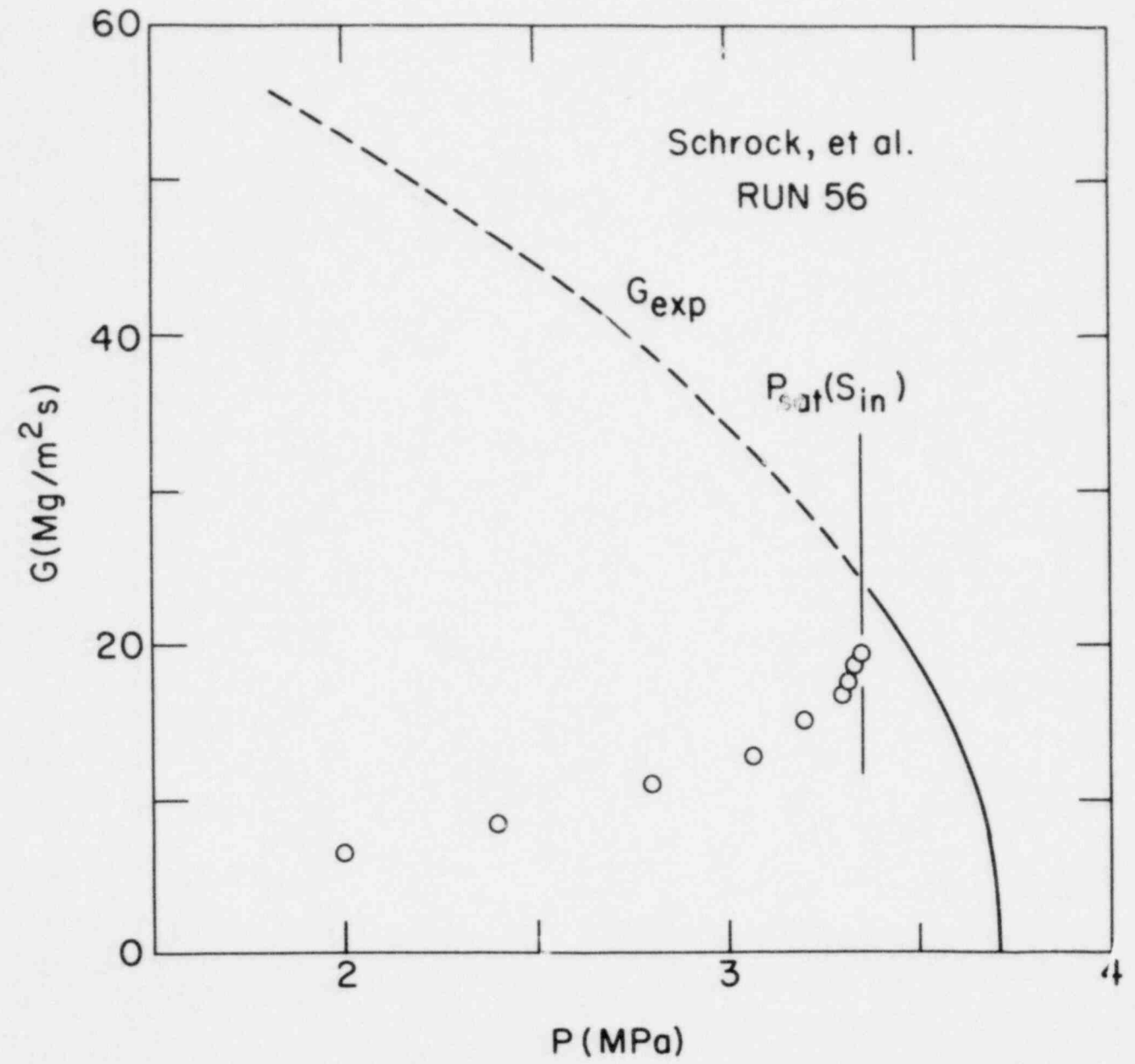
Figure (1.12) - Comparison of Experimental Mass Flux G_{exp} and Critical Mass Flux G_{cr} at C-J Point in Run 56 of Schrock, et al. (BNL Neg. No. 10-1203-79).

underlying this first treatment. Perhaps the most serious condition assumed that may not be realistic is the complete kinematic and thermodynamic equilibrium of the post-jump condition.

The effects of velocity slip between the liquid and vapor in region 2 have been examined. Preliminary results indicate a small improvement in the G_{cr} values, but far from being adequate. The other effects, e.g., thermodynamic nonequilibrium, variable flow area, need to be examined and further work on the slip effect are needed before the feasibility of this approach may be conclusively stated.

1.2 Flashing Experiments (G. A. Zimmer, B.J.C. Wu, J. H. Klein, and N. Abuaf)

The five beam gamma densitometer presented in Fig. (1.13) was used to measure the transverse distribution of the chordal averaged void profiles at various axial locations in the test section under flashing conditions. The five sources have 3 mm diameter collimation holes and the sources are placed at 10.2 mm center-to-center distances. Figure (1.14) depicts a horizontal and a vertical cross section of the source holder. The second additional row of five sources were added for the possible future purpose of measuring cross correlations in the flow direction. The detector holder presented in Fig. (1.15) has a similar 3 mm diameter collimation holes and contains the set of five Cadmium Telluride detectors mounted on a small circuit board. As observed in Fig. (1.16), which is a pictorial representation of the test section TS 2, the source and detector holders are connected to the two arms of a traversing mechanism, which is driven by two motors and which allows the controlled motion of the gamma densitometer system both in the axial and transverse directions.

First the nozzle was calibrated while empty (full of air) at 27 axial locations. At every axial location the five sources-detectors system was moved in 2.54 mm steps in the transverse direction to cover a total distance of 1.27 cm for each source. Figures (1.17 a,b,c,d,e) show the results of this calibration normalized with respect to the centerline value as a function of radial distance at five different axial locations. The output of each source is represented by a different symbol. The fifth and sixth measurements for each source provide a repetition of the first and second measurements of the next source. Thus, during each run there are some measurements which are repeated at the same location by two different source-detector systems. As one moves from the test section inlet to the throat, the effect of the tube radius becomes more important on the distributions. Each data point presented was an average of 10 consecutive γ-measurements of nine seconds duration each. The full calibrations of the nozzle at the same axial locations were also performed with the nozzle full of cold water (20 $^{\circ}$C), with and without the pump running to check if there were any vibration problems with the electronics. The results of the full cold (room temperature) calibration are presented in Fig. (1.18 a,b,c,d,d) at the same axial locations as presented in Fig. (1.17). Here also the counts of the five sources were normalized by the value at the centerline. In these figures,
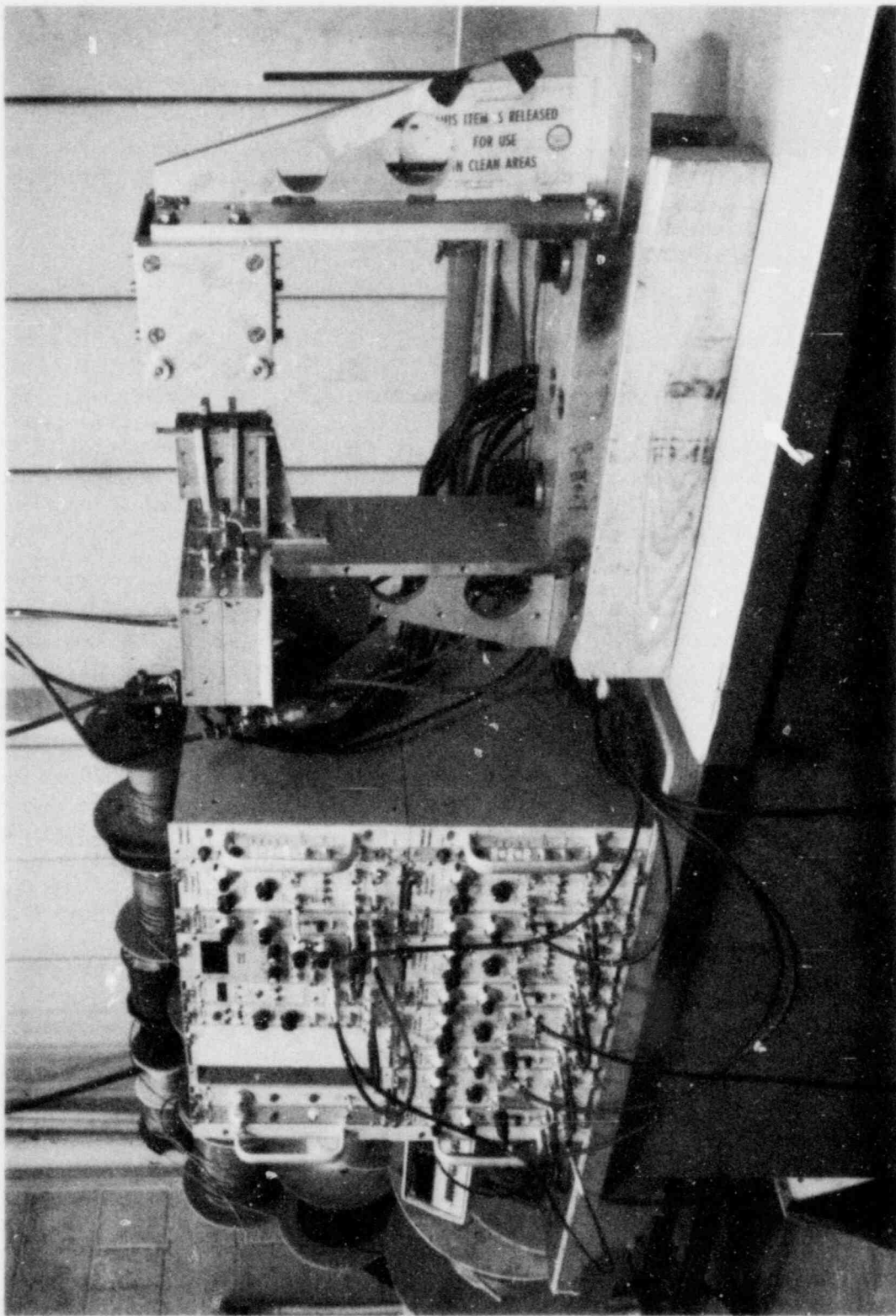
Figure (1.13) - Photograph of the Five Beam Gamma Densitometer (BNL Neg. No. 6-1079-79).
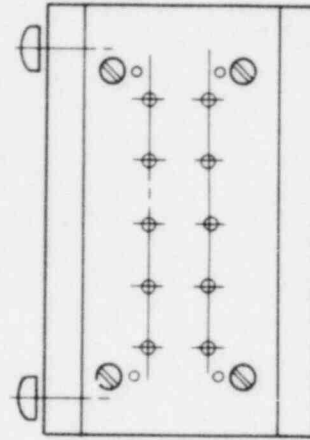
DETECTOR

LEAD

1 cm
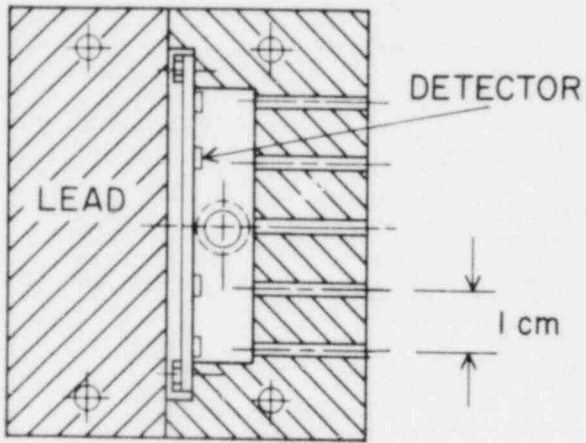
Figure (1.15) - Schematic Representation of the Detector Holder. (BNL Neg. No. 11-671-79).

SOURCE

SCALE
1 cm

SOURCE
HOLDER

LEAD

ALUMINUM

HORIZONTAL
CROSS-SECTION

VERTICAL
CROSS-SECTION

Figure (1.14) - Horizontal and Vertical Cross Sections of the Source Holder. (BNL Neg. No. 11-667-79).

26

DENSITOMETER TRAVERSING MECHANISM

SIGHT PORT

PRESSURE TAP TUBING (49)

VENTURI

STEPPING MOTOR TYPICAL

GAMMA DENSITOMETER DETECTOR SHOWN SOURCES OPPOSITE SIDE

POSITION TRANSDUCERS

INLET STRAIGHTENING SECTION

FLOW
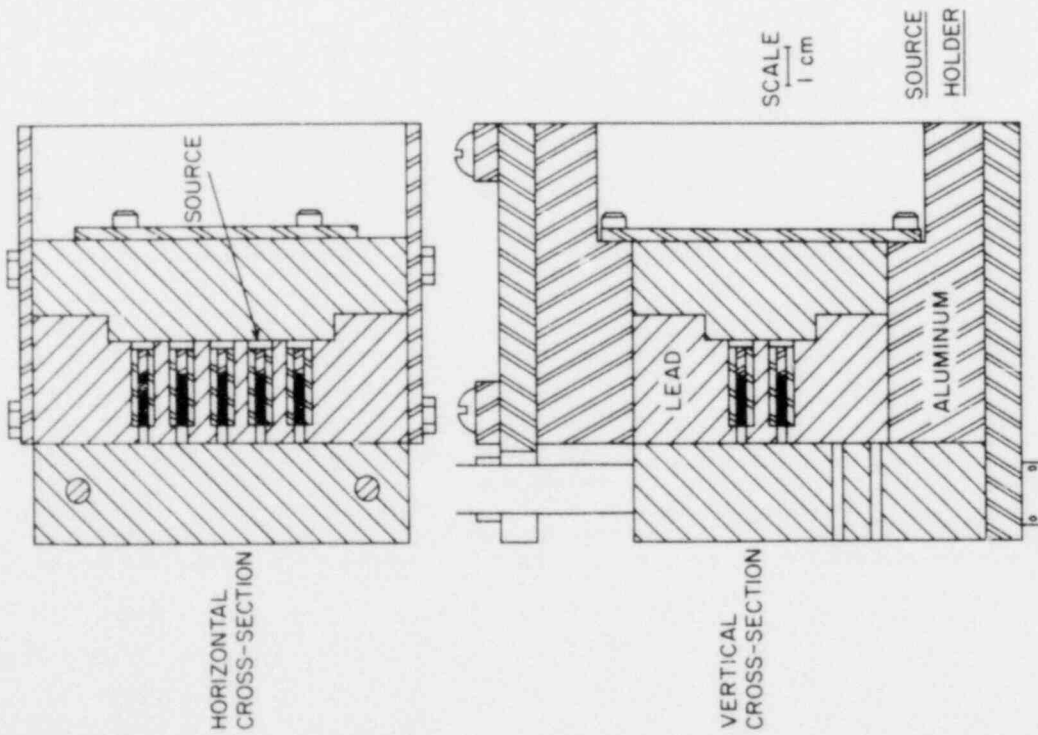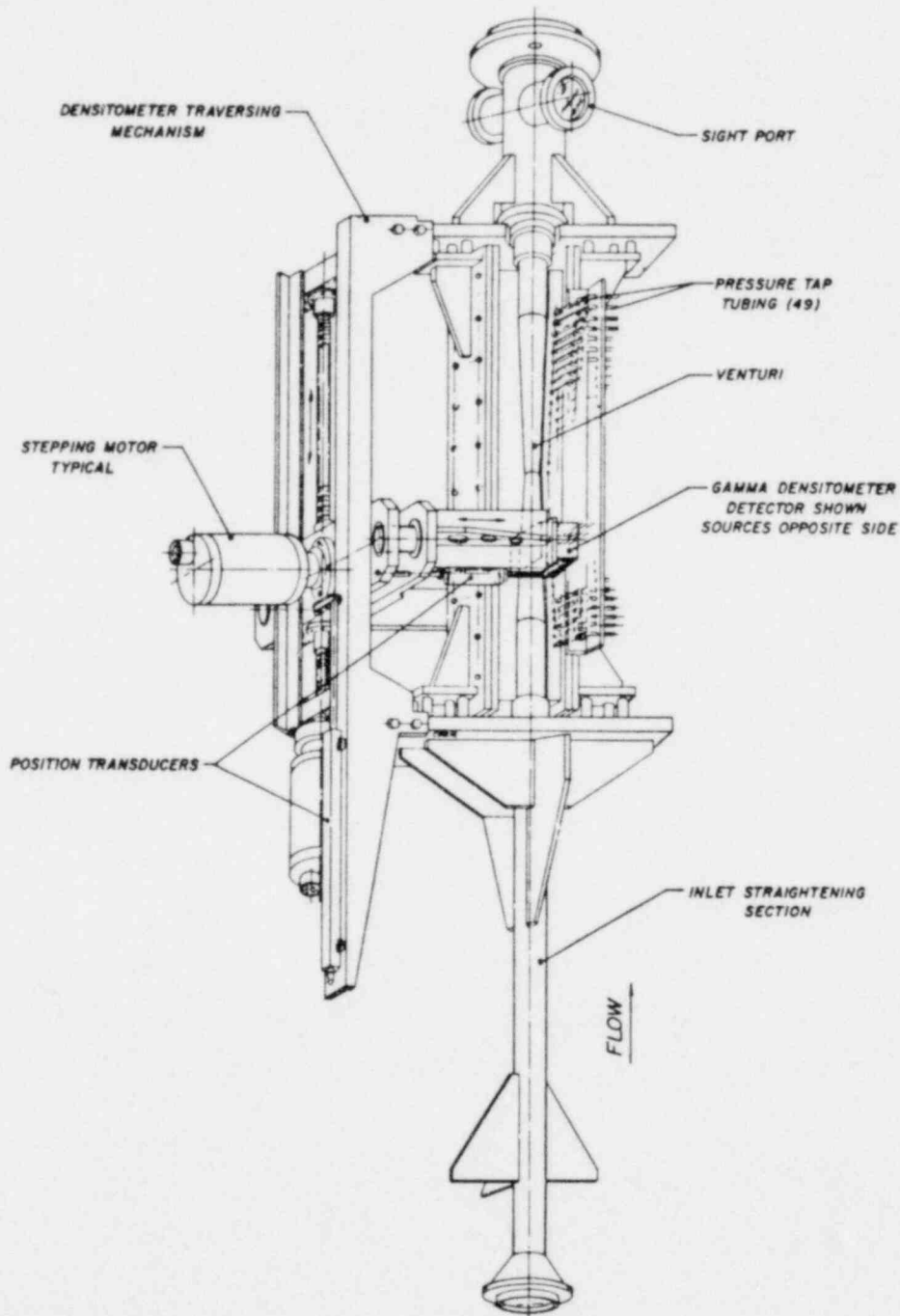
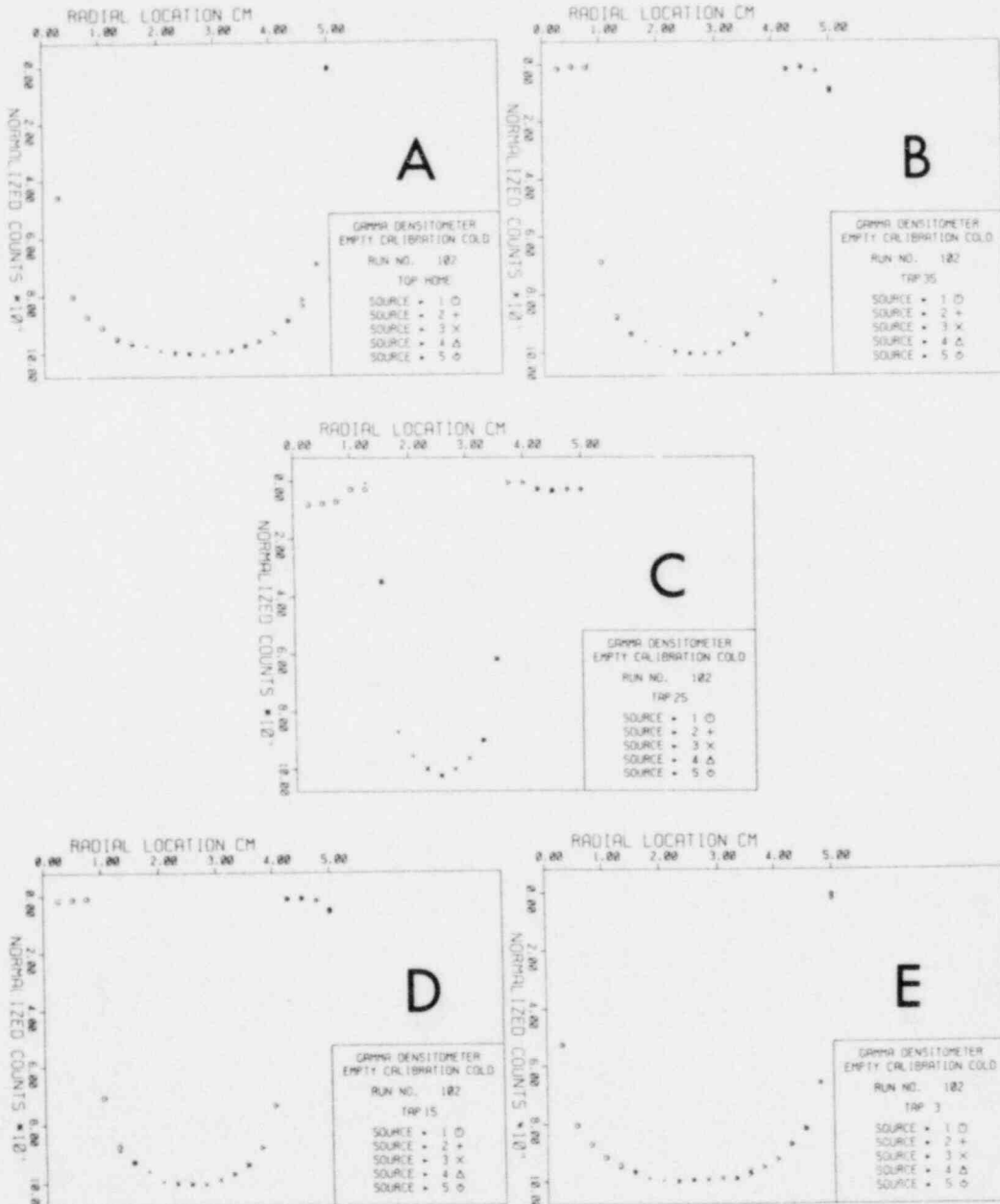Figure (1.16) – Schematic Representation of the Test Section. (BNL-Neg. No. 10-1406-79).

Figure (1.17) – Normalized Empty Calibrations of the Test Section at Five
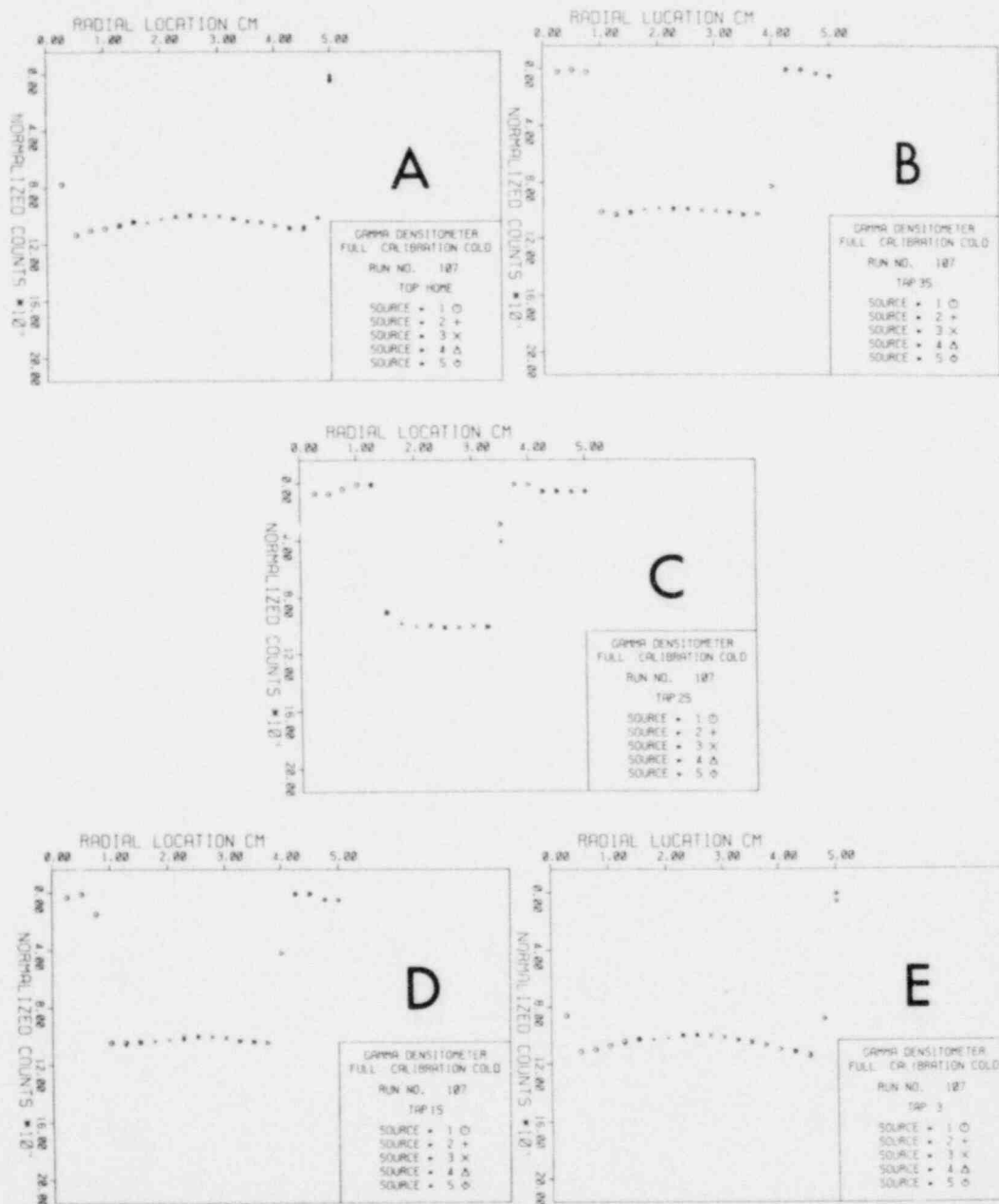Different Axial Locations. (BNL Neg. No. 10-1413-79).

Figure (1.18) - Normalized Full Calibrations of the Test Section at Five Different Axial Locations. (BNL Neg. No. 10-1414-79).

the repeatibility of the results with two consecutive sources at the same location is clearly observable. One fact to be pointed out in these calibration runs is the symmetry in the results as the sources and detectors move across the test section, both in the empty and full calibrations. Another important observation is the lack of scatter in the results and the source detector overlap repeatability.

After the calibration of the gamma densitometer system, a few cold hydrodynamic calibration runs were performed and the results were compared with the previously determined effective areas. No difference outside of the experimental scatter was observed.

The full calibration of the test section was also repeated while the loop was running at low flow rates and 100 ^{o}C inlet temperature conditions. The automatic computer controlled positioning of the sources included the information to calculate the linear expansion of the test section. The results of these runs are being analyzed presently in detail.

Flashing experiments were conducted at 100 ^{o}C and 125 ^{o}C inlet temperatures and several mass fluxes according to the general test matrix. While most of the results are still being evaluated, preliminary results of Run 130 will be presented in this present quarterly. The transverse distributions of all the chordal-averaged void fractions are presented in Fig. (1.19) (1.20) (1.21) (1.22) (1.23) (1.24) (1.25). In these figures, the chordal void fraction averaged from the ten sets of 9 s measurements are plotted vs. the radial (transverse) location. Once again, different symbols are used to represent each source. The dashed lines represent the boundaries of the nozzle at that axial location and the horizontal line depicts the area-averaged void fraction for that axial location, calculated from

$$\bar{\alpha} = \frac{\Sigma \alpha_i \Delta A_i}{\Sigma \Delta A_i}$$

(1.15)

where ΔA_i is the chordal area defined by the gamma beam thickness at a given transverse location and α_i is the chordal averaged void fraction measured at the same location. Some preliminary observations from this set of data is that the void profile is not symmetrical with respect to the axis of the tube. The void profiles seem to imply the presence of a low void fraction core, surrounded by a high void fraction envelope close to the walls. As we get closer to the throat of the nozzle, the area-averaged void fraction decreases and gets closer to the all liquid single phase value. The scatter of the points close to the wall and upstream of the throat could be attributed to the fact that at the extreme locations, close to the walls, the calibrations (both empty and full) change drastically, thus a small error in the location ($\sim$ 0.005 ") can cause a large error in the voids measured, since the difference between full and empty is also small in the same region. All

Figure (1.19) - Radial Distributions of the Chordal Averaged Void Fractions at Various Axial Locations Obtained by the Five Beam Gamma Densitometer for Run 130. (BNL Neg. No. 10-1405-79).

Figure (1.20) – Radial Distributions of the Chordal Averaged Void Fractions at Various Axial Locations Obtained by the Five Beam Gamma Densitometer for Run 130. (BNL Neg. No. 10-1411-79).

Figure (1.21) - Radial Distributions of the Chordal Averaged Void Fractions
at Various Axial Locations Obtained by the Five Beam Gamma Densitometer
for Run 130. (BNL Neg. No. 10-1412-79).
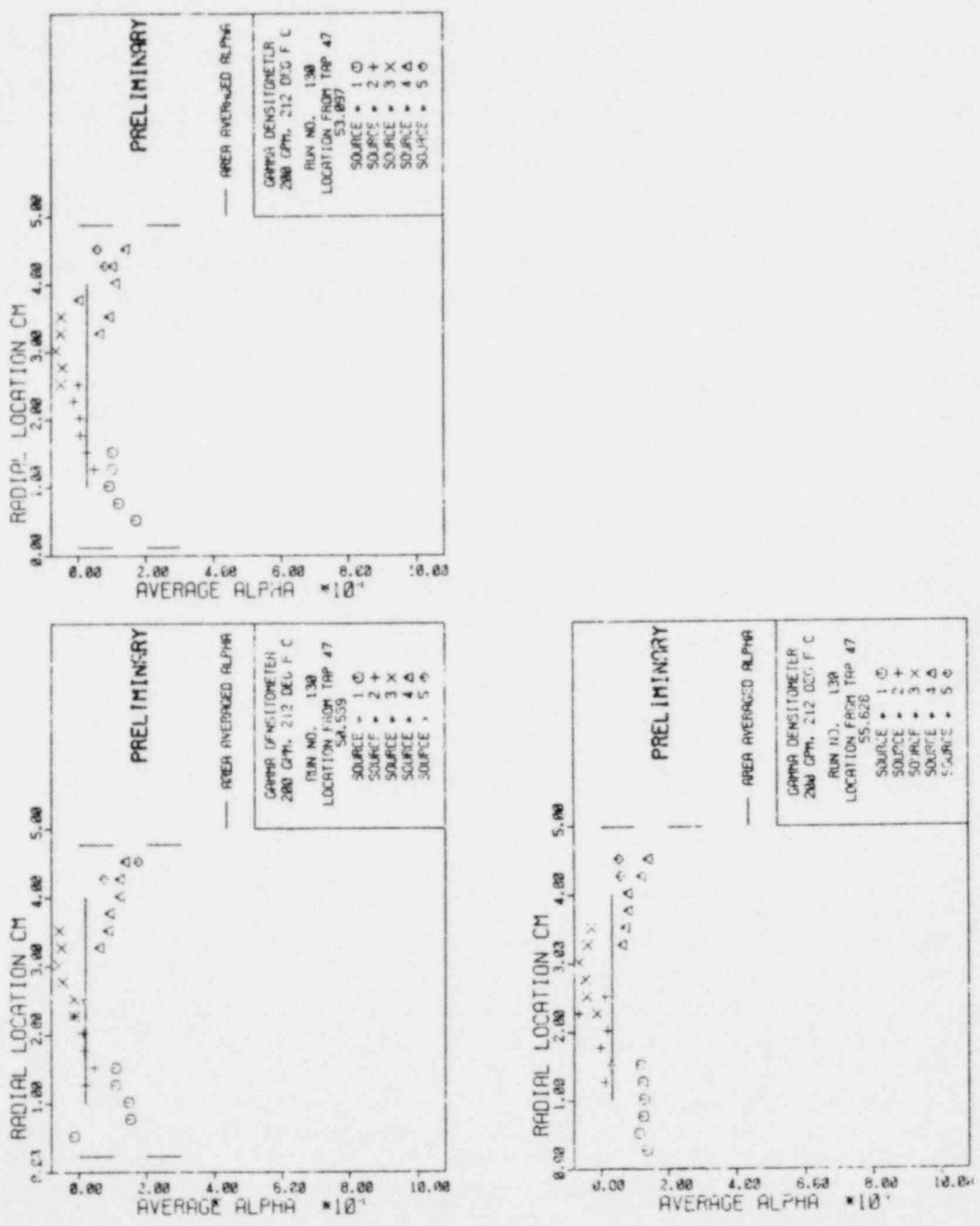
Figure (1.22) – Radial Distributions of the Chordal Averaged Void Fractions
at Various Axial Locations Obtained by the Five Beam Gamma Densitometer
for Run 130.   (BNL Neg. No. 10-1400-79).

Figure (1.23) – Radial Distributions of the Chordal Averaged Void Fractions at Various Axial Locations Obtained by the Five Beam Gamma Densitometer for Run 130. (BNL Neg. No. 10-1403-79).
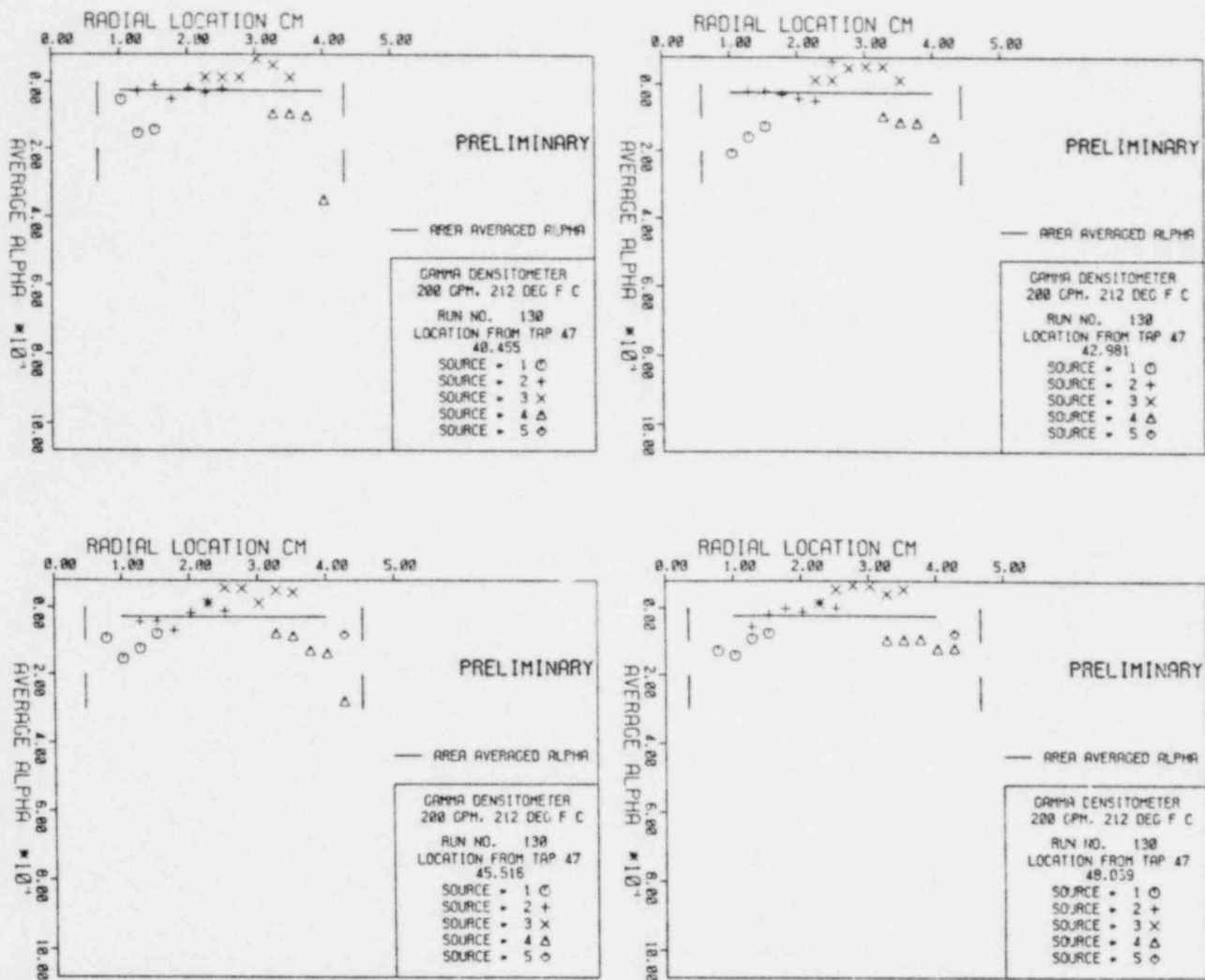
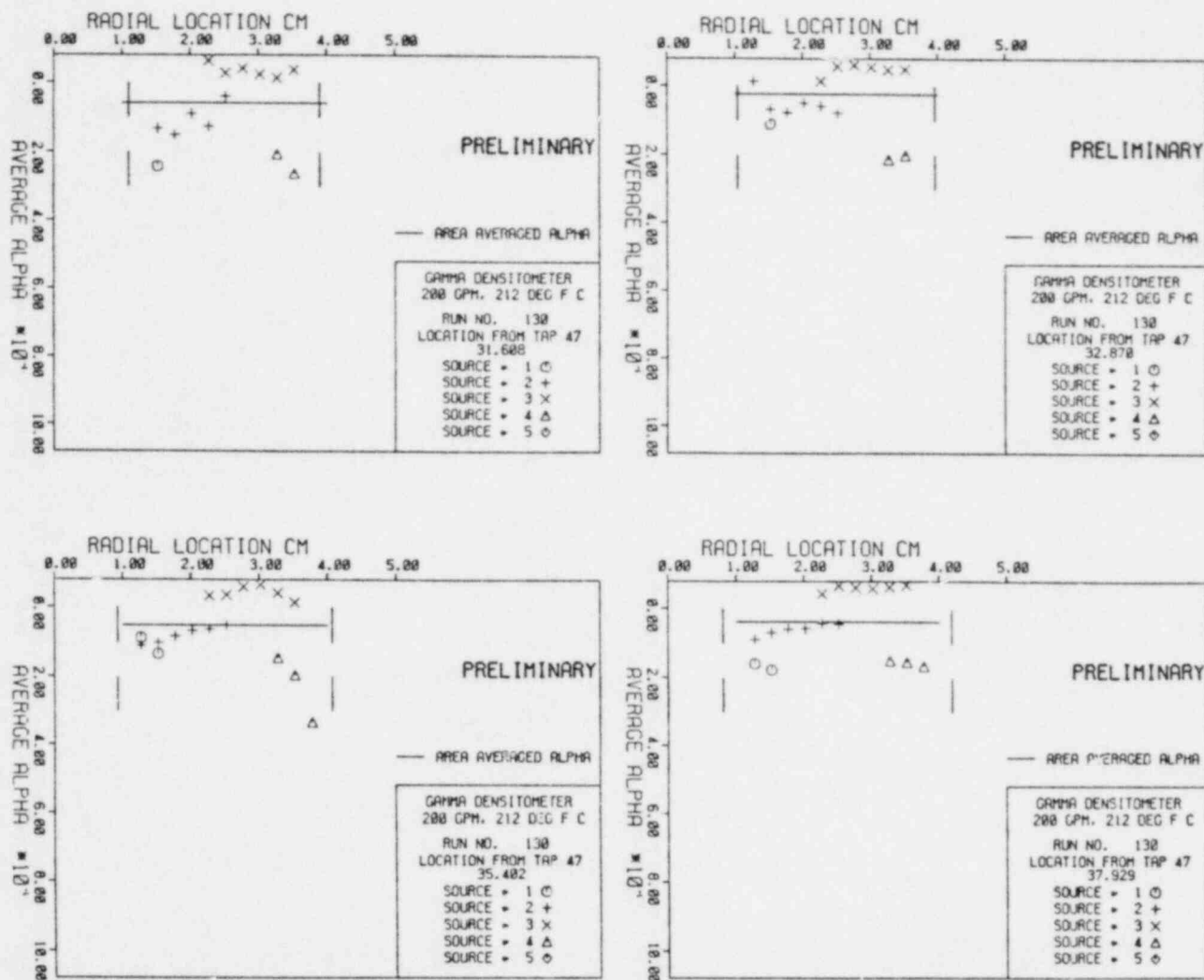Figure (1.24) – Radial Distributions of the Chordal Averaged Void Fractions at Various Axial Locations Obtained by the Five Beam Gamma Densitometer for Run 130. (BNL Neg. No. 10-1407-79).

RADIAL LOCATION CM

0.00　1.00　2.00　3.00　5.00

AVERAGE ALPHA *10⁻¹

PRELIMINARY

— AREA AVERAGED ALPHA

GAMMA DENSITOMETER
200 GPM, 212 DEG F C

RUN NO.　130
LOCATION FROM TAP 47
20.230
SOURCE • 1 ⊙
SOURCE • 2 +
SOURCE • 3 ×
SOURCE • 4 △
SOURCE • 5 ◇

RADIAL LOCATION CM

0.06　1.00　2.00　3.00　5.00

AVERAGE ALPHA *10⁻¹

PRELIMINARY

— AREA AVERAGED ALPHA

GAMMA DENSITOMETER
200 GPM, 212 DEG F C

RUN NO.　130
LOCATION FROM TAP 47
22.756
SOURCE • 1 ⊙
SOURCE • 2 +
SOURCE • 3 ×
SOURCE • • △
SOURCE • 5 ◇

RADIAL LOCATION CM

0.00　1.00　2.00　3.00　5.00

AVERAGE ALPHA *10⁻¹

PRELIMINARY

— AREA AVERAGED ALPHA

GAMMA DENSITOMETER
200 GPM, 212 DEG F C

RUN NO.　130
LOCATION FROM TAP 47
24.022
SOURCE • 1 ⊙
SOURCE • 2 +
SOURCE • 3 ×
SOURCE • 4 △
SOURCE • 5 ◇

RADIAL LOCATION CM

0.00　1.00　2.00　3.00　5.00

AVERAGE ALPHA *10⁻¹

PRELIMINARY

— AREA AVERAGED ALPHA

GAMMA DENSITOMETER
200 GPM, 212 DEG F C

RUN NO.　130
LOCATION FROM TAP 47
25.290
SOURCE • 1 ⊙
SOURCE • 2 +
SOURCE • 3 ×
SOURCE • 4 △
SOURCE • 5 ◇

Figure (1.25) - Radial Distributions of the Chordal Averaged Void Fractions
at Various Axial Locations Obtained by the Five Beam Gamma Densitometer
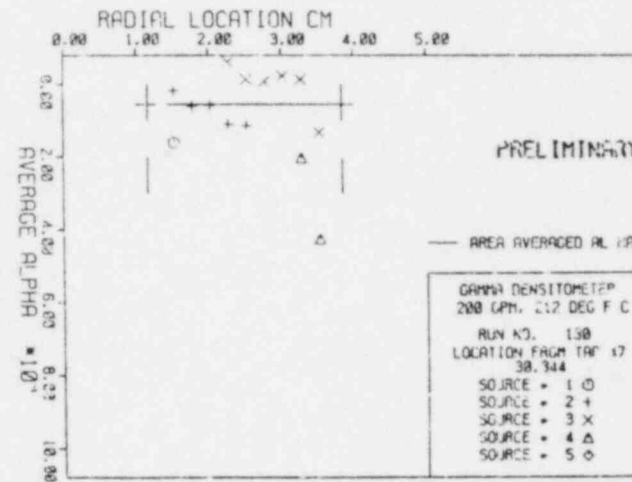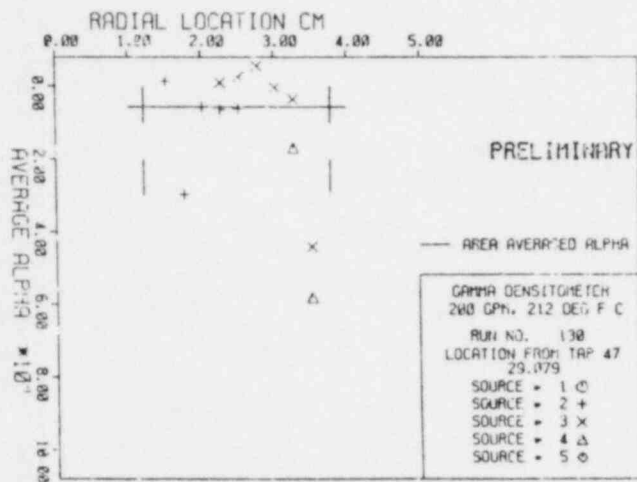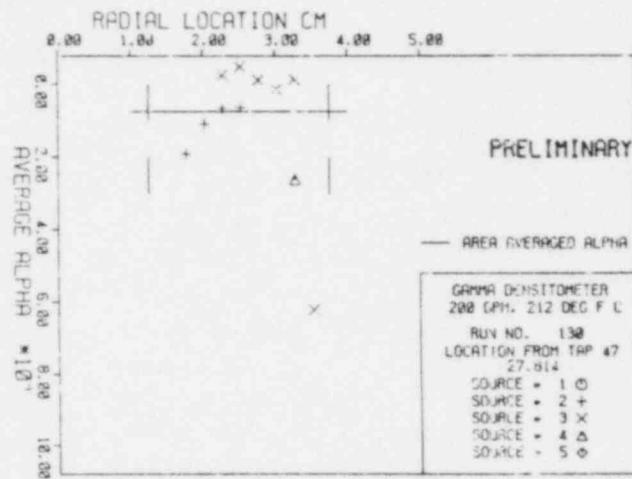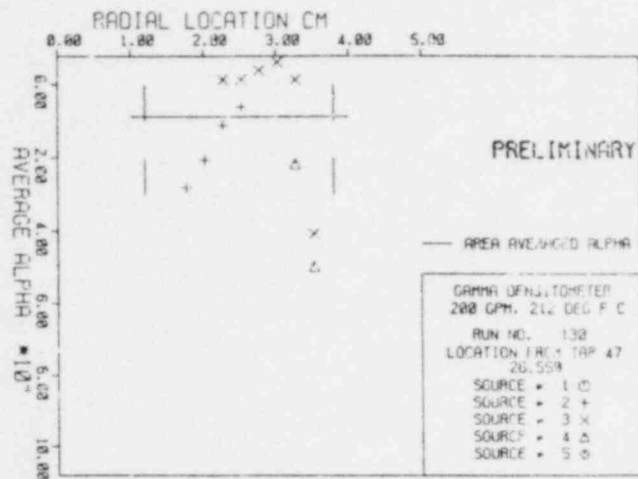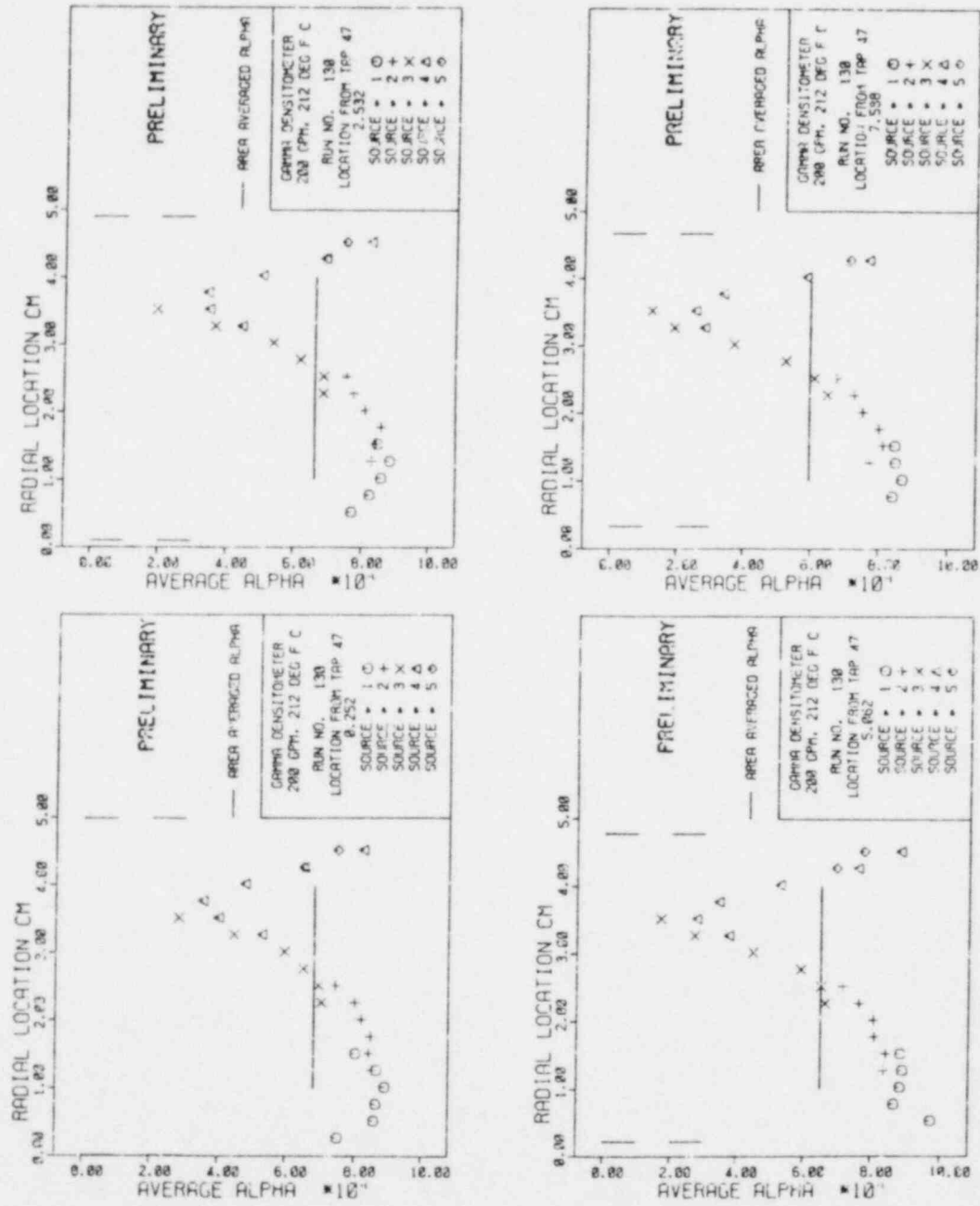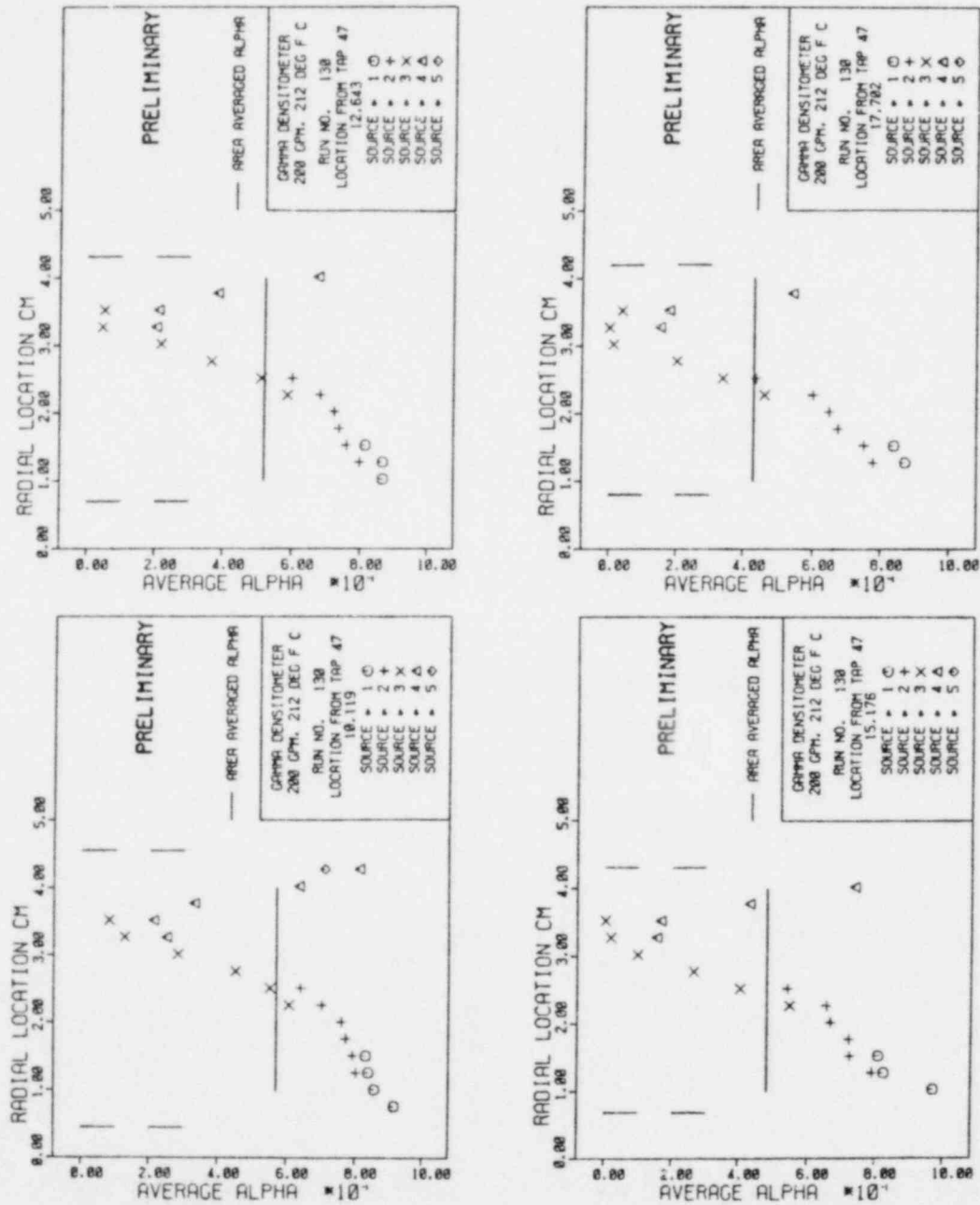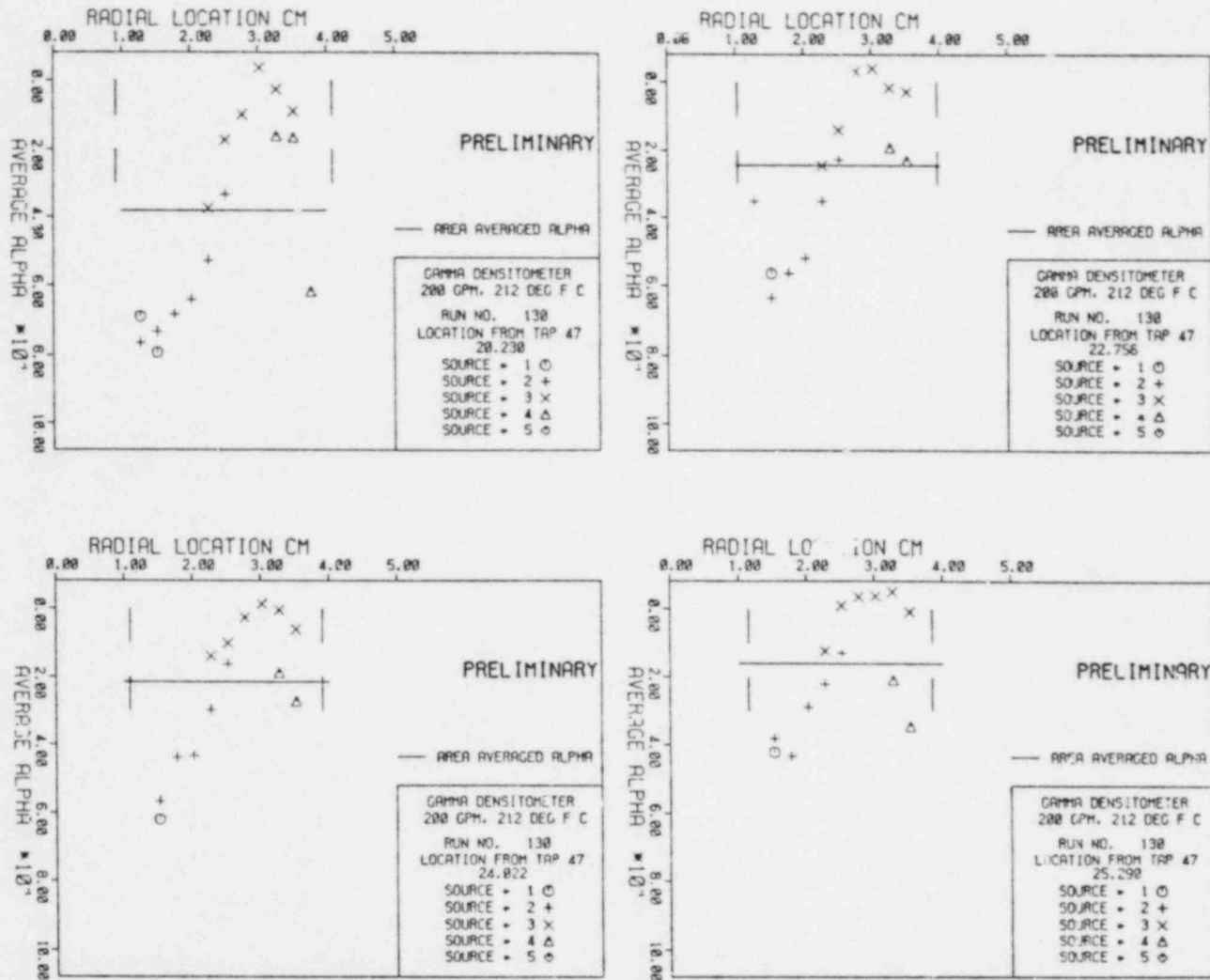for Run 130.　(BNL Neg. No. 10-1410-79).

our data recorded include absolute locations in the transverse direction and
therefore the proper corrections can be applied as a function of location.
The difference in the void fraction measured by two neighboring sources at
the same location near the nozzle centerline is a result of the unsteady
nature of the flashing flow, not scatter since no scatter was present in the
empty and full calibrations.

One of the experiments, Run 130, was analyzed and the pressure distribu-
tions, area-averaged void profiles and vapor generation rates calculated from
the data are presented in Fig. (1.26). In the same figure, these data are
also compared with TRAC P1A predictions and homogeneous equilibrium calcula-
tions. The static pressure distributions presented show the accurate repeati-
bility of the experimental data under similar conditions with a time period
of more than six months between them. Runs 76, 761, and 762 were made
previously in the second series of runs and the details are discussed by
Zimmer (1979). Run 130 is the new experiment where the chordal-averaged void
fractions were recorded as a function of transverse locations and axial
locations. Both runs were performed under the same inlet conditions $G = 6040$
kg/m^2 s, $p_{in} \sim 395$ kPa and $T_{in} = 99.3$ ^{o}C in one case and 100 ^{o}C in

the other. The area-averaged void profiles depicted at each axial location
were obtained from detailed transverse profiles of chordal averaged void
fractions measured with the five beam gamma densitometer. These detailed
radial profiles were presented in Fig. (1.19) to (1.25) for various locations
upstream of the test section exit (Top Home). The open circles (Run 762)
which depict the results of the diametrical averaged void fractions confirm
that such diametrically averaged data are not representative of the area-
averaged values for this flow regime configuration. Any comparison of these
experimentally measured diametrical averaged void fraction [such as pre-
viously obtained in earlier tests at BNL or also at Grenoble (Reocreux 1974)],
to area-averaged void fraction predictions by various models can lead to
inaccurate conclusions. The static pressure distributions, the void pro-
files, and the vapor generation rates both from experiments and TRAC P1A
predictions seem to agree reasonably well for this specific experiment.
Since the pressure at the throat, the saturation pressure at the inlet
temperature and the onset of flashing are close to each other, this agreement
is expected. Similarly some simple homogeneous equilibrium calculations
performed seem also to predict the pressure distribution and void profiles
reasonably well. On the other hand, if the inception superheats are con-
siderably different, the resulting nonequilibrium can result in large differ-
ences between TRAC and experimental results.

Additional data were also recorded under various flashing conditions and
the results are being examined and compared to TRAC P1A predictions.

38
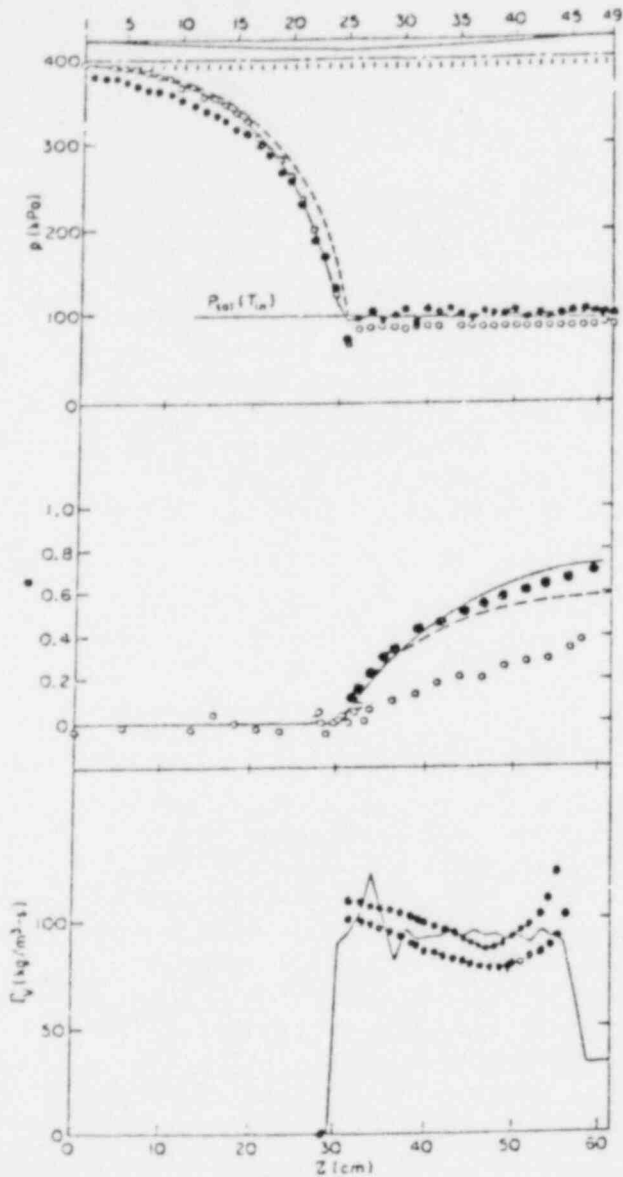
Pressure Distribution

Measured: ●   Run 130
               O   Run 761

Calculated: ——— TRAC

            - - - - Equilibrium

Void Fraction Distribution

Measured: ●   Run 130
                      Area Average

               O   Run 762
                      Diametrical Average

Calculated: ——— TRAC

            - - - - Equilibrium

Net Vapor Generation Rate

Deduced from Run 130: ●
(Upper trace for C_o = 1.1,
 lower trace for C_o = 1.0)

Calculated: ——— TRAC

Figure (1.26) - Comparison of TRAC Predictions and Homogeneous Equilibrium
Calculations With BNL Experiments. All Experimental Data Displayed Were
Obtained Under the Same Run Conditions: G_{in} 6040 kg/m^{2}s, p_{in} = 395 kPa,
T_{in} = 99.3 $^{\circ}$C. Runs 76, 761, and 762 Were Made Previously, and Details
Are Discussed in BNL-NUREG-26003; Run 130 is the New Experiment Where
Chordal Averaged Void Fractions Were Recorded as a Function of Transverse
Location and Axial Location.

REFERENCES

ABUAF, N. and JONES, O. C., JR., "Reactor Safety Research Programs, Quarterly Progress Report, April-June 1979, p.   , BNL-NUREG-   (1979).

ALAMGIR, Md., and LIENHARD, J. H., Personal communication (1979).

BRAY, K.N.C., " J. Fluid Mech., 6, 1-32 (1959).

BROWN, R. A., "Flashing Expansion of Water Through a Converging-Diverging Nozzle, UCRL-6665-T (October 1961).

COURANT, R. and FRIEDRICKS, K. O., Supersonic Flow and Shock Waves, Wiley, NY (1948).

HAYES, W. D., in Fundamentals of Gasdynamics, H. W. Emmons, Editor, Princeton Univ. Press, Princeton, NJ (1960).

JONES, O. C., JR. and ZUBER, N., "Evaporation in Variable Pressure Fields," Paper No. 76-CSME/CSChE, 16th National Heat Transfer Conference (1976).

JONES, O. C., Jr., "Flashing Inception in Flowing Liquids," BNL-NUREG-26134 (1979).

LEONHARDT, W. J. and ABUAF, N., "Reactor Safety Research Programs Quarterly Progress Report, April-June 1978, BNL-NUREG-50883, p. 158 (August 1978).

LEVINE, M. M. and JONES, O. C., Jr., "Thermal Reactor Safety Code Development, BNL Monthly Highlights for July 1979 (1979).

OSWATITSCH, K., "Kondensationserscheinungen in Uberschalldusen," Z. angew. Match. Mech. 22, 1 (1942).

SCHROCK, V. E., STARKMAN, E. S., AND BROWN, R. A., "Flashing Flow of Initially Subcooled Water in Convergent-Divergent Nozzles, J. of Heat Transfer, Trans. ASME, 99, pp. 263-268 (1977); erratum, J. of Heat Transfer, 99, p. 647 (1977).

SIMONEAU, R. J., Personal communication (1979).

SOZZI, G. L. and SUTHERLAND, W. A., "Critical Flow of Saturated and Subcooled Water at High Pressures, NEDO-13418 (July 1975).

REOCREUX, M., "Contribution a l'etude des debits critiques en ecoulements diphasiques eau-vapeur, These de Doctorat, University Scientifique et Medicale de Grenoble (1974).

ROHATGI, U. S. and RESHOTKO, E., "Nonequilibrium Two-Dimensional Flow in Variable Area Channels," Nonequilibrium Two Phase Flow, ASME (1975).

References (Cont'd)

WEGENER, P. P. and WU, B.J.C., "Gasdynamics and Homogeneous Nucleation," in Nucleation Phenomena, A. C. Zettlemoyer, Editor, p. 325-417 Elsevier, NY (1977).

WU, B.J.C., SAHA, P., ABUAF, N., AND JONES, O. C., JR., "A One-Dimensional Model of Vapor Generation in Steady Flashing Flow," BNL-NUREG-25709 (1979).

ZIMMER, G. A., et al., "Reactor Safety Research Programs, Quarterly Progress Report, October-December 1978, BNL-NUREG-50978, p. 162 (March 1979).

ZIMMER, G. A., et al., "Pressure and Void Distributions in a Converging-Diverging Nozzle With Nonequilibrium Water Vapor Generation," BNL-NUREG-26003 (April 1979).

ZUBER, N., STAUB, F. W., and BIJWAARD, G., "Vapor Void Fraction in Subcooled Boiling and in Saturated Boiling Systems," Proc. 3rd Int. Heat Trans. Conf., Vol. 5, p. 24 (1966).

2. RAMONA,IRT and RETRAN Code Modification and Evaluation

Considerable progress has been made in developing and implementing new component models for RAMONA-III. A model for the recirculation loop drive pump was developed and combined with the jet pump model previously done. These models are in the final stages of being "debugged" within the code. They have successfully executed as stand-alone packages. The steamline model has successfully executed both as a stand-alone code and within RAMONA-III. Results using this model have been verified by comparing them with an analytical solution for a special case and with experimental data from the Peach Bottom-2 Turbine Trip Tests. The steam separator model had been implemented prior to this reporting period. A rudimentary control and protection system has been implemented.

A new fuel rod heat conduction model was developed and implemented in the code. It takes into account clad heat capacity and non-uniform heat generation which were not considered in the original model. It has successfully run but only with a limited mesh.

New updates to the code were received from Scandpower and generated at BNL in order to correct and improve the code. A graphics capability is in the process of being developed.

A Peach Bottom-2 plant model was developed at BNL and a similar input deck was received from Scandpower. Calculations are being run with these data in order to understand what improvements might still be needed.

2.1 RAMONA Model Modification and Development

2.1.1 Jet Pump-Recirculation Loop Model

The BWR code RAMONA-III has been modified to calculate the pressure head produced by a recirculation pump. The head is then used by the jet pump model (see previous Quarterly Progress Report.) Both the jet pump and the recirculation pump models are based on LINFORD (1973).

Currently it is assumed that the pump motor power comes from the power plant directly. The equations will be modified in the future to model the pump motor power coming from a motor generator unit through a fluid coupler. The procedure is an extension of the present method and requires the knowledge of the response of the fluid coupler.

For the case of power coming directly from the power plant, LINFORD (1973) gives the following four nonlinear equations that must be solved.

$$T = K_{T1} n_p^2 + K_{T2} n_p m_p + K_{T3} (m_p + K_{T4} n_p)|m_p + K_{T4} n_p| \tag{1}$$

$$\Delta P_{RP} = K_{H1} \, n_p^2 + K_{H2} \, m_p + K_{H3} \, (m_p + K_{H4}) \, |m_p + K_{H4}| \qquad (2)$$

$$\frac{\pi J_p}{30 g_c} \frac{dn_p}{dt} = T_{e\ell} - T_m \qquad (3)$$

$$T_{e\ell} = \text{function } (n_p) \qquad (4)$$

The four unknown variables are n_p, $T_{e\ell}$, T_m, and ΔP_{RP}. T_m is the pump torque and ΔP_{RP} is the recirculation pump pressure head. Figure 2-16 of LINFORD (1973) is a curve of electrical torque, ($T_{e\ell}$) versus shaft speed (n_p). Both are expressed as percent of rated quantities. This figure provides the functional relationship, Equation (4), between $T_{e\ell}$ and n_p.

K_{Ti} and K_{Hi} ($i=1,\ldots,4$) are constants that can be obtained from the manufacturers curves. J_p is the pump motor inertia and is also given by the manufacturer; g_c is the gravitational constant. m_p is the flow rate through the recirculation pump and is assumed to be provided by the jet pump model.

Substituting Equations (1) and (4) into (3) and solving the ordinary differential equation for n_p will give ΔP_{RP}.

A set of subroutines has been written and executed to solve for n_p and obtain the new ΔP_{RP}. Before the equations were put into RAMONA-III, a stand-alone version was verified by driving the solution mechanism, both for steady state and transient modes of operation, with a small front-end "driver" routine.

This driver contained a curve representing the flowrate m_p as a function of time to use as input to the solution routines that obtain ΔP_{RP}. This curve, as well as all the pump characteristics, was obtained from a RELAP-3B run simulating the Peach Bottom reactor (Lu, 1979a).

Noting that at steady state $T_{e\ell} = T_m$, we can solve the combination of Equations (1) and (4) with a Newton-Raphson nonlinear equation solver. For the transient two methods have been produced. The first just takes all the variables as known (explicit method) on the right hand side of Equations (1), (3), and (4); updates the shaft speed by replacing dn_p/dt by $(n_p^{new} - n_p^{prev})/\Delta t$ in Equation (3); and obtains ΔP_{RP} in Equation (2) by substituting r_p^{new}. The second method is an implicit approach because it assumes that n_p is also an unknown on the right hand side of Equations (1), (3), and (4). Again, a Newton-Raphson algorithm solves the implicit approach. After comparing the two methods for a Peach Bottom transient as provided by RELAP-3B the explicit approach is recommended. The solutions of both methods are about the same and the implicit method is twice as slow because of the greater computer logic. Both methods have been put into RAMONA-III, however, with the user having a choice.

The jet pump equations detailed in the previous quarterly have been coded into the original BNL version of RAMONA-III. The combined jet pump, recirculation pump model was first tested using preliminary BNL generated Peach Bottom-2 plant model data. Since this data gave unrealistically large mass flows without the jet pump model present, a realistic mass flow of 1.28×10^4 kg/s was artificially imposed for steady state checkout purposes. The four loss coefficients required in the jet pump model were obtained from RELAP-3B results for Peach Bottom Test 3, Lu (1979b). These conditions resulted in an M ratio of 2.04, a drive pump head of 15.4 bar and a jet pump head of 2.04 bar. These values show reasonable agreement with actual steady state conditions.

In order to check out the model without imposing a mass flow, the combined jet pump, recirculation pump model was inserted into an updated BNL version of RAMONA-III, which included the Scandpower (ScP) Peach Bottom updates and data received in July. Using the loss coefficients generated from RELAP-3B data a converged steady state was obtained.

A transient calculation has been attempted using the ScP Peach Bottom model. This includes dome pressure and feedwater disturbances. The jet pump disturbance is automatically eliminated by the insertion of the jet pump model.

Several problems were encountered in running the transient such as RAMONA's use of a zero time step for transient initialization and storage of previous time values of the dependent variables in the pump differential equations for use when either the neutronic or hydraulic time step controls require a time step cut back.

The ScP Peach Bottom Test No. 3 transient is presently running and the results are being analyzed for correctness with regard to the time cut back problems.

2.1.2 Steamline Model

A steamline dynamics model is required for RAMONA-III to predict steam mass flow rate and enthalpy flow rate at the exit of a BWR steam dome during the transient induced by the sudden closure of the turbine stop valves or the main steam isolation valves. Such valve closures initiate acoustic pressure and steam velocity oscillations and they may trigger the response of safety and relief valves. The turbine stop valve closure causes the bypass valves to open.

The BNL steamline code described earlier (D.J. Diamond, et al. 1979) has now been linked with, and executed in, the RAMONA-III code.

The algorithm used in the BNL steamline code for the integration of the governing partial differential equations has been verified by comparing the computer solution for a selected test case with the corresponding analytical solution. The results are shown in Figures 1 and 2.

The BNL steamline model has been assessed by comparing computer solutions with experimental data from the Peach Bottom-2 Turbine Trip Tests (Carmichael

and Niemi, 1978). The results are shown in Figures 3 through 5 for Turbine Trip Test No. 1.

Presented below is a brief description of the BNL steamline model in its latest version, of the solution method used, of the code assessment and of work remaining for the completion of the steamline model and code developments.

Model Description

The steam line system as modeled consists of a single pipe with specified length and diameter (which may change at branch positions), connecting the steam dome with the turbine valve and having two branches at freely specified axial positions. One branch leads to the pressure relief and safety valves, the other branch leads into the bypass line and to the bypass valve. Thus, the steam line system terminates at the steam dome exit, at the turbine valve, at the relief and safety valve and at the bypass valve.

More than one steamline in parallel are modeled by a single line with its length equal to the arithmetic mean length of the parallel lines and with its internal diameter equal to the actual diameter of an individual pipe. The mass and enthalpy flow rates at the steam dome exit are then multiplied by the number of parallel steam lines.

A Main Steam Isolation Valve (MSIV) closure is modeled with a steamline segment leading from the reactor vessel to the isolation valve, including the safety and relief valves but without the line sections downstream of the isolation valve.

The effect of valve actions are modeled by imposing time-dependent mass flow rates as boundary conditions.

The modeling assumptions are:

(i)   The cross-sectional area of the pipe is uniform over axial distance between branch points.

(ii) $|\rho g_z| << |\partial p/\partial z|$, gravity effects are negligible in the momentum and energy balances. Here, ρ, g_z and p designate, respectively, the steam density, the gravitational acceleration and the steam pressure, z is the axial coordinate.

(iii) $|\partial w/\partial z| = 0$ $\{1/c |\partial w/\partial \tau|\} = 0$, local acceleration is negligible (J.S. Ansari and R. Oldenburger (1967)). The symbols w and c designate the axial velocity component and the sonic velocity, respectively.

(iv) $q''_w = 0$, the flow is adiabatic; q''_w is the wall heat flux.

(v)   The initial entropy of the steam in the pipe is uniform, the entropy of the steam entering the pipe at the steam dome is constant; this implies that viscous dissipation and axial conduction are neglible in the energy balance.

(vi)   Internal form losses are distributed in axial direction, over pipe sections adjacent to the form loss source location.

(vii)   The steam satisfies the thermal and caloric equations of state for an ideal gas.

$$\rho = \frac{\kappa}{\kappa - 1}\, p/h,$$

where $\kappa = c_p/c_v$ is the constant isentropic expansion coefficient evaluated at initial conditions of the steam in the dome, and h is the steam enthalpy.

(viii)   Pressure p, density ρ and enthalpy h are uniform over any cross-sectional area A.

These assumptions reduce the general field equations of one-dimensional pipe flow (p. 29, D.J. Diamond et al.) to these three equations of

mass conservation

$$\frac{\partial p}{\partial \tau} = -\frac{\kappa p_o}{A \rho_o} \left[\frac{p}{p_o} \right]^{\frac{\kappa-1}{\kappa}} \frac{\partial W}{\partial z}, \tag{5}$$

motion

$$\frac{\partial W}{\partial \tau} = -A \frac{\partial p}{\partial z} - \frac{f + Kd/L}{2dA\rho_o} \left[\frac{p_o}{p} \right]^{1/\kappa} |W|W, \text{ and} \tag{6}$$

thermodynamic path

$$\rho(\tau, z) = \rho(0,0) \left[\frac{p(\tau, z)}{p(0,0)} \right]^{1/\kappa}. \tag{7}$$

Equation 7 follows from Assumptions (iv), (v), and (vii) and from the energy balance. The symbols W, f, K, d, and L designate mass flow rate, Darcy friction factor, form loss coefficient, internal pipe diameter, and pipe length, respectively. The subscript o indicates initial pipe entrance conditions, $\rho_o = \rho(p_o)$, $p_o = p(0,0)$.

Pipe branches are modeled with global balances for the steam volume V in the branch section. The mass balance is

$$\dot{\bar{p}} = -\frac{\kappa p_o}{V \rho_o} \left[\frac{p}{p_o} \right]^{\frac{\kappa-1}{\kappa}} \sum_j W_{j,out} \tag{8}$$

where $\bar{p}$ is the mean pressure in the branch section and the superscripted dot designates a time derivative. Notice that mass flows W_j toward the branch are counted negatively in the sum on the right-hand side of Equation 11. The mean pressure $\bar{p}$ is taken to occur at the intersection of pipe axes in the branch section, and Equation 6 is integrated from this intersection, across the terminal cross-sections of the branch and up to the first nodes of the pipe sections feeding into the branch.

Equations 5, 6, and 8 govern the two principal variables p and W and are subject to the following initial boundary conditions. The initial conditions are, for $\tau \leq 0$

$$W(o,z) = W_o \tag{9}$$

$$0 = -A \frac{dp}{dz} - \frac{f + Kd/L}{2dA\rho_o} \left[\frac{p_o}{p}\right]^{1/\kappa} |W|W. \tag{10}$$

These are obtained by setting the time-derivatives in Equations 5, 6, and 8 equal to zero. The boundary conditions are: at z = 0, the steam dome exit

$$p(\tau,0) = P(\tau) - \frac{1+K_c}{4\rho A^2} |W|\left[W + |W|\right], \tag{11}$$

at the Turbine Stop Valve (TSV)

$$W_{TSV} = W(\tau), \quad \text{prescibed}, \tag{12a}$$

and at the bypass and check valves

$$W_B = W_b (\tau, \tau_d, \Delta p, p, \dot{p}), \quad \text{prescribed}. \tag{12b}$$

Here $P(\tau)$ is the steam dome pressure as computed by RAMONA-III or known from experiments. The symbol K_c is the entrance loss coefficient (contraction). In Equation 12b, the symbols τ_d, Δp and p stand for the known time delay of valve action, the pressure drop across the valve, the pressure just upstream of the valve and the rate of change of this pressure, respectively. The functionals in Equations 12a and b are prescribed by the user. Detailed descriptions of constitutive relations and of correlations will be published later.

Solution Technique

RAMONA-III employs explicit, first-order Euler integration in time. The BNL steamline code employs explicit, fourth-order Runge-Kutta integration in time, with an internal time-step control, governed by a user-chosen upper bound of the permissible integration error per time step for each variable.

Within RAMONA-III, the BNL steam line code advances with its own integration algorithm starting from the previous time level and terminating at the current time level. This step is carried out with a fixed value for the steam dome pressure, as supplied from RAMONA-III, and with prescribed, time-dependent valve actions. The computed flow rates of mass and enthalpy, corresponding to the current time level, are then used in RAMONA-III to advance the systems calculations to the next future time level. For optional uses, the BNL steamline code produces also the time-mean values of mass and enthalpy flows, averaged over the individual time step. The BNL steamline code is synchronized with the RAMONA-III integration step control.

In its stand-along computing mode, the BNL steamline model computes the steamline transient for a given steam dome pressure history and for specified valve actions, lists pressure and mass flow rates at selected nodal positions and at selected points in time, and stores on magnetic tape selected flow parameters and corresponding times for plotting.

For the purpose of integration, Equations 5 and 6 are discretized with respect to the spatial coordinate z on a staggered mesh.

For the initial steady state, the W-values are set equal to the initial steam mass flow rate W_o for all main steam line positions, and equal to zero for all side line positions. This satisfies Equation 9. Equation 10 is replaced by its discretized form, with its left-hand side set equal to zero. The resulting equation is solved for the initial pressures p by Newton-Raphson iteration.

Code Assessment

Results obtained from the BNL steamline code in its stand-alone version have been compared with computer calculations of the ODYN Code by GE (1978), with an analytical solution and with experimental results from the Peach Bottom-2 Turbine Trip Test No. 1 (Carmichael and Niemi 1978).

The steamline model in the ODYN Code implies the same assumptions as the BNL steamline model. The test conditions for comparing computed results from the ODYN Code and the BNL code were selected by GE to be as follows:

Geometry

Pipe length	216.5 ft	=	65.99 m
Internal cross-sectional area:	1.66 ft^2	=	0.1542m^2

Horizontal, straight pipe without bypass branch, safety and
  relief valves.

Initial Steady-State Conditions

Mass flow rate	591.5 lbm/sec =		268.3 kg s^{-1}
Inlet pressure, inside of pipe, at axial position z = 0	998 psia	=	68.8 bar
Exit pressure, upstream of Turbine Stop Valve, at axial position z = 65.99 m	945 psia	=	65.2 bar
Isentropic expansion coefficient	κ	=	1.255

Boundary Conditions

Constant inlet pressure, $p(\tau,0)$ = 998 psia = 68.8 bar
Exit mass flow rate decreasing linearly with time from initial
  flow rate to zero within 0.1 seconds.

$$W(\tau,L) = W(0,L)[1-(10s^{-1})\tau] \quad \text{for } 0 \leq \tau \leq 0.1 \text{ s}$$
$$= 0 \qquad\qquad\qquad \tau \geq 0.1 \text{ s.}$$

The results from the ODYN Code were found in Figure 19-26 on Page Q-19-4 in Appendix B of the GE Licensing Topical Report (1978). The figure is reproduced here as Figure 6. The so-called "Moody" reference curve of Figure 6 is used for the comparison between ODYN and BNL code results in Figure 7.

Even though the ODYN and BNL steamline models imply the same assumptions, the comparison of the results from the two codes in Figure 7 show good agreement only for the phase of the pressure oscillations in the steamline just upstream of the turbine stop valve, but a discrepancy of 35 psi (21%) for the pressure amplitude at the first peak following turbine stop valve closure.

In order to determine which one of the two codes compute the correct pressure amplitude and for the purpose of computer code verification, Equations 5 and 6 were solved analytically for the conditions of the above test case and with the following two simplifications:

$$\text{(i)} \qquad \kappa = 1, \tag{13}$$

$$\text{(ii)} \ \frac{f + Kd/L}{2dA\rho_o} |W| \ \equiv \beta = \text{const.} \tag{14}$$

Equation 14 represents laminar flow without form losses ($K=0$). For laminar flow, $f = 64/N_{Re}$ and $\beta = 32 \, \mu_o/(\rho_o d^2)$. In order to satisfy Equation 10 for the initial pressure distribution, we set

$$\beta = \left[p(0,0) - p(o,L) \right] A/(W_o L). \tag{15}$$

Details of the analytical solution will be presented in a topical report later. The final result for the pressure rise above the dome pressure, $\tilde{p}(\tau,L) \equiv p(\tau,L) - p_o$, at the Turbine Stop Valve is

$$\tilde{p}(\tau,L) = G(\tau) + H(a,\tau) + M(\tau) + N(a,\tau) - \rho_o w_o \beta L \tag{16}$$

where

$$G(\tau) \equiv \left(\frac{W_o}{A} c \right) (a\tau) e^{-\beta\tau/2} \left\{ \left(1 + \frac{2\beta\tau}{3} \right) \left[I_o(\beta\tau/2) + I_1(\beta\tau/2) \right] - \frac{2}{3} I_1(\beta\tau/2) \right\} \tag{17}$$

$$H(\tau,a) \equiv G(\tau-1/a) \qquad \text{for } (a\tau) \geq 1$$
$$\equiv 0 \qquad \qquad \text{for } 0 \leq (a\tau) \leq 1 \tag{18}$$

$$M(\tau) \equiv \sum_{n=1}^{\infty} \left[\phi_n + \int_{\frac{2nL}{c}}^{\tau} \phi_n(\zeta)d\zeta \right] \qquad \text{for } c\tau \geq 2nL \tag{19}$$

$$\equiv 0 \qquad \qquad \text{for } c\tau < 2nL$$

$$N(\tau) \equiv \sum_{n=1}^{\infty} \psi_n + \int_{\frac{2nL}{c}}^{\tau} \psi_n(\zeta) d\zeta \qquad (20)$$

$$\psi_n(\tau) \equiv \phi_n(\tau - 1/a) \qquad \text{for} \quad (a\tau) \geq 1 + 2anL/c$$

$$\equiv 0 \qquad \text{for} \quad (a\tau) \leq 1 + 2anL/c \qquad (21)$$

$$\phi_n \equiv (-1)^n \frac{2W_o}{A} ca \int_{\frac{2nL}{c}}^{\tau} e^{-\frac{\beta\zeta}{2}} I_o \left[\frac{\beta}{2} \sqrt{\zeta^2 - (2nL/c)^2} \right] d\zeta$$

$$\qquad (22)$$

$$\text{for} \quad \tau c \geq 2nL$$
$$\equiv 0 \qquad \text{for} \quad 0 \leq \tau c \leq 2nL$$

I_o and I are the modified Bessel functions of the first kind and of zero and first orders, respectively.

Observe that the series of Equations (15) and (16) are zero for $\tau c < 2L$, that is, until the first expansion wave returns to the Turbine Stop Valve. Notice also, that each reflection of an expansion wave at the Turbine Stop Valve introduces a new term in the series of Equations (15) and (16), and also that for any finite time, these series have only a finite number of nonzero terms.

The quadratures in Equations 19 and 20 were executed by Runge-Kutta integration with a time-step control to guarantee four significant digits in the result.

Figure 1 shows the comparison of the results from the BNL steamline code (circles) and from Equation 12 (solid line). Shown is the pressure rise $p(\tau,L) - p(o,L)$ versus time τ. The code was executed with the imposition of laminar flow at all flow speeds. The chosen test conditions are:

rate of valve closure	a	=	10.0	s^{-1}
sound speed	c	=	438.5	$m\ s^{-1}$
pipe cross-sectional area	A	=	0.15422	m^2
pipe length	L	=	65.985	m
initial mass flow rate	W	=	268.3	$kg\ s^{-1}$
friction parameter	β	=	3.18257	s^{-1}
initial density	ρ_o	=	35.783	$kg\ m^{-3}$
number of equally spaced nodes			80.	

It can be seen from Figure 1 that the BNL steamline code computes the pressure amplitude correctly in accordance with the governing equations, Equations 1 and 2 when the conditions in Equations 9 and 10 are imposed. Since

the general solution algorithm was left unaltered by Equations 9 and 10 it is claimed that the BNL steamline code computes the pressure amplitude and phase correctly and that the pressure amplitude as computed by ODYN and shown in Figure 7 is too low.

Figure 2 exhibits the influenc/ f wall shear and, consequently, initial pressure drop on the pressure excursion at the Turbine Stop Valve. For inviscid flow $\beta = 0$ and Equation 16 reduces to

$$\tilde{p}\ (\tau,L)\ =\ \frac{W_o c_o}{A}\ a\ \left[\ S\left(\frac{2L}{c_o},\ \tau\ \right)\ -\ S\left(\frac{2L}{c_o},\ \tau - \frac{1}{a}\right)\right] \tag{23}$$

where

$$S\left(\frac{2L}{c_o},\tau\right)\ \equiv\ \tau\ -\ 4\ nL/c_o \quad \text{for} \quad 4n \leq \frac{\tau c_o}{L} \leq 2(2n+1),$$

$$\equiv\ 4(n+1)L/c_o - \tau \quad \text{for} \quad 2(2n+1) \leq \frac{\tau c_o}{L} \leq 4(n+1),$$

$$\equiv\ 0 \quad \text{for} \quad \tau \leq 0,$$

The lower, solid line curve in Figure 2 represents Equation 23, whereas the circles depict the finite-difference solution from the BNL steamline code. The upper, dash-dotted curve in Figure 2 represents the finite-difference solution for frictional flow according to Equations 2 and 6, with $f = 0$ and $k\Delta L/d = 0.104$. Both curves were computed with $\kappa = 1$ and 80 nodes. The solid curve has the amplitude of $c_o W_o/A$.

Figure 2 shows good agreement for inviscid flow calculations between analytical and finite-difference solutions. The upper curve in Figue 2 reveals that the initial pressure drop due to friction in the pipe causes the pressure rise at the time of valve closure to exceed $c_o W_o/A$ and to continue after the time of valve closure until the expansion wave arrives at the valve.

Computed results from the BNL steamline code have been compared with experimental results from the Peach Bottom Turbine Trip Test No. 1 (Carmichael and Niemi, 1978). The purpose of this comparison is to assess the model assumptions, particularly Assumption (vii).

The assessment consists of imposing the measured steam dome pressure as inlet boundary condition, the measured valve stem actions at the turbine stop valve and at the bypass valve as exit boundary conditions, and then of comparing the two measured pressure histories for the Main Steam Isolation Valve pressure and for the Turbine Stop Valve pressure with computed pressure histories. The valve stem actions have been imposed approximately by prescribed linear functions of mass flow rate versus time.

The test data were taken from Tables 3-5, 6-1, 6-2, B-1, B-6, B-7, B-8, and from Figure 6-1 of Carmichael and Niemi (1978). The recorded traces in Figure 6-1 were digitized, using an enlarged reproduction of Figure 6-1. The digitized experimental data and the computed data were machine-plotted. The

results are shown in Figures 3 through 5 and in Figures 8 and 9. Both curves in Figure 3 are plotted from 75 data pairs (p, τ). The experimentally obtained curves for turbine stop valve pressure and main steam isolation valve pressure are drawn from 125 and 80 data points, respectively. The curves of computed pressure transients at the turbine stop valve and at the main steam isolation valve, shown in Figures 4, 5, 8, and 9 are drawn from approximately 1,400 computed data pairs.

The origin of the time axis (abscissa) in Figures 3, 4, 5, 8, and 9 is translated by 224 milliseconds in positive direction relative to the time origin in Figure 6-1 of Carmichael and Niemi such that the Turbine Stop Valve starts to close at time $\tau = 0$. This translation accounts for 80 milliseconds of delay in the mass flow response to valve action, 30 milliseconds of signal delay in the pressure sensor connecting line and 91 milliseconds of a time shift in Figure 6-1 of Carmichael and Niemi (1978). The remaining 23 milliseconds cannot be accounted for, except for a portion of this amount which can be justified by the possibility (p. B-4, EPRI-NP-564) that the time delay in the sensor lines should be greater than 30 milliseconds. The total translation by 224 milliseconds is justified by the fact that the turbine stop valve pressure sensor is just upstream of the valve and that the pressure must start to rise, when the mass flow rate commenses to decrease.

Geometric data were daken from the EPRI report by Larsen (1978), line A was modeled. The initial mass flow rate was computed from a mass balance for the core bypass junction, an energy balance for the core and an energy balance for the reactor:

$$4W_o = \frac{W_c \left[h_{c,i} - h_f \right] + Q}{h_e - h_f} \tag{24}$$

Here W_c, $h_{c,i}$, h_e, h_f, and Q designate, respectively core mass flow rate, core inlet enthalpy, steam dome enthalpy, saturation liquid enthalpy, and thermal power release in the core, respectively.

The BNL steamline code was executed for the conditions and with the parameters as listed below:

Peach Bottom-2, Turbine Trip Test No. 1

Initial mean core pressure		69.29 bar
Initial core power (47.4% of 3,295 MWT)		1,562 MWt
Initial core mass flow rate		12,763 kg/s
Total initial steam mass flow rate through four steam lines	$4W_o =$	762.80 kg/s
Initial steam mass flow rate through Line A,	$W_o =$	190.70 kg/s
Initial steam dome pressure,	$p_o =$	68.35 bar
Transient steam dome pressure (curve fit)		Eq. 25
Turbine stop valve closure rate (see Equation 26)	$a =$	10.53 1/s

Maximum bypass valve capacity $W_{b,max}$ = 110.54 kg/s

Bypass valve action delay τ_d = 0.30 s

Bypass valve opening time
(see Equation 47) τ_b = 0.588 s

Pipe length between steam dome and

pressure sensor at main steam isolation valve 27.80 m

inboard main steam isolation valve 39.00 m

branch to bypass line 125.26 m

turbine stop valve and its pressure
sensor 131.21 m

Cross-sectional area of main steam line 0.2713 m^2

Length of bypass line 20.59 m

Cross-sectional area of bypass line 0.07015 m^2

Number of parallel steam lines 4

Number of nodes between steam dome and

branch to bypass 65

Turbine stop valve 67

Number of nodes in bypass line 10

Entrance loss coefficient 0.5

Elbow loss coefficient (9 elbows) 0.9

Loss coefficient for both MSIV 1.14

The boundary conditions for Turbine Trip Test No. 1 were as follows:
(i) the steam dome pressure, a curve fit to the experimental data and
shown as the dashed curve in Figure 3,

$$P(\tau) = p_1 + 9.08 \times 10^4 \frac{N}{m^2} e^{-0.783s^{-1}(\tau-0.317s)} \sin\left[\chi(\tau-0.317s)\right],$$

(25)

where

$$p_1 = \sum_{j=0}^{4} b_j (\tau-0.317s)^j$$

$$\chi_o = \left[2.078 + 1.550s^{-1}(\tau-0.317s)\right]s^{-1}$$

$$\chi = \chi_o \qquad \text{for } \tau < 0.717 \text{ s}$$

$$\chi_o + 0.5(\tau-0.317s) \ s^{-1}. \left[\exp \ -25^{-1} \ (\tau-0.317s)\right]$$

and $b_o = 0$ $b_2 = -0.44128s^{-2}$ $b_4 = 0.00754667s^{-4}$

$b_1 = 1.03172s^{-1}$ $b_3 = 0.09165s^{-3}$

(ii) the steam mass flow rate at the Turbine Stop Valve

$$W_{TSV} = W_o [1-a\tau] \text{ for } 0 \le a\tau \le 1$$

$$= 0 \qquad \text{for } a\tau > 1,$$

(26)

where $W_o = 190.70$ kg/s and $a = 10.53s^{-1}$.

(iii) the steam mass flow rate at the bypass valve

$$
\begin{aligned}
W_b &= 0 & \text{for} \quad 0 \leq \tau \leq \tau_d \\
&= W_{b,max} \text{ Min} \left\{ 1, \frac{\tau - \tau_d}{\tau_b} \right\} & \text{for} \quad \tau > \tau_d,
\end{aligned} \tag{27}
$$

where $W_{b,max} = 110.54$ kg/s,

Figures 4 and 5 show the comparison of computer calculation with experimental data, namely the pressure rises at the Turbine Stop Valve and at the Main Steam Isolation Valve, respectively. The experimental curves show the high-frequency pressure oscillations caused by wave reflections in the pressure sensor connections. These high-frequency oscillations are not modeled. The computed curves agree fairly well with the measured mean pressure fluctuations of low frequency. The computed propagation velocity (Figure 4) is approximately 4% higher than the measured velocity, and the damping is approximately 30% too low. Figure 5 leads to the same conclusions.

As can be seen from the analytical solution in Figure 2, friction and form losses increase the damping and reduce the propagation velocity. Therefore, the turbine trip transient calculation was repeated with all loss coefficients set equal to twice their best-estimate values. The results are shown in Figure 8 and reveal a strong effect of loss coefficients on damping but no noticeable effect on wave propagation velocity.

The wave velocity can be reduced by decreasing the polytropic expansion coefficient from its best-estimate value of $\kappa = 1.277$ (from steam properties) to the value of $\kappa = 1.05$. This is shown in Figure 9. Notice, however, that the pressure rise at the time of valve closure and the time of the first expansion wave reflection is too low for the corrected propagation velocity.

It appears that the small discrepancies between measured and computed pressure responses in the steamline to a turbine trip cannot be resolved without further detailed analysis of the instrumentation, specifically of steam line geometry, sensor connection delays and signal processing. The modeling assumptions appear to be justified.

Future Work on Steamline Model

Peach Bottom-2 Turbine Trip Tests No. 2 and 3 will be used to complete the code assessment.

Programming on RAMONA-III will continue to implement plant controls and output editing.

2.1.3   Control and Protection System

The following plant protection trips have been added to RAMONA-III in the form of updates.

A.   Scram

ID	Conditions
1.	Time
2.	High Power
3.	Low Reactor Vessel Water Level
4.	High Reactor Vessel Water Level
5.	High System Pressure

B.   Recirculation Pump Trip
1.   Time
2.   High System Pressure
3.   Low Vessel Water Level

C.   Feedwater System Trip
1.   Time
2.   High Vessel Water Level

In addition, the following are in the process of being added:

D.   Turbine Trip
1.   Time
2.   Low Vessel Water Level
3.   High Vessel Water Level
4.   Low Turbine Inlet Pressure

E.   Turbine Bypass Opening
1.   Time
2.   Turbine Inlet Valve Closure

A.   Scram
6.   Turbine Inlet Valve Closure
7.   Main Steam Isolation Valve Closure

B.   Recirculation Pump Trip
4.   Turbine Inlet Valve Closure

Each trip has its own set point and its own delay time.

The data necessary for these trips can now be read in via standard RAMONA input cards. The code prints out the trip input for all the specified trips, and in the case of a Feedwater System Trip it requires a table of flow rates versus timed after start of trip.

2.1.4.   Fuel Rod Model

The fuel rod heat conduction model has been modified to take into account cladding heat capacity and non-uniform heat generation in the pellet. The

model which was actually implemented in RAMONA-III differs slightly from that which was described in the previous Quarterly Progress Report (see Elias (1979)). It has been successfully used in transient calculations but at present is limited in the number of fuel rod meshed that can be used.

The following assumptions form the basis for the model:

1. All fuel rods within one node are assumed to behave in the same way.

2. Axial heat conduction is neglected.

3. Nuclear heat generation is a parabolic function of pellet radius with magnitude a function of time. There is no azimuthal dependence in the pellet and no heat generation in the cladding.

4. The gap is thin and has no heat capacity.

5. Densities of fuel and cladding are constant. The fuel and cladding thermal conductivities depend on the local temperature. The heat capacities of the fuel and cladding depend on average fuel and cladding temperatures, respectively.

6. The gap heat transfer coefficient is a (given) function of the average fuel and gap temperature.

7. All pellet zones are of equal area as are all clad zones.

8. The zone average temperature is assumed to be the zone midpoint temperature. The temperature on the boundary between two zones is given by a linear interpolation between the temperatures at the centers of the two zones.

These assumption are used to solve the problem along with the clad outer surface temperature as a given boundary condition and internal boundary conditions describing the heat transport across the gap. The latter are defined using a gap heat transfer coefficient.

Subroutines have been added to the code to calculate the fuel and cladding thermal conductivity and heat capacity as a function of temperature. The properties were obtained from MacDonald (1976).

2.2 Plant Modelling

A plant model consisting of input data to RAMONA-III for Peach Bottom-2 was prepared. The reactor conditions were those prior to the running of Turbine Trip Test No. 3. A similar plant model was received from Scandpower Inc.

The differences between the two input decks has been studied in an effort to determine which representation might be superior. Some of the differences between the input models are the following: the cross-section parameterization used in the BNL input is different (see previous Quarterly Progress Report)

and the neutronic data itself was generated independently at BNL and ScP. The ScP riser volume represents the reactor upper plenum only; the separators, standpipes, and surrounding fluid are all represented by the steam dome volume. Our preference is to put the separator into the riser volume with the surrounding water included as part of the downcomer. The ScP bypass flow area does not include the reflector region. In order to get the correct bypass flow fraction they vary the pressure loss coefficient. The hydraulic conditions in the bypass region do not provide feedback for the core power calculation. Nevertheless, it seems preferable to use the correct flow area and then adjust the loss coefficients to get the right bypass flow. These differences may or may not be significant. This will become clearer after more experience is gained in running the code.

2.3 Programming Considerations

2.3.1 Coding Modifications

During this period five sets of update corrections to RAMONA-III have been received from Scandpower. The updates were meant to: a) correct "bugs" that had been uncovered when their operating system was changed in the Spring; b) add the ability to run with the neutron diffusion parameter representation specific to the PRESTO code; c) modify the hydraulics model by neglecting the variation of the local rate of change in pressure; d) allow for steam dome pressure feedwater flow rate and pump head to be input as a function of time so that the Peach Bottom-2 Turbine Trip Test #3 could be run; e) correct for inconsistencies between the steady-state solution and the initial dynamics solutions and f) correct for other problems. Considerable problems were encountered in the implementation of two of these correction sets at BNL due partly to the differences between the BNL and Scandpower versions of the code and partly to incomplete information being received. With the help of ScP all of these problems have now been resolved. In addition other problems have been encountered in the development of a BNL input model for use with RAMONA-III due mainly to the use of existing options within the code which ScP does not use and which appear to be not fully debugged. Most of these problems have also now been resolved at BNL.

2.3.2 Graphics Capability

The plot and data control (PAD) program is a general purpose post processing plot program designed for use with mesh type codes (where arrays are, for example, a function of x, y, z, t) such as RAMONA. The first phase of this program is to have the data files created and interpreted. The data arrays to be plotted are stored on a data file along with descriptive information to sufficiently define the data arrays for processing by the PAD program. The format of the data file provides flexability to the extent that no programming modifications are required to process data files from different mesh programs. Overplots of two or more curves on the same axes from the same or different data files is possible.

Program control in PAD is by means of command statements that reference the arrays and coordinate variables by name. This combination of command

statements with the geometric description contained on the data file allows program PAD to be logically independent of the mesh program that produced this data file.

The third and final phase of program PAD after manipulation of the data to create different arrays (see below) is generation of PLOTS under control of the user through the command statements. Arrays to be plotted are processed as the data is recorded from tape and stored as limited lists on disk. This allows all curves (surfaces) that are plotted on the same axes to be processed by a single module that handles the type of plot (2,3, etc.) specified on the appropriate command statement. Additional plot modules may be added to the program when needed.

Significant input from the user on the command statements controls what data arrays are plotted, specifies headings and axis labels, and determines whether curves are drawn on the same or different axes.

In addition the user may further reduce this data by imposing bounds on the coordinates or by data averaging to reduce the array dimension. PAD's approach to data reduction is to allow the user to define a new array that is the result of a simple transformation of a previously defined array. Thus, the array $P(z)$ may result from the array POWER (x, y, z, t) by the transformation

$$P(z) = \sum_{x,y} \text{POWER } (x, y, z, t = 1000)$$

where x, y, z, t are the coordinate variables specified in the data file with the same names.

The program presently contains all the necessary modules except for the plot routines and is in the process of being debugged. Additional modification and extensions will undoubtedly be necessary before this program is available for general use.

2.4 RETRAN Code Implementation

The RETRAN code has been obtained at BNL and made operational on the BNL-6600. All of the test problems provided by EPRI have been run successfully and the results are in agreement with the results supplied with the code.

A plant model, representing the Three Mile Island (TMI) Unit 2 has been obtained from GPU/Energy Incorporated. The model has been used to calculate a transient similar to the TMI event and the results are currently being evaluated.

2.5 IRT Code Modification

2.5.1 IRT Once-Through Steam Generator Downcomer Modeling

The downcomer model with a momentum equation to calculate the recirculation flow through the aspirator region has been incorporated in the once-through steam generator model in the IRT code. The new model has been

used to analyze the initial phase of a transient similar to the Three Mile Is-land (TMI) incident. The transient analyzed consists of a complete loss of normal feedwater with no auxiliary feedwater. Scram is initiated by high pressurizer pressure; in addition, when the power operated pressurizer relief valve is predicted to open, the valve is assumed to stick in the full open position for the remainder of the transient. The IRT calculations are in re-latively good agreement with the TMI data for the pressurizer pressure and pressurizer level transients.

2.5.2 Steam Generator Tube Rupture Model

A model to simulate steam generator tube ruptures has been incorporated in the IRT once-through steam generator model. The model allows a specified num-ber of tubes to be ruptured manually, at a certain time or when the pressure difference between the steam generator primary and secondary sides exceeds a designated value. The rate of leak flow from the ruptured tubes is computed by both Moody's critical flow correlation and the Darcy formula; the smaller value is used in the computations. For the Moody critical flow calculation, the fluid enthalpy and pressure upstream of the ruptured tube are used to determine the leak flow per unit area. This value is then multiplied by the rupture area to give the total leak flow rate.

2.5.3 IRT Steamline Break Flow Model

The original IRT once-through steam generator model simulated the steam generator secondary system only up to the steam outlet nozzle. A new model has been added that represents the steam header and steam lines up to the tur-bine inlet valve. This model allows simulation of double-ended steamline break transients where all steam generators initially blow down through the rupture. In addition, the following systems are simulated in the new model:

1) steam dump system
2) bypass system
3) main steam isolation valve
4) turbine admission valve

2.6 Steam Generator Refill Modeling

The U-tube steam generator model in the IRT code has been modified to re-move some restrictions in the original CESEC code that prevented steam gener-ator refill after depletion of the secondary side water mass. In addition, the code has been modified to prevent secondary pressure from falling below atmospheric pressure during long term depressurization transients.

2.7 Once-Through Steam Generator Analyses

B&W has proposed several changes in the plant protection system to miti-gate the consequences of a loss of feedwater transient. These changes include an increase in the pressurizer relief valve set point and a reduction in the high pressurizer pressure scram set point. In support of these changes, B&W has submitted an analysis of the loss of normal feedwater transient with auxi-liary feedwater initiated at 40 seconds. Similar calculations have been

performed using the IRT code with the once-through steam generator model. The results of both analyses indicate that the pressurizer relief valve will not open if the set points are revised and auxiliary feedwater is delivered to the steam generator 40 seconds after initiation of the transient.

The once-through steam generator model in the IRT code has been used to analyze an overfeed transient for a typical B&W plant. The transient analyzed consisted of a turbine trip with continuation of normal feedwater and initiation of auxiliary feedwater. In addition, when the steam bypass system became operational it was assumed to malfunction and remain open. These assumnptions were made to maximize the primary system cooldown. The objective of the analysis was to determine if voids were formed in the primary system during the transients. The results indicate void formation approximately 45 seconds after initiation of the transient.

REFERENCES

CARMICHAEL, L.A. and NIEMI, R.O. Transient and Stability Tests at Peach Bottom Atomic Power Station Unit 2 and End of Cycle 2, EPRI NP-564, Topical Report (Project 1020-1), 1978.

DIAMOND, D.J. et al. Water Reactor Safety Research Division, Quarterly Progress Report, January 1-March 31, 1979 BNL-NUREG-51015, NUREG/CR-0821.

ELIAS, E. "New Heat Conduction Model in RAMONA-III." BNL internal memo (Oct. 1979).

GE Licensing Topical Report: Qualification of the One-Dimensional Core Transient Model for Boiling Water Reactors, Vol. 1. NEDO-24154, 1978.

LARSEN, N.H. "Core Design and Operating Data for Cycles 1 and 2 of Peach Bottom-2, Topical Report EPRI-NP-563, 1978.

LINFORD, R. B. "Analytical Methods of Plant Transient Evaluations for the General Electric Boiling Water Reactor," NEDO-10802, General Electric (1973).

LU, M.S., CHENG, H.S., SHIER, W.G., DIAMOND, D.J., LEVINE, M.M. "Analysis of Licensing Basis Transients for BWR/4", BNL-NUREG-26684 Brookhaven National Laboratory, (1979a).

LU, M.S., HSU, C.J., CONNELL, H.R., SHIER, W.G., LEVINE, M.M. "Thermal-Hydraulic Analysis of Peach Bottom-2 Turbine Trip Tests," BNL-NUREG-25526, Brookhaven National Laboratory (1979b).

MACDONALD, P.E. and THOMPSON, L.B. "MATPRO, A handbook of Material Properties for use in the Analysis of Light Water Reactor Fuel Rod Behavior," ANCR 1263, Idaho National Engineering Lab. (1976).
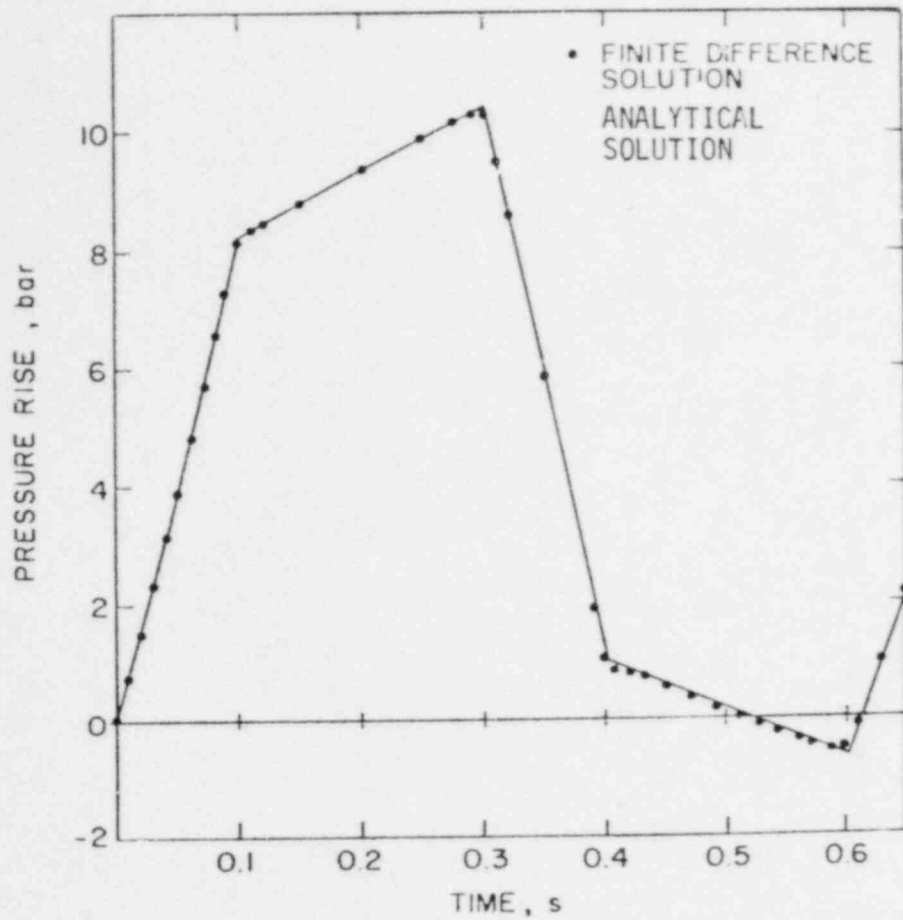
Figure 1   Comparison of analytical solution
(Eq. 16) with computer solution,
general case with friction.
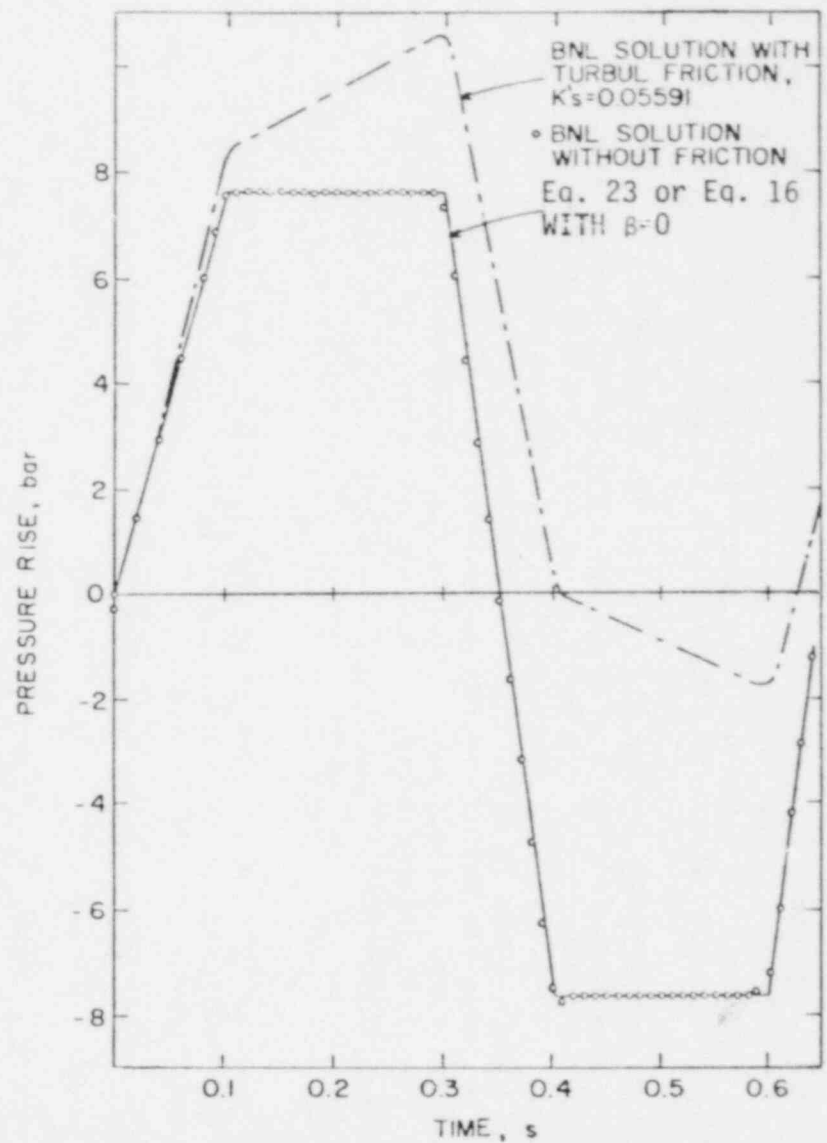BNL Neg. No. 10-1205-79.

Figure 2   Effect of friction and comparison of
computer solution with analytical
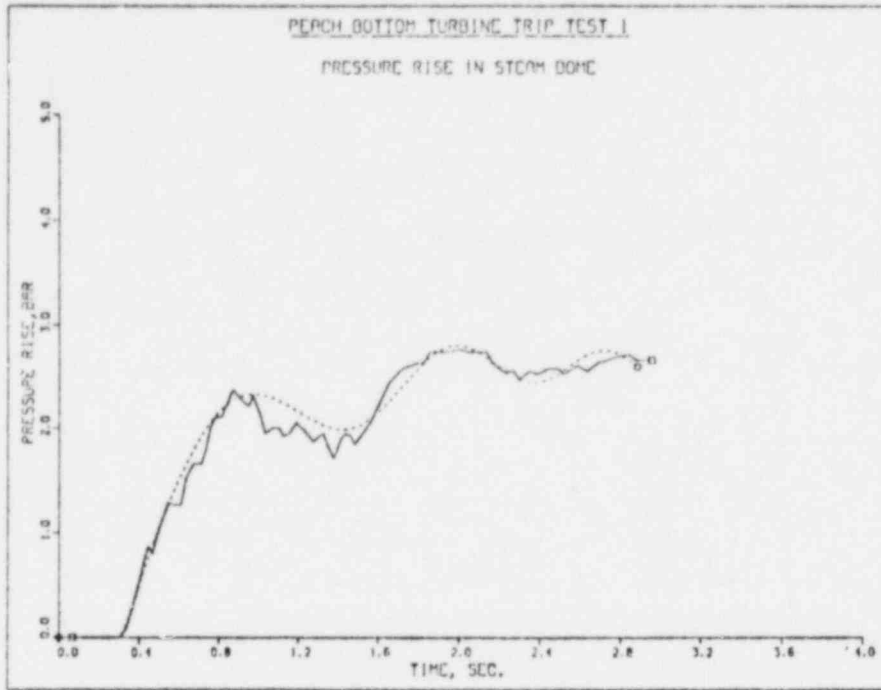solution for inviscid flow.
BNL Neg. No. 10-1208-79.

Figure 3 Steam dome pressure. Solid curve: TTI experiment dashed curve: curve fit, Eq. 25, as used for boundary condition.
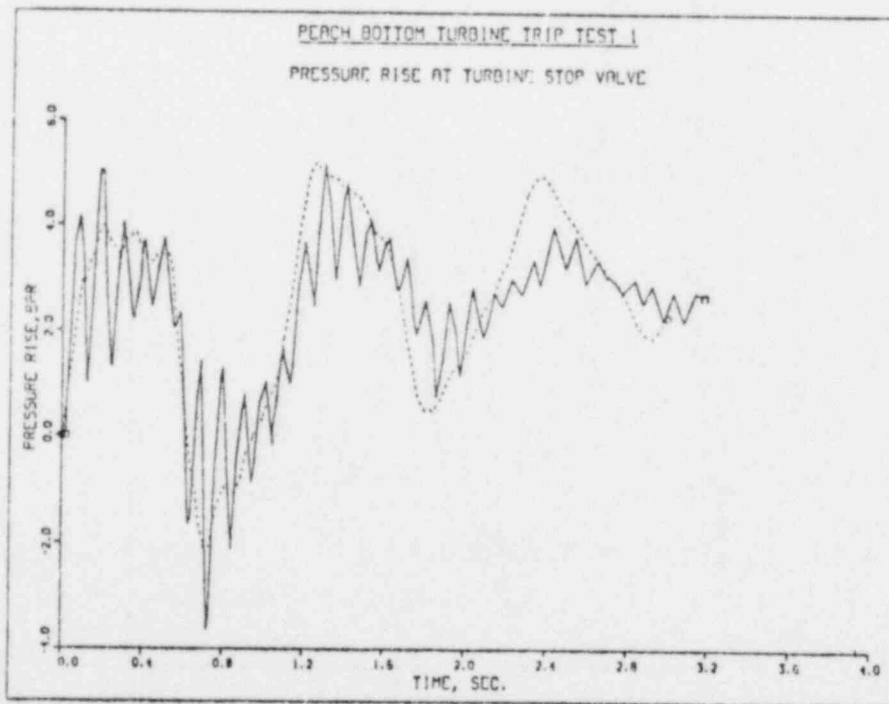

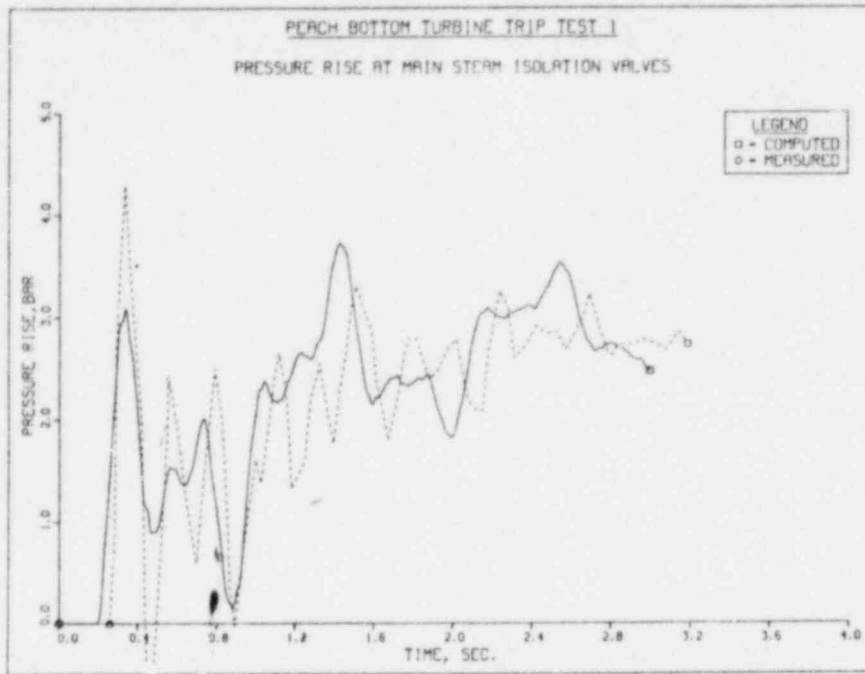Figure 4 Pressure rise at turbine stop valve. Solid curve: experiment. Dashed curve: computer solution.

Figure 5   Pressure rise at main steam isolation valve.
Dashed curve: experiments; solid curve:
computer solution.
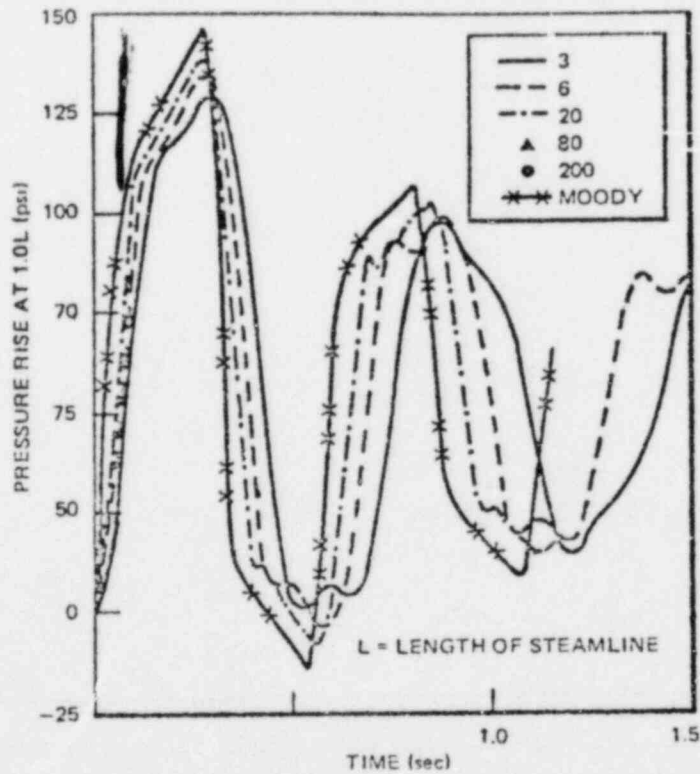
Figure 6   ODYN calculations of pressure rise at pipe
exit, effect of nodalization.
(NEDO-24154).
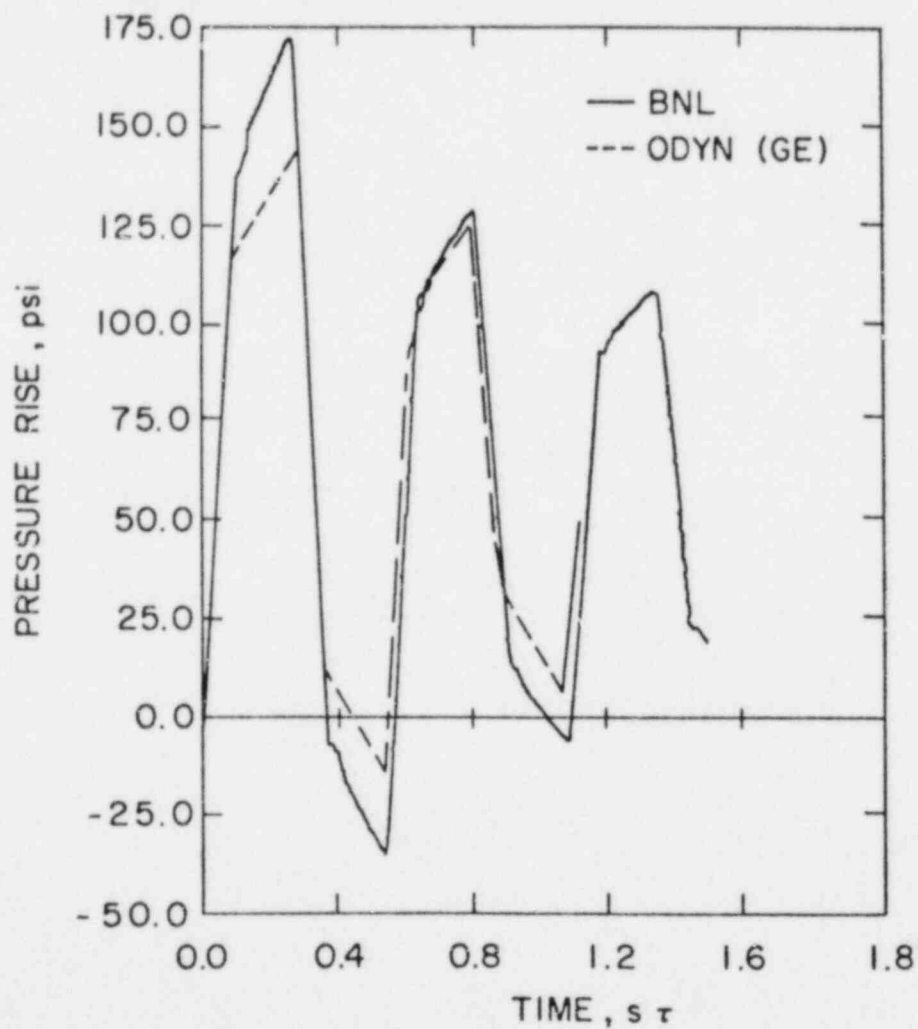
Figure 7   Comparison of results from ODYN code (GE) with
          BNL steam line code for selected test case.
          BNL Neg. No. 10-1204-79.
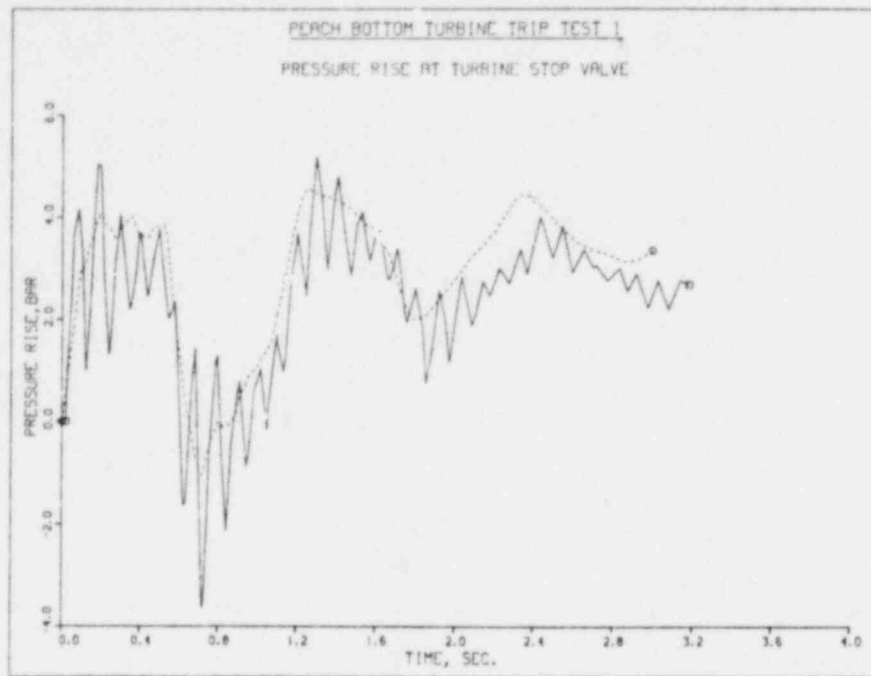
Figure 8 Effect of form losses on pressure amplitude and
wave propagation velocity. Solid curve: experiment;
dashed curve: computed result. Reference calculation
is shown in Figure 4.
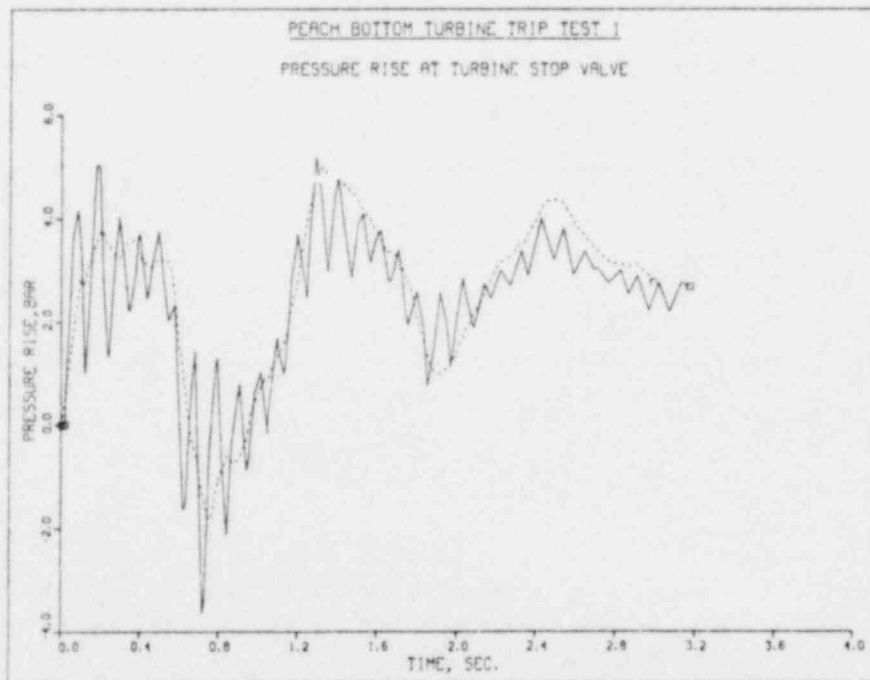
Figure 9 Effect of polytropic expansion coefficient on
pressure wave propagation velocity and amplitude.
Solid curve: experiment; dashed curve: computed
results. Reference calculation is in Figure 4.

3. TRAC Evaluation and Model Improvement

3.1 Moby-Dick Nitrogen-Water Experiments (P. Saha and Y. Feng)

As a continuation of the TRAC-P1A assessment work with the Moby-Dick nitrogen-water tests (Jeandey, 1979), further TRAC predictions have been performed to study the effects of (i) the inlet BREAK component size and (ii) finer nodalization. Results of these studies are summarized below.

It was mentioned in the previous quarterly (Saha, 1979) that the pressure just at the entrance of the test section was lower than the experimental value or the value assigned to the inlet BREAK component. This is due to the stag-gered mesh scheme employed in TRAC and the suggestion that the length of the BREAK or FILL components be the same as the neighboring cell in the a'jacent component (TRAC-P1A, 1979). In order to obtain the correct (experimental) pressure at the test section inlet, we started to reduce the length of the inlet BREAK cell. This did not pose any problem for the code, indicating that it does not seem to be mandatory to have equal lengths for the BREAK and the neighboring cells. Results with various lengths for the inlet BREAK component are shown in Figures 3.1 and 3.2 for Runs 3095 (zero quality) and 3176 (low quality), respectively. All runs had the same nodalization (42 cells). It is seen that as the size of the inlet BREAK cell decreases, the pressure at the inlet of the test section increases and eventually reaches the experimental value. Thus, a small inlet BREAK cell size of the order of 1 cm is needed to represent the inlet pressure boundary condition correctly. It is also noticed that the predicted inlet mass flow rate increases significantly as the inlet BREAK cell size is decreased. This is due to the fact that the calculated pressure drop across the straight portion (from the inlet to the throat) of the test section increases with decreasing BREAK cell size.

The nodalization study was carried out next. For the zero quality run, i.e., Run 3095, finer nodalization tends to increase the mass flow rate (Saha, 1979). For two-phase situations, the effects of finer nodalization are not appreciable, as shown in Figure 3.3, where results for three different nodal-ization are depicted for low-quality Run 3176. This trend is confirmed for the intermediate-quality Run 3087 in Figure 3.4. It is also seen from Figure 3.4 that the effect of nodalization is negligible compared to that of inlet BREAK cell size, particularly for two-phase runs.

The effects of various two-phase friction factors will be studied in the near future. Comparisons between the TRAC-P1A predictions and the experimental results which are available now, will also be shown in the next report.

3.2 Shock-Tube Test with Air (Y. Feng and P. Saha)

An idealized thought experiment has been conducted in a shock-tube filled with air to separate the numerics of TRAC-P1A from its modeling. Initially, a diaphragm divides the shock-tube into two chambers of equal volumes containing
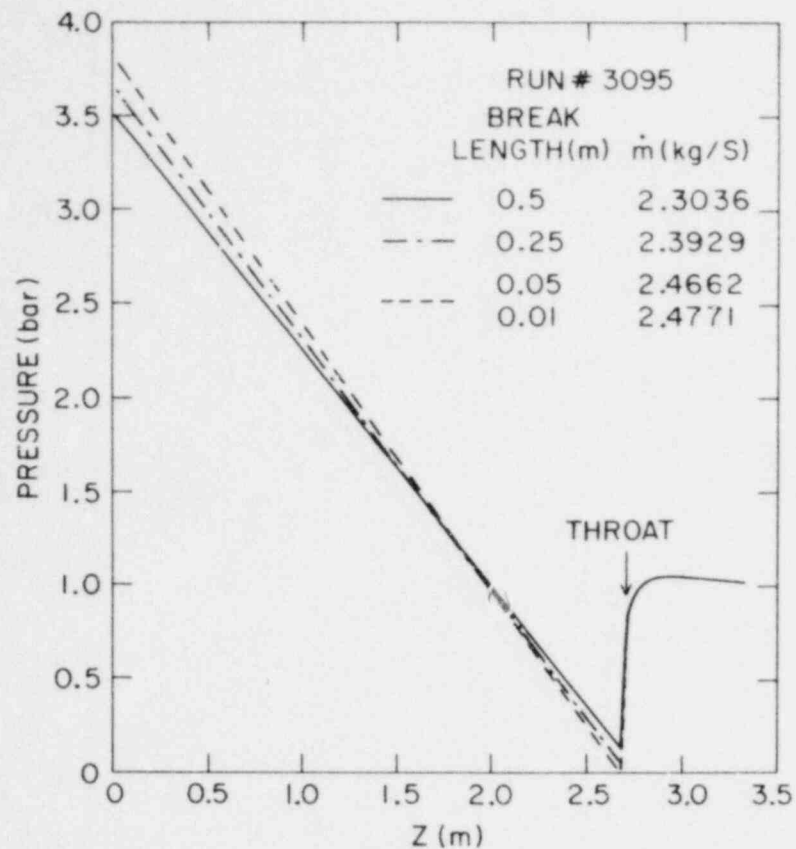
Figure 3.1 - Effect of Inlet BREAK Cell Length
on TRAC-P1A Prediction for Run 3095.
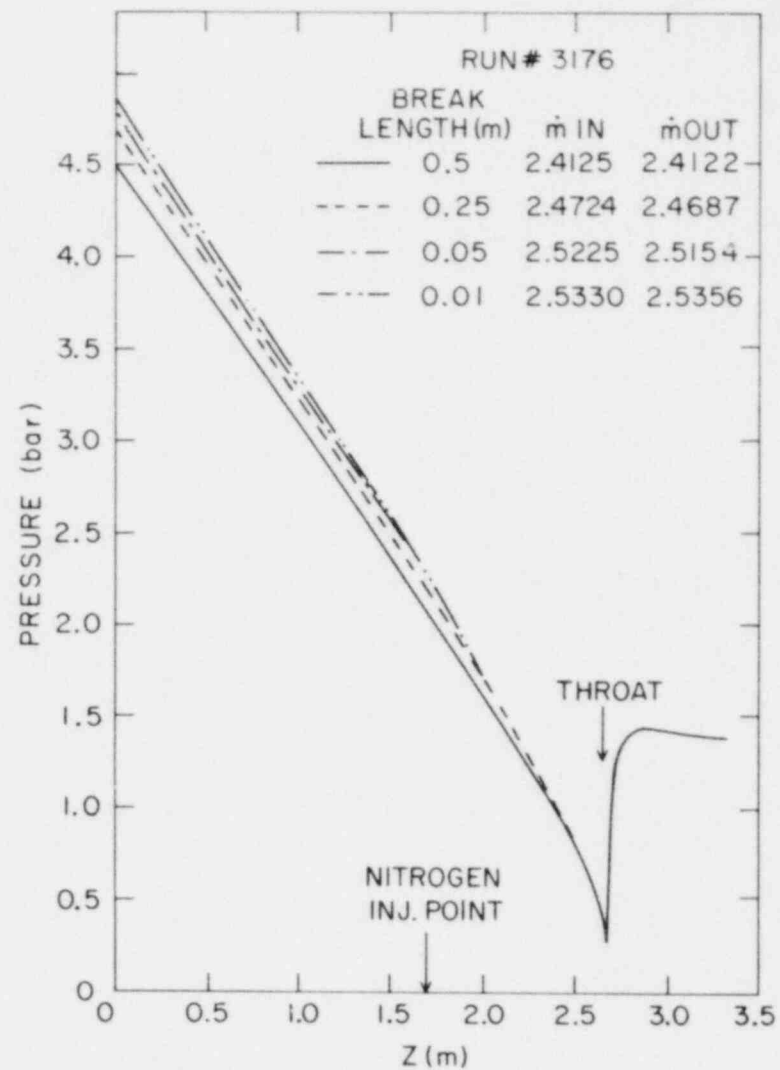(BNL Neg. No. 10-1417-79)

Figure 3.2 - Effect of Inlet BREAK Cell Length
on TRAC-P1A Prediction for Run 3176.
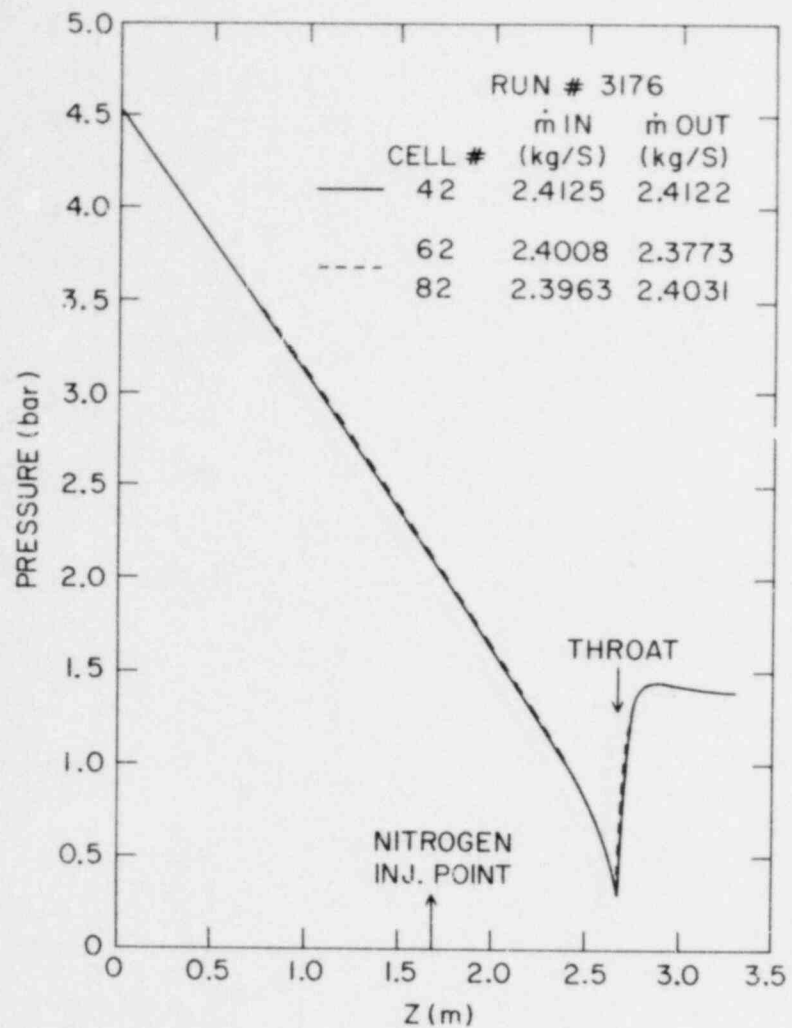(BNL Neg. No. 9-707-79)

Figure 3.3 - Effect of Nodalization on TRAC-P1A
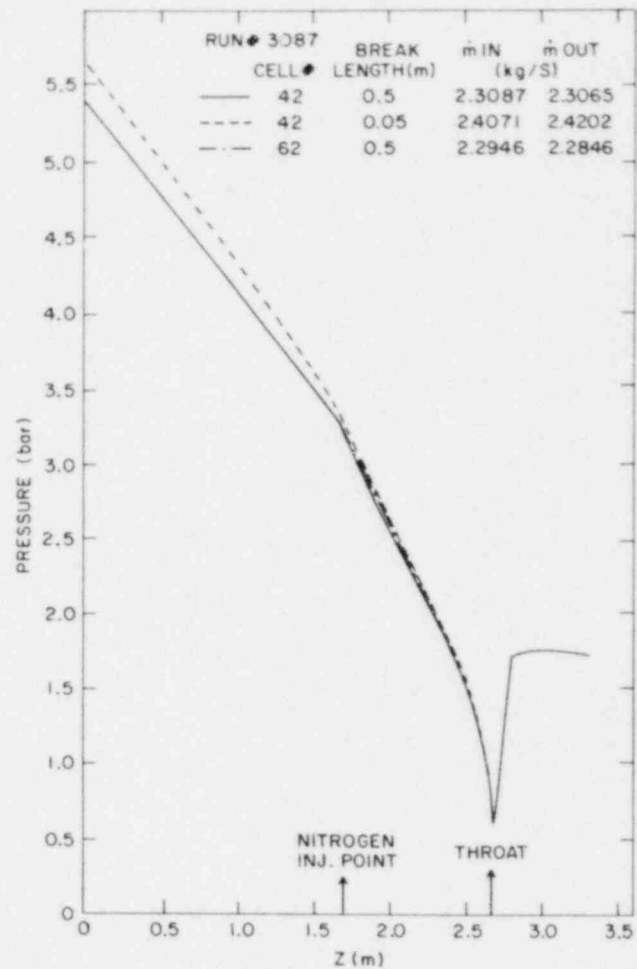Prediction for Run 3176. (BNL Neg. No. 9-704-79)

Figure 3.4 - Effect of Nodalization and Inlet
BREAK Cell Length on TRAC-P1A Prediction for
Run 3087. (BNL Neg. No. 10-1416-79)

air at different pressures. The temperatures of the air in two chambers may or
may not be the same. At time equal to zero, the diaphragm is burst and the
transient begins. As shown in Figure 3.5, a shock wave moves into the low
pressure chamber and an expansion wave moves into the high pressure chamber.
With the exception of the region between the expansion front and the "termina-
ting characteristic," simple analytical solution for this problem is available
(Liepmann and Roshko, 1967). This solution is used to check the calculations of
TRAC-P1A.

A shock-tube with 10 cm in inside diameter and 20 m in length is chosen. A
rather long shock-tube is chosen so that an appreciable amount of time (on the
order of 10 ms) is needed for the shock wave to reach the closed end. The TRAC
calculation is then terminated because the simple analytical solutions are not
valid beyond that time.

In TRAC simulation, a PIPE component represents the shock-tube. A FILL com-
ponent with zero velocity boundary condition is attached to each end of the PIPE
component to represent the closed ends of the shock-tube. First, a nodalization
study is conducted with 40, 100, 200 and 400 cells with initial pressure ratio
of 2 (2 bars in the high pressure chamber and 1 bar in the low pressure chamber)
and initial air temperature of 300K in both the chambers. The run with 400
cells did not materialize due to SCM overflow. However, it was found that the
results for 100 and 200 cells were quite close so that the results for 200 cells
could be accepted as the TRAC prediction. Comparisons between the simple analy-
tical solutions and the TRAC calculations for different nodalization are shown
in Figures 3.6 and 3.7. It is seen that even for 200 cells, the pressure and
temperature distributions calculated by TRAC are not as sharp as the analytical
solutions at the shock wave and at the expansion front. This is believed to be
due to numerical diffusion inherent in the TRAC numerical scheme. It should,
however, be noted that TRAC predicts the magnitude of pressure between the
shock-wave and the "terminating characteristic" quite well as long as sufficient
nodes are used.

Similar results are obtained with different initial pressure ratios and ini-
tial air temperatures. Some numerical instability or "noise" has been observed
at higher initial pressure ratios (50 or more). An example is show in Figure
3.8. The time steps, selected by the TRAC code for this calculatio , were
higher than the minimum time step specified through the input. Therefore, the
instabilities were not due to any input restrictions, and the reason for this
anomaly is not known at this time. Further study is needed in this area.

3.3 Marviken Critical Flow Tests (U. S. Rohatgi)

The Marviken Critical Flow Test consists of a full scale reactor vessel,
which is connected to a discharge pipe and a nozzle. The vessel contains vapor
as well as both saturated and subcooled liquid. This subcooled liquid has a
specific temperature profile, which is maintained by a set of heaters (Ericson
et al, 1979). The TRAC-P1A has been used to simulate Test 22 (L/D = 1.5) and
Test 24 (L/D = 0.33). The mass flux predictions in the nozzle are always lower
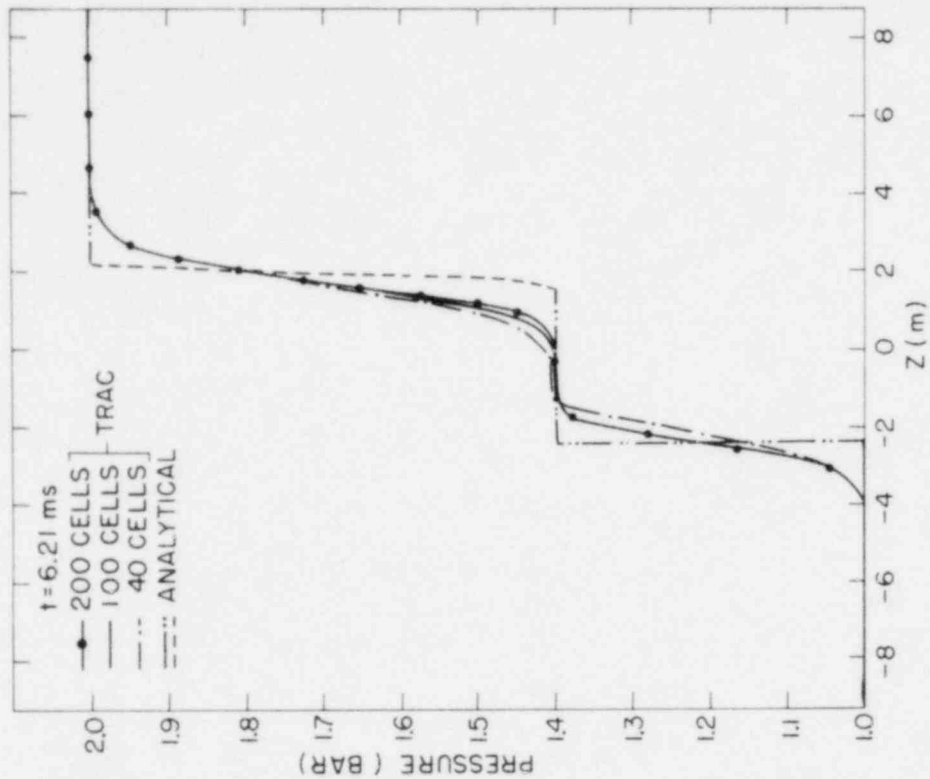than the experimental values. This underprediction could be due to many causes,

Figure 3.6 - Comparison of TRAC-P1A Prediction of Pressure with Simple Analytical Solution. (BNL Neg. No. 9-703-79)
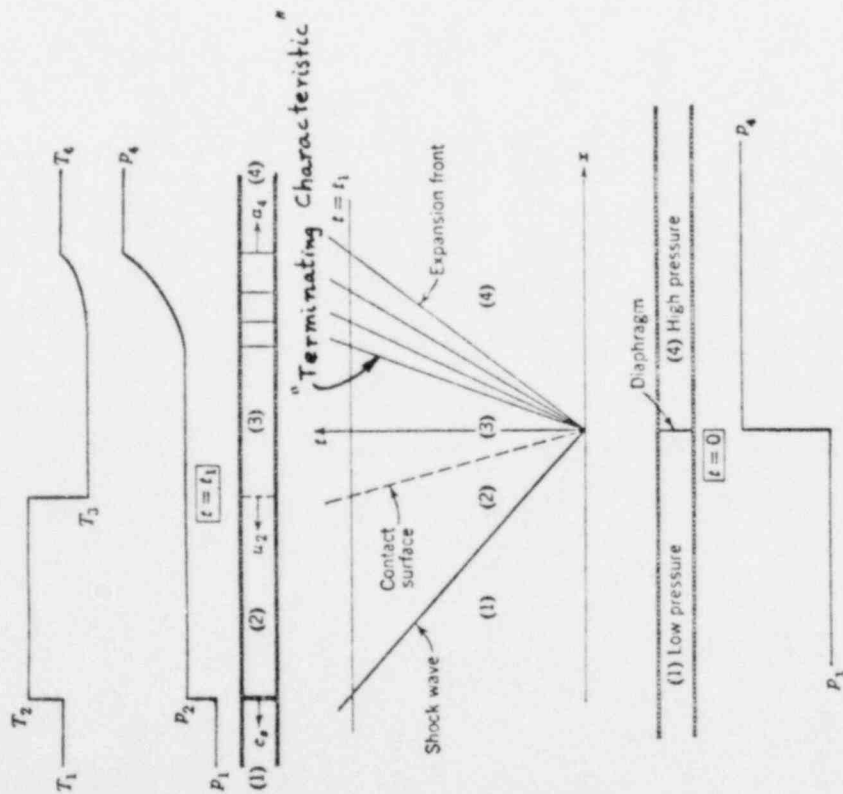

Figure 3.5 - Motion in a Shock-Tube. (BNL Neg. No. 10-1415-79)
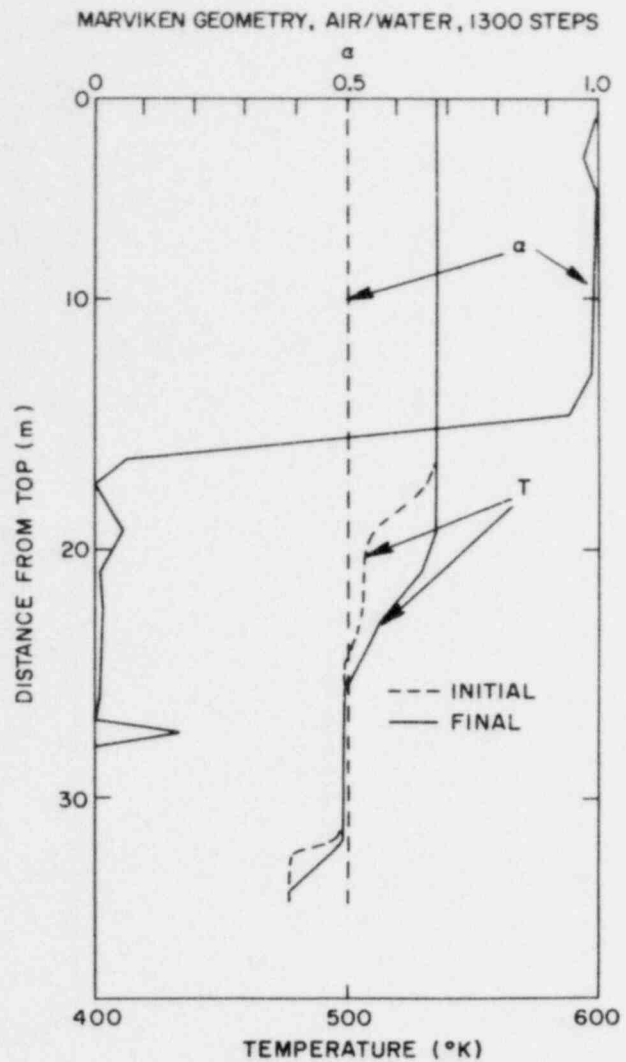
MARVIKEN GEOMETRY, AIR/WATER, 1300 STEPS

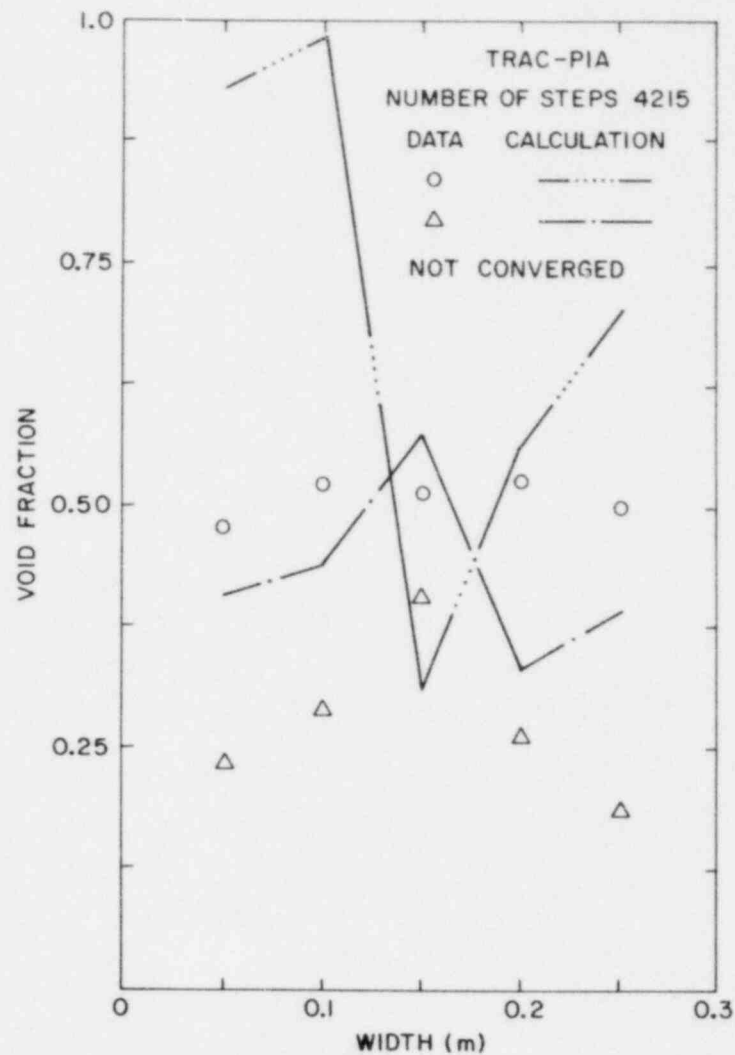Figure 3.9 - Initial and Steady State Void Distribution in Two Pipe System.
(BNL Neg. No. 11-51-79)

Figure 3.10 - Void Distribution in the RPI Two-Dimensional Vessel. (BNL Neg. No. 11-54-79)

void fraction was computed by assuming slug flow regime at the inlet of the vessel. In our further simulation, we will model the inlet pipe from the tee, where air and water mix, to the bottom of the test vessel. This will allow us to specify the void fractions where we know them (water inlet and air inlet).

3.5 FRIGG Loop Test (L. Neymotin)

The FRIGG Loop test (Nylund, 1968) consists of a vessel with downcomer, core, riser, phase separator and condenser. However, as most of the measurements of pressure and void fraction are in the core bundle region, and since TRAC-P1A does not have a separator model included, TRAC-P1A will be used for simulating only the core and downcomer region. In preparation for actual FRIGG vessel, it was decided to first try a simple vessel run to get experience with the vessel and also to test TRAC-P1A for simple problems. This is accomplished by taking a system as shown in Figure 3.11. It contains a core region without rods, a downcomer and a lower plenum. There is one input pipe connected to the downcomer to supply the liquid, which flows out through the set of pipes and the breaks connected to the top of the core. The flow configuration is quite complicated due to asymmetry in velocity field and recirculation zone.

Flow region has been divided into five equal parts in vertical direction and has four regions in radial direction. Three of these rings r= .1, .2, .3m are representing the core and one outer ring (r=0.4m) is for the downcomer. In 0-direction vessel was divided into three equal sections (120°) only for saving computer time. The calculation took about 45 minutes of computer time to achieve the steady-state with 2.7 sec. of real time.

The solution seems physically reasonable. The fluid enters the downcomer normally to its walls and goes around the core outer shell. It also moves downwards to the core entrance, which is located at level 1 (Figure 3.11, 3.12). Figure 3.13 shows the axial velocity profile predicted by the TRAC at L/D = 2.5. An attempt to get such a profile farther from the entrance by increasing the step size in axial direction has been unsuccessful (problem did not converge). Perhaps, it was caused implicitly by existance of some limiting relationship between space steps in z and v-directions. On the other hand, increasing the number of axial steps with the old step sizes would be too expensive in computer time. Furthermore, TRAC lacks any kind of momentum exchange in the free fluid region one space step away from the solid boundaries (for single-phase fluid). This results in velocity profile invariability in the cells which have no solid surfaces. Static pressure distribution in the core and downcomer is shown in Figure 3.14. It looks reasonable. The sharp pressure increasing in cell 12, level 5 is related with the 90° flow turning in this downcomer region.

The experience gained during the computation of 3-dimensional single-phase for the vessel-like geometry will be useful in trying actual FRIGG loop. It should be mentioned, that detailed calculations of such a complicated system will be very expensive in terms of computer time.
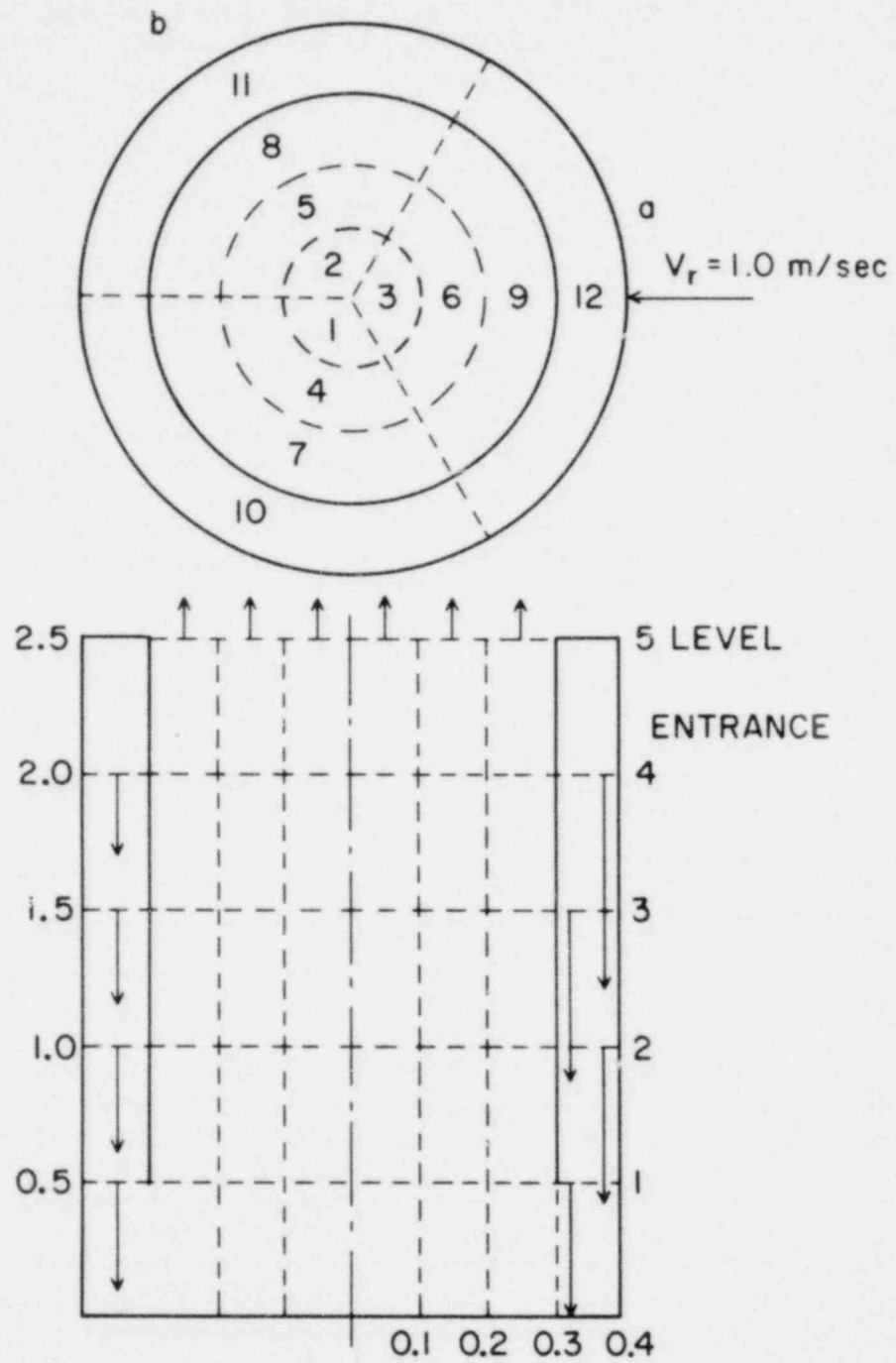
Figure 3.11 - Vessel Geometry, Nodalization and Axial Velocity Distribution. (BNL Neg. No. 11-49-79)
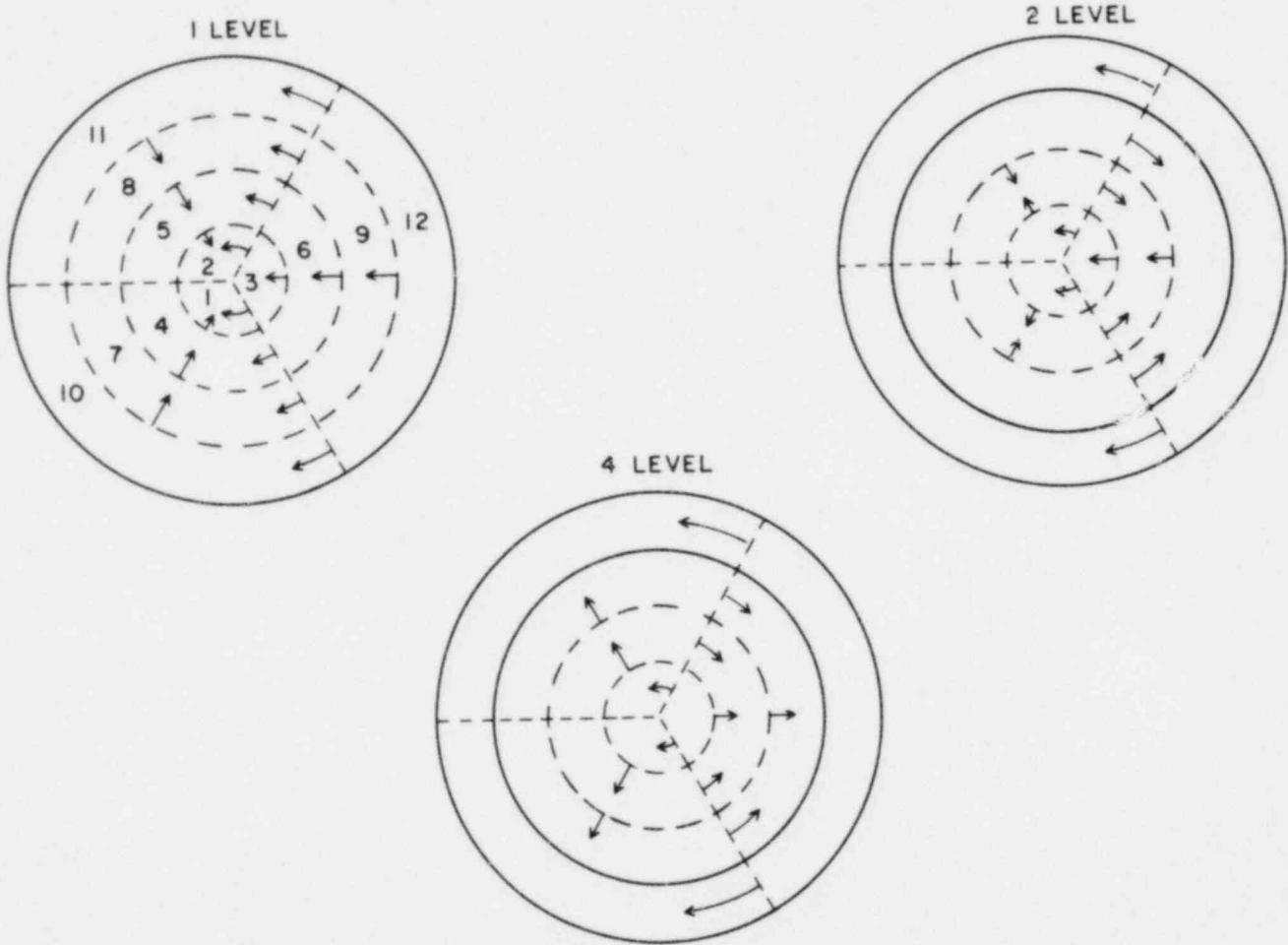
Figure 3.12 - Radial and Azimultial Velocity Distribution at Three Levels in the Vessel. (BNL Neg. No. 11-50-79)
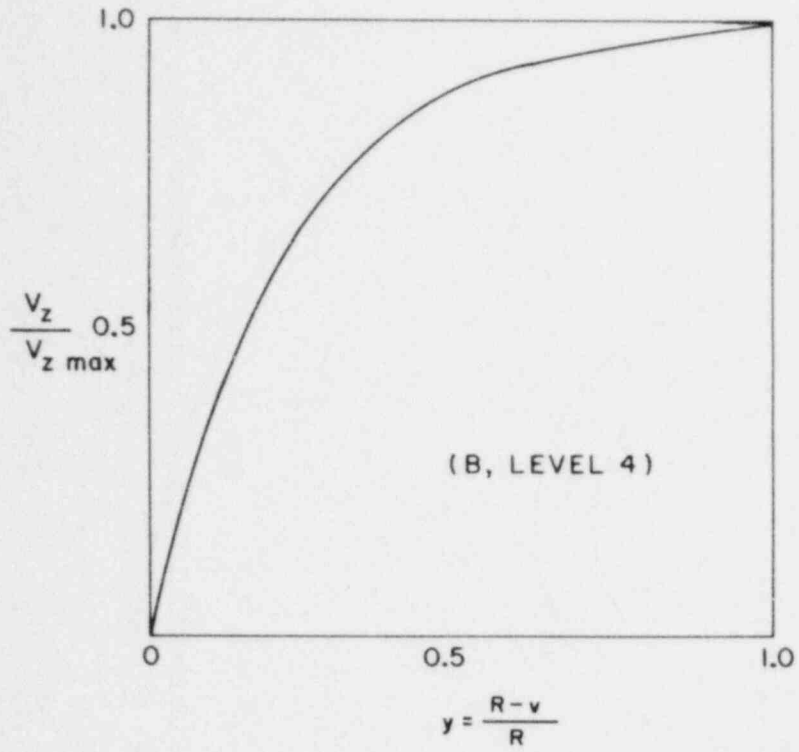
Figure 3.14 - Axial Pressure Distribution at
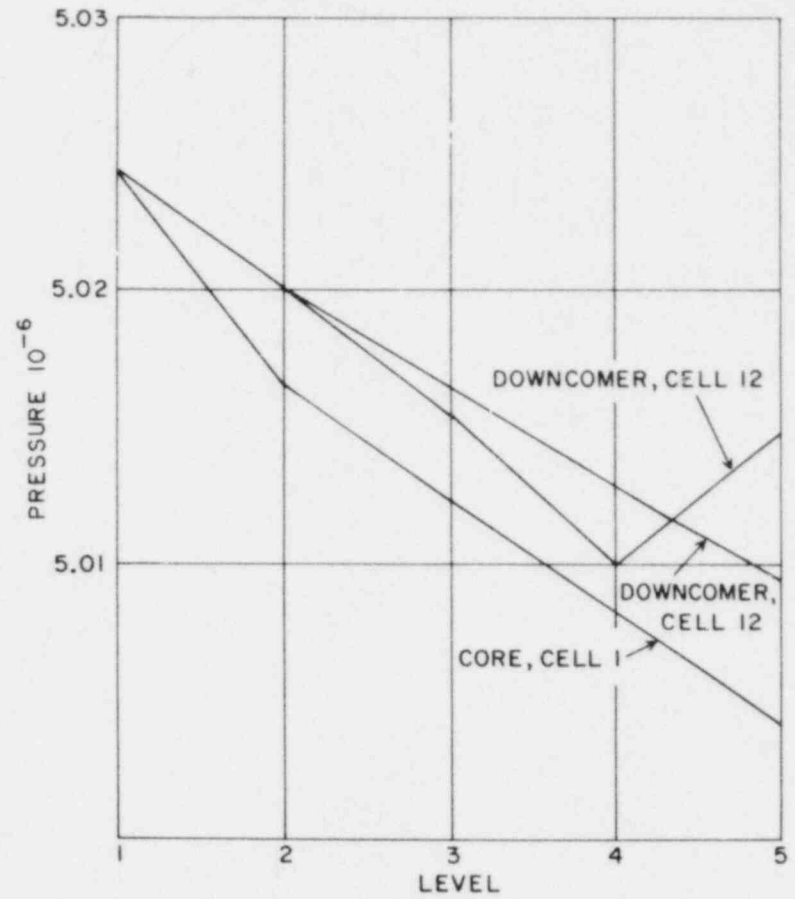Different Locations in the Vessel.
(BNL Neg. No. 11-53-79)

Figure 3.13 - Axial velocity profile in the Core
Section at Level 4.   (BNL Neg. No. 11-52-79)

3.6 Constitutive Relations in TRAC-P1A (U. S. Rohatgi and P. Saha)

A document has been prepared in order to describe the basic thermal-hydraulic models and correlations employed in the TRAC-P1A code. This task required inspection of certain subroutines in the code and provided more detailed information regarding TRAC models to the members of the Advanced Code Review Group (ACRG). Upon receiving comments from the ACRG members and others, the document shall be issued as a BNL-NUREG report.

REFERENCES

ERICSON, L., et al., "MXC-222, Interim Report Results from Test 22," Joint reactor safety experiments in Marviken Power Station, Sweden, MX3-87, March, 1979.

ERICSON, L., et al., "MXC-224, Interim Report Results from Test 24," Joint reactor safety experiments in Marviken Power, Sweden, MX3-91, May 1979.

JEANDEY, C. and BARRIERE, G., (1979), "Partie I: Etude Experimentale d'Ecoulements Eau-Air a Grande Vitesse," DTCE/STT/SETRE Note T.T. No. 599, Janvier 1979.

LAHEY, R. T., "Two-Phase Flow Phenomena in Nuclear Reactor Technology," Quarterly Progress Report 8, NUREG-CR-0418, March-May 1978.

LIEPMANN, H. W. and ROSHKO, A., (1967), "Elements of Gasdynamics," Chapter 3, John Wiley & Sons, Inc., N.Y., 1969.

NYLUND, O., et al., "FRIGG Loop Project: Hydrodynamic and Heat Transfer Measurements on a Full-Scale Simulated 36-rod Marviken Fuel Element with Uniform Heat Flux Distribution," FRIGG-2, AB Atomenergi, Stockholm, 1968.

SAHA, P., (1979), "Moby-Dick Nitrogen-Water Experiments," Quarterly Progress Report Water Reactor Safety Research Division, April-June, 1979.

TRAC-P1A: An Advanced Best-Estimate Computer Program for PWR LOCA Analysis (1979), Vol. I., Los Alamos Scientific Laboratory, Los Alamos, N.M., March 1979.

II.   METALLURGY AND MATERIALS EVALUATION

SUMMARY

The susceptibility of Inconel alloy 600 to intergranular stress corrosion cracking (SCC) is being investigated in pure water, simulated primary water and environments with an all volatile treatment (AVT) typical of secondary side water in PWR steam generators. U-bend specimens made from several heats of production grade steam generatory tubing have failed by SCC in these environments. Failure times in pure water and primary water are similar, but initial tests indicate that an AVT environment decreases the time necessary to produce cracking.

Constant stress tests and constant extension rate tests have indicated that small amounts of cold working appear to accelerate the failure of susceptible materials. Specimens stressed to 120%, 140% and 160% of their yield strength have failed by stress corrosion cracking.

Constant extension rate tests have shown similar activation energies for two heats of material tested.

1. <u>Stress Corrosion Cracking of PWR Steam Generator Tubing</u>

(T.S. Bulischeck and D. van Rooyen)

1.1 Constant Deflection Tests

U-bend tests are in progress in pure deaerated water at $325^{\circ}C$ and $290^{\circ}C$, in simulated primary water at $365^{\circ}C$ and in AVT environment at $345^{\circ}C$. Stress corrosion cracking has been produced in some heats of production grade tubing in each of these environments. Figures 1, 2, 3, 4 and 5 show the relationship between failure time and environment temperature for the heats of material that have exhibited SCC. The slopes of the lines on these plots indicate that a significant heat to heat variation exists. Some difference may be accounted for by the different stress levels produced when bending the U-bends. The tubes used for this program vary both in diameter and in wall thickness. All of the U-bends are formed on the same bending fixture which produces a specimen with a 0.5" radius of bend. The differences in stress level result from wall thickness variations and the increased flare of thin-walled tubes provide a larger hoop stress component. The stress levels of these specimens are being measured by photoelastic techniques and these results are expected within the next several months.

U-bend specimens have been exposed to pure deaerated H_2O at $325^{\circ}C$ for 40 weeks and these tests were scheduled to be terminated to provide facilities for other tests. However, only one specimen (Fig. 3) from one heat of material has shown SCC at this temperature. It is, therefore, necessary to continue this test beyond its scheduled expiration date. Additional data at $325^{\circ}C$ are needed to determine the relationship between failure time and temperature so that high temperature test results may be extrapolated to operating temperatures.

Primary water tests are being conducted in a circulating autoclave system. The solution contains 1000 ppm B as boric acid and $10^{-4}m$ LiOH with the H_2 adjusted to 35 STP cc/Kg. U-bends exposed to this environment at $365^{\circ}C$ for 13 weeks have produced SCC in two heats of material. Figures 1 & 2 show that there is very little difference between the failure times of specimens exposed to pure water and those in primary water environments. The other three heats of material which cracked in pure water (Fig. 3, 4, and 5) have not failed in primary water. This is probably due to the fact that heats #10 and #11 cracked mainly in the pickled condition in pure water and specimens with this treatment were only recently added to the primary water test. The exposure time for heat #5 in primary water is still less than the time required to produce failure of unpickled specimens in pure water.

Conditions simulating all volatile treatment (AVT) were produced in a static autoclave system by following the degassing procedures used for pure water tests. The system was then cooled to slightly below the boiling point and hydrazine and morpholine solutions were injected with care being taken to prevent any atmospheric contamination. The concentrations were adjusted to give a hydrazine concentration of 100 ppb with morpholine at 5 ppm. The starting solution had a pH of 8.8 and total conductivity of 3.1 μmho/cm. AVT tests are operated at $345^{\circ}C$ and decomposition of both additives are expected

at this temperature. Hydrazine will decompose within the first few hours, but its rapid gettering action will have completed the oxygen removal by this time. Morpholine will remain approximately 1 week before complete decomposition. These above estimates are being investigated by sampling the liquid and vapor phase in the system at the end of the two week tests.

Specimen exposures in AVT at 345°C have been in progress for eight weeks. Pickled specimens were not included in the initial exposures and, therefore, no direct comparison is yet available for those heats of material which cracked only in the pickled condition in pure water. The two heats of material which failed in AVT (Fig. 1 and 2) have a much shorter time to failure than those exposed to pure water environments. This may possibly be due to further reduction of the low level O_2 concentrations. Additional data are needed to determine if this tendency for shorter failure times in AVT is a real effect or if these initial failures are due only to the scatter typically experienced in this type of test.

Nuclear steam generator tubing, that has received a commercial heat treatment to sensitize the material and provide increased SCC resistance, has been included in both the primary water and AVT tests. These specimens are being tested in both the as received and pickled conditions.

1.2 Constant Stress Test

Constant stress tests are in progress using two types of tensile specimens. The initial tests are pure water environments at 365°C. The one type of tensile specimen used for this test is the design that is also used for the constant extension rate tests. A section of tubing is rolled flat and the specimen is then machined into a dog bone shape as specified in ASTM A370. The rolling results in a small amount of cold working ($\sim3\%$) which seems to accelerate SCC in both the constant stress and constant extension rate tests. Efforts will be made in the near future to determine the residual stress in these specimens. Figure 6 shows that constant stress tests using these plate type tensile specimens produce intergranular failure in very short times. The load was applied with bolt-loaded pull rods and the applied load was continuously recorded. Some variations in load were experienced due to room temperature oscillations, and the error bars on Figure 6 show this range. Additional tests are in progress using plate type specimens exposed to the same conditions to see if the results are repeatable. A test is in progress using a dual ligament tube type specimen which has not received any cold working. This specimen is exposed to pure water at 365°C and the load is precisely controlled by an MTS system. An applied load of 160% y.s. has not produced specimen failure after 3 weeks exposure. It appears from the data obtained thus far in both the constant stress test and constant extension rate tests that very small amounts of cold working are detrimental to the service life of steam generator tubing.

1.3 Constant Extension Rate Tests

The data obtained thus far from the constant extension rate tests are shown in Figure 7. As previously reported, the crack velocities are calculated by dividing the maximum intergranular crack depth by the straining time

from the yield point to final fracture. Several specimens which have been examined after straining small amounts indicate that SCC may start well after the yield point, but many additional tests are needed to determine where this does occur. Consequently, the crack velocities in Figure 7 may be somewhat higher than indicated. Recent tests show that the slope of the data from two different heats of material tested agree very well. If this slope remains the same for other heats of material tested, many heats of material may be rapidly evaluated by performing high temperature tests and extrapolating the results to operating temperatures.

1.4 Capsule Tests

Inconel 600 capsules containing carbon steel slugs and a corrosive environment have been exposed to primary water for 6 weeks at 290°C and 6 weeks at 325°C. The internal environment in the capsules corrode the carbon steel and provide tensile stress patterns in the outside surface of the tubing similar to those experienced by dented tubes. The outside surface is then exposed to primary water which is the environment involved in recent service related failures. These capsules have deformed such that an increase in outside diameter of up to .012" has been measured, but no SCC has been observed. This test conforms to the requirement scheduled in the program proposal for investigating different stress patterns.
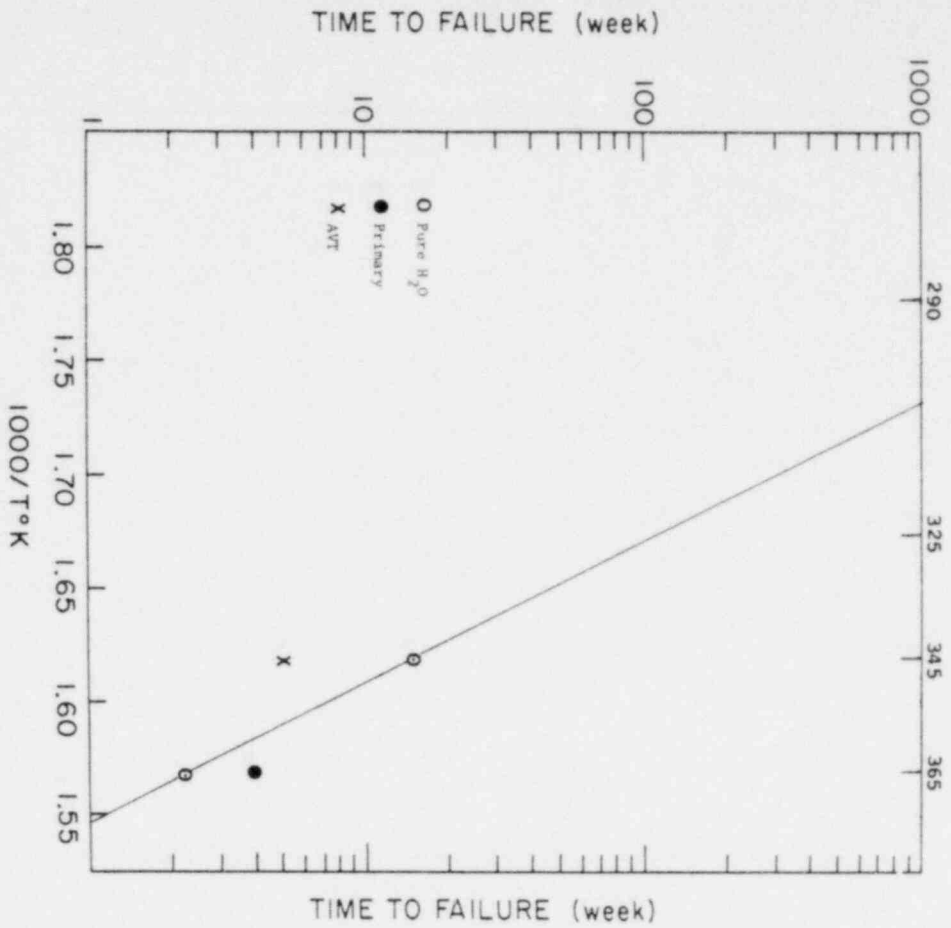
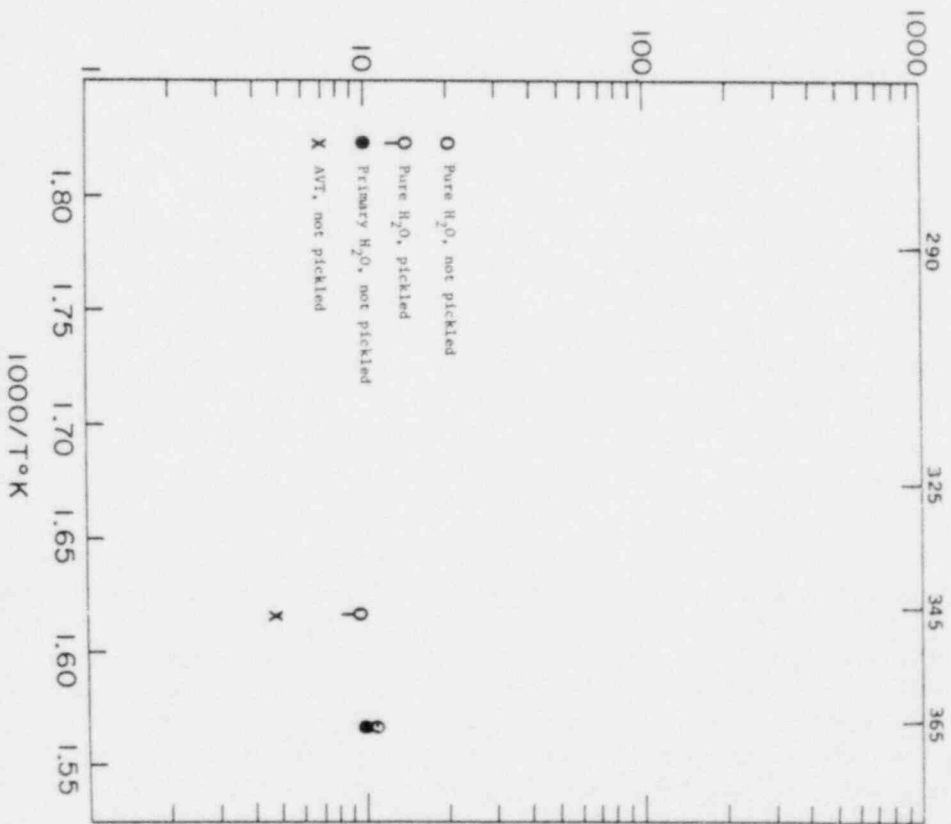Fig. 1 Failure Time vs. Temperature for SCC of Heat #2 Specimens

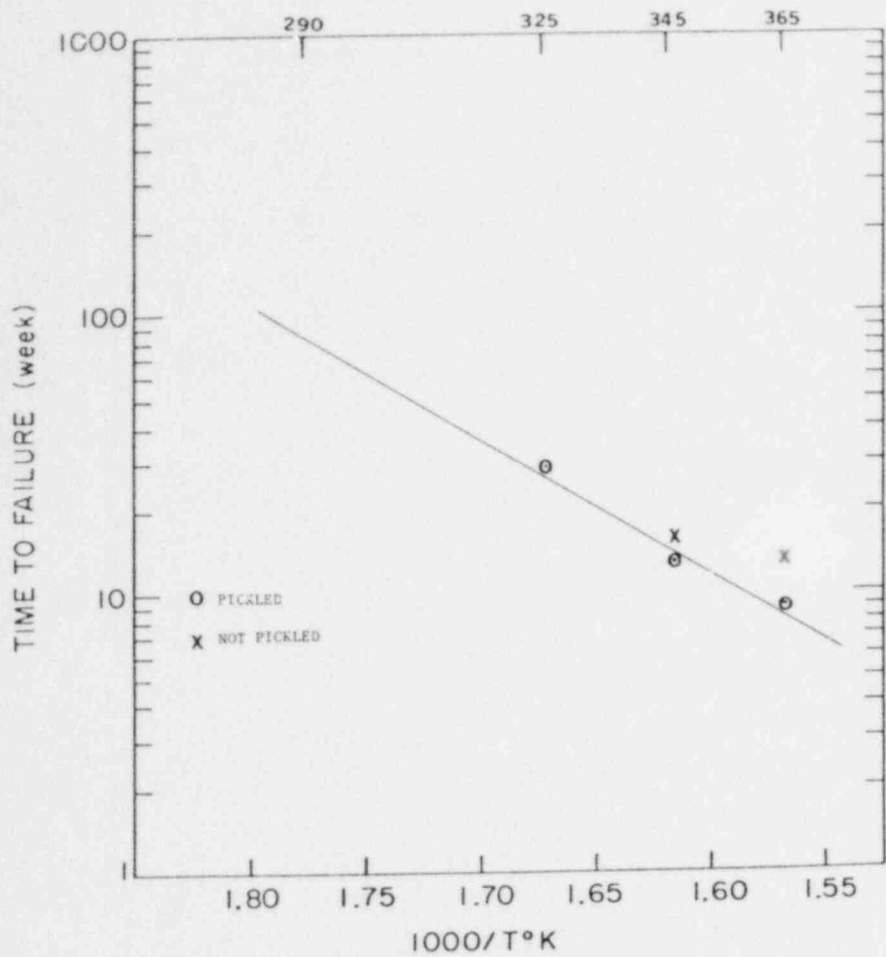Fig. 2 Failure Time vs. Temperature for SCC of Heat #4 Specimens

Fig. 3   Failure Time vs. Temperature for SCC
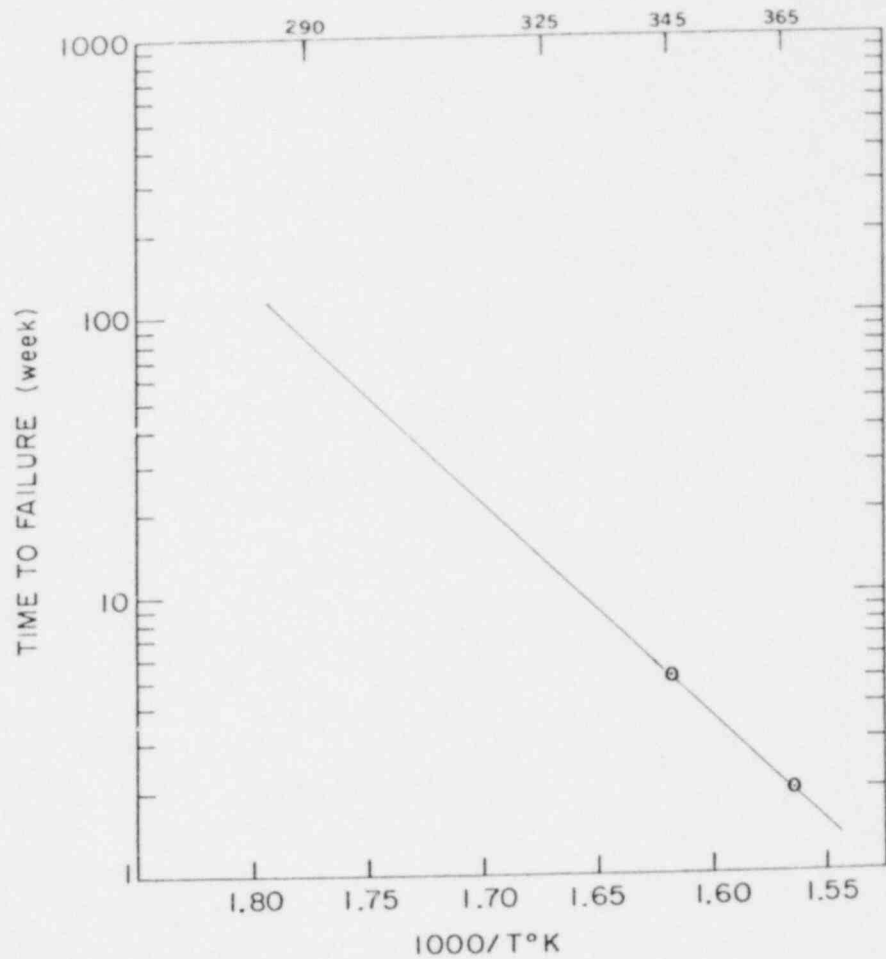of Heat #5 U-bend Specimens in Pure
Deaerated H_2O

Fig. 4   Failure Time vs. Temperature for SCC
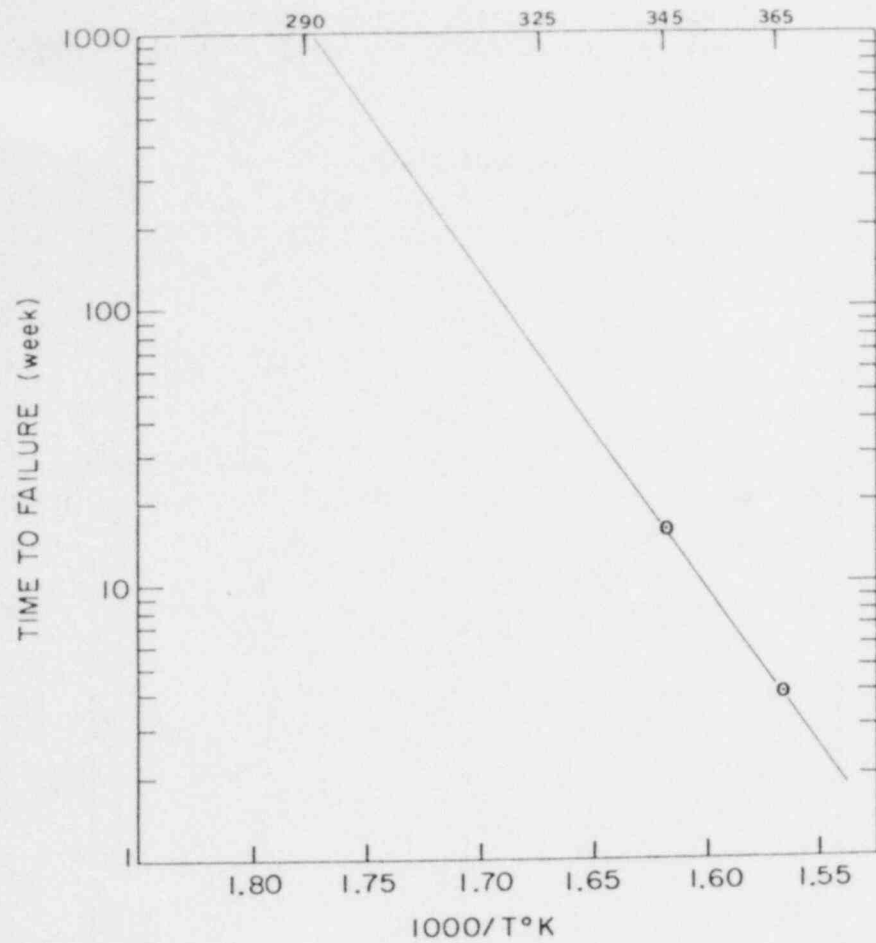of Heat #10 Pickled Specimens in Pure
Deaerated H_2O

Fig. 5 Failure Time vs. Temperature for SCC
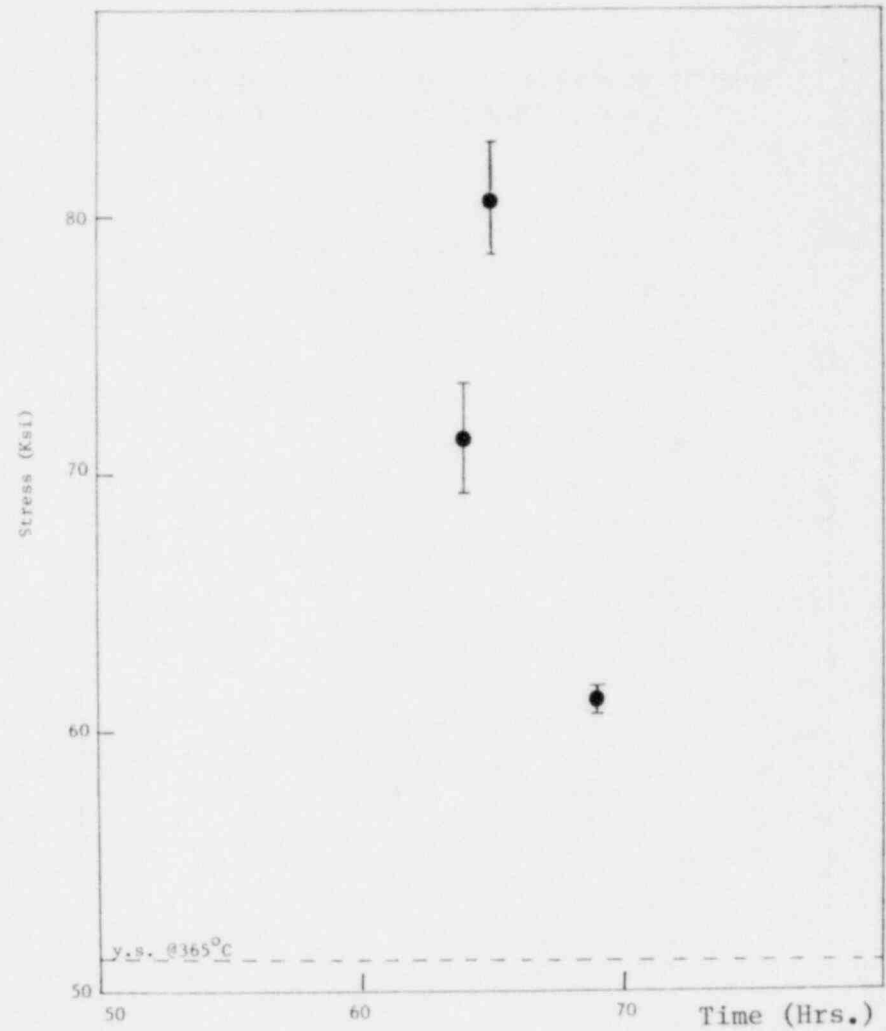of Heat #11 Pickled Specimens in Pure
Deaerated H_2O

Fig. 6 Time to Failure for Specimens from Heat #4
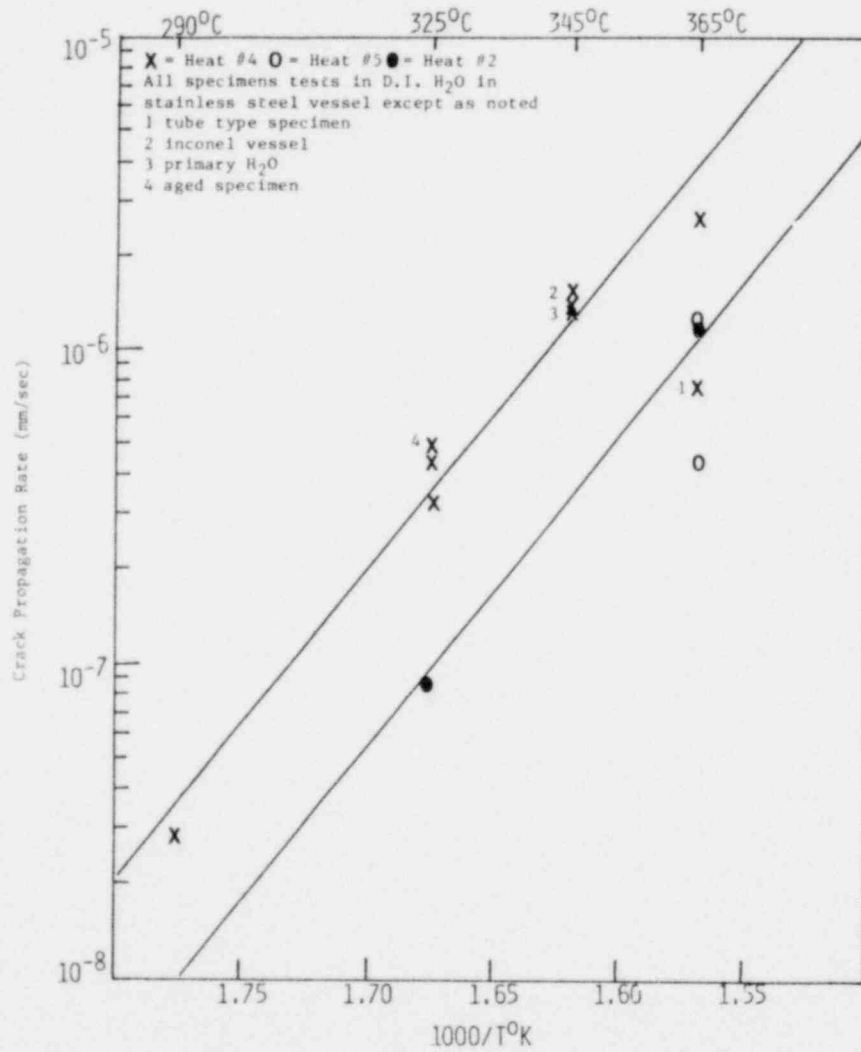Stressed in Pure Deaerated H_2O at $365^{\circ}C$

Fig. 7   Effect of Temperature on Crack
         Velocity for Materials Tested
         in C.E.R.T.